Fundamental Electrochemical Properties of Liquid Metals in LiCl-KCl for Separation of Alkali/Alkaline-Earths (Cs, Sr, and Ba)

Final Report

Hojong Kim, Supathorn Phongikaroon, James L. Willit

December 21, 2018

Award: DE-NE0008425
Funding Opportunity: DE-FOA-0001129
Funding Agency: Office of Nuclear Energy
Lead Recipient: The Pennsylvania State University
Project Title: Fundamental Electrochemical Properties of Liquid Metals in LiCl-KCl for Separation of Alkali/Alkaline-Earths (Cs, Sr and Ba)
Principle Investigator: Hojong Kim (The Pennsylvania State University)
Collaborators: Supathorn Phongikaroon (Virginia Commonwealth University), James L. Willit (Argonne National Laboratory)
Date of Report: December 21, 2018
Project Period: October 1, 2015 – September 30, 2018

Table of Contents

List of Figures

List of Tables

ABSTRACT

In electrorefiner, uranium is recovered from used nuclear fuel using an electrorefining process in which a metallic used nuclear fuel anode is oxidized into molten LiCl-KCl-UCl_3 electrolyte and pure U is preferentially reduced onto an inert cathode. While electrorefiner systems facilitate the recycling of substantial amounts of uranium from used nuclear fuel, they also contribute to the production of nuclear waste due to the build-up of fission products such as ^{90}Sr and ^{137}Cs in the molten salt electrolyte as they are electrochemically more active than U. The accumulation of alkali/alkaline-earth elements (Ba, Sr, Cs) in the electrolyte presents a problem as Sr and Cs isotopes have high heat densities and produce large amounts of highly ionizing radiation; these hazards combined with difficulty in removing the highly stable alkali/alkaline-earth elements from the electrolyte necessitates frequent replacement and disposal of the electrolyte, which then increases the overall volume of nuclear waste. This research project focuses on evaluating the viability of using liquid metal electrodes for electrochemical separation of alkali/alkaline-earths from molten salts utilizing the strong atomic interactions between candidate liquid metals and alkali/alkaline-earths. The strength of chemical interactions was quantified by determining the thermodynamic properties (e.g., activity) in liquid metals of Bi, Sb, and Pb.

Thermodynamic properties, including activities, partial molar entropies, and partial molar enthalpies, were determined using electromotive force measurements for the Sr-Bi, Sr-Sb, Sr-Pb, Ba-Bi, and Ba-Sb binary systems in order to elucidate the strength of interactions between the alkaline-earth elements and each liquid metal, and to develop a comprehensive understanding of their behavior. Activities as low as $a_{Sr} = 10^{-13}$ at $x_{Sr} = 0.04$ at $T = 888$ K were measured as well as liquid state solubility as high as 40 mol% at 988 K in Sr-liquid metal systems; activities as low as $a_{Ba} = 10^{-15}$ at $x_{Ba} = 0.05$ at $T = 888$ K with liquid state solubility as high as 30 mol% at 988 K in Ba-liquid metal systems. Experimental data was used as input data towards computational efforts involving first-principles calculations as well as the CALPHAD (CALculation of PHAse Diagram) technique in the case of the Sr-Sb and Ba-Bi systems to develop improved phase diagrams and provide further basis for the use of computational models in elucidating strongly interacting binary systems.

Attempts to remove Sr and Ba from molten salt electrolyte using an electrochemical cell with liquid metal cathodes were successful, with post-mortem elemental analysis of the electrodes confirming significant quantities of Sr (6.5 mol%) and Ba (12.8 mol%) deposited into Bi. Furthermore, deposition results correlated well with the deposition behavior predicted from the aforementioned electromotive force measurements, inviting the possibility of using liquid metal electrodes for selectively removing alkali/alkaline-earth elements from molten LiCl-KCl electrolyte to recycle the process salt in electrorefiner.

1. Introduction

1.1 Motivation/Problem Statement

One of the most promising recycling methods for used nuclear fuel is an electrochemical method known as electrorefining. Electrorefining processes used nuclear fuel in order to recover uranium which can then be re-enriched and re-used as nuclear fuel [1]. An electrorefiner system operates as a simple two-electrode electrochemical cell where the used metallic nuclear fuel acts as an anode, an inert steel mandrel as a cathode, and LiCl-KCl-UCl_3 (10 wt%) as a molten salt electrolyte (Figure 1).

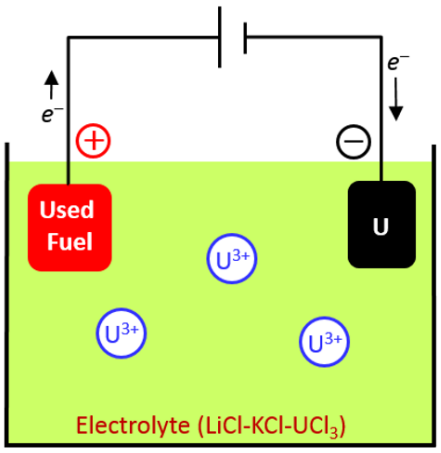

Figure 1. Schematic of a simplified electrorefining process, with uranium oxidized from metallic used nuclear fuel at the anode and pure uranium reduced at the cathode in molten salt LiCl-KCl-UCl_3 electrolyte.

As depicted in **Error! Reference source not found.**, when current is passed, uranium will be oxidized out of the used fuel anode and pure uranium metal is reduced at the inert steel cathode via the following reactions:

$$\textbf{Anode: U(in anode)} \rightarrow \mathbf{U^{3+} + 3e^-}$$
$$\textbf{Cathode: } \mathbf{U^{3+} + 3e^-} \rightarrow \textbf{U(on cathode)}$$

, with the overall reaction given by:

$$\textbf{U(in anode)} \rightarrow \textbf{U(on cathode)}$$

The recovered pure U can then be subjected to the enrichment process for further re-use. Unfortunately, electrorefiner systems do not operate ideally as shown in Figure 1 because used nuclear fuel is composed of diverse fission products (e.g., alkali, alkaline-earth, rare-earth elements etc.) that possess distinct electrochemical properties including standard reduction potential in the chloride system (Figure 2).

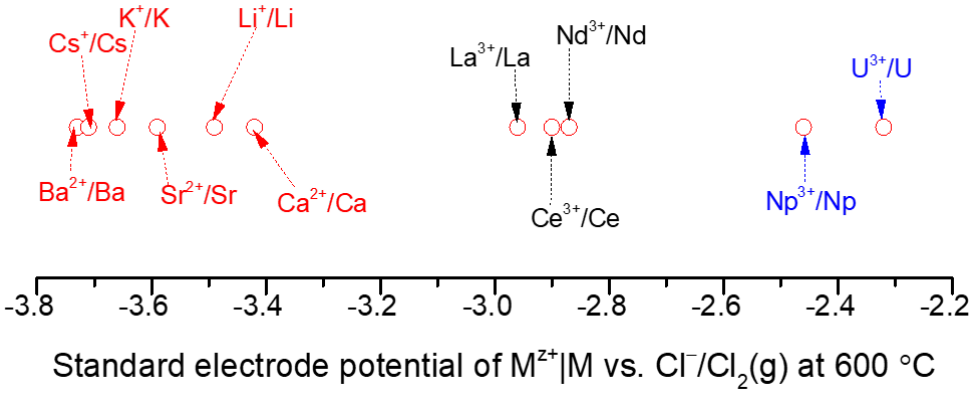

Figure 2. Standard electrode potentials of $M^{z+}|M$ vs. the Cl^-/Cl_2 (g) couple at 600 °C, where *z* is the number of electrons in each half-cell reaction and M are the pure metals [2].

A standard reduction potential represents a species' tendency to be reduced, with more positive potentials indicating a higher tendency for reduction. **Error! Reference source not found.**2 depicts the standard reduction potentials of various components of used nuclear fuel; it is clear that Ba, Sr, K, and Cs are the last elements to reduce out of the LiCl-KCl-UCl_3 electrolyte due to their highly negative potentials and that U, having the most positive potential, is the first element to reduce. At first glance this may not seem to be an issue for the electrorefiner system as U is the element of interest for recovery from the used nuclear fuel; however, any metallic elements with more negative redox potentials than U (e.g., Cs, Sr, Ba, and rare-earth metals) will be co-oxidized from the anode and accumulated in the molten salt electrolyte.

As alkali and alkaline-earth elements, A (A = Ba, Sr, Cs), only account for a maximum of 12% of the used nuclear fuel composition, the question as to why A are the focus of this work arises. Firstly, ^{90}Sr and ^{137}Cs are dangerous isotopes due to their short half-lives (~30 years), highly ionizing β and γ radiation, and high heat densities (~100 W L^{-1}) [3]. In fact, despite accounting for a small fraction of the composition of used nuclear fuel, Sr and Cs exhibit the highest heat densities among fission products, more than 6 times greater than the other elements of actinides and rare earths. Secondly, A are comparatively very difficult to remove from the LiCl-KCl-UCl_3 electrolyte due to their highly negative redox potentials. Based on the redox potentials (Figure 2), it is evident that rare earth elements and actinides could theoretically be removed from the electrolyte by continuing to pass current after all U has been reduced out as they have the next most positive standard reduction potentials. Unfortunately, this same idea cannot be applied to reduce out A as Ba, Sr, and Cs all have standard reduction potentials more negative than Li, a primary component of the molten salt electrolyte. Therefore, any attempt to remove A by simply continuing to reduce elements out of the electrolyte would result in the reduction of Li^+ to Li, i.e. the decomposition of the main constituent of supporting electrolyte system.

1.2 Background

Previous research by Kim et al. [4] suggests that the large electronegativity difference between alkali/alkaline-earth elements and liquid metals, M (M = Bi, Sb, and Pb) will allow them to be preferentially separated from molten salt electrolytes. In the case of a multi-component molten salt electrolyte ($BaCl_2$-LiCl-$CaCl_2$-NaCl, 16-29-35-20 mol%), Kim et al. [4] found that a

liquid metal (Bi) electrode was able to separate conventionally non-separable species. According to the standard reduction potentials for Ba^{2+}/Ba (-3.74 V), Li^{+}/Li (-3.49 V), Ca^{2+}/Ca (-3.44 V), and Na^{+}/Na (-3.42 V) vs. $Cl^{-}/Cl_2(g)$ at 600 °C, deposition should proceed in the following order: Na → Ca → Li → Ba, with Na being the first to reduce and Ba being the last. However, after discharging the Bi electrode at 50 C g^{-1} with a constant current density of j = -100 mA cm^{-2} at 600 °C, Ba was found to be the dominant species in the Bi electrode via post-mortem scanning electron microscopy (SEM) with electron dispersive spectroscopy (EDS) (Figure 3).

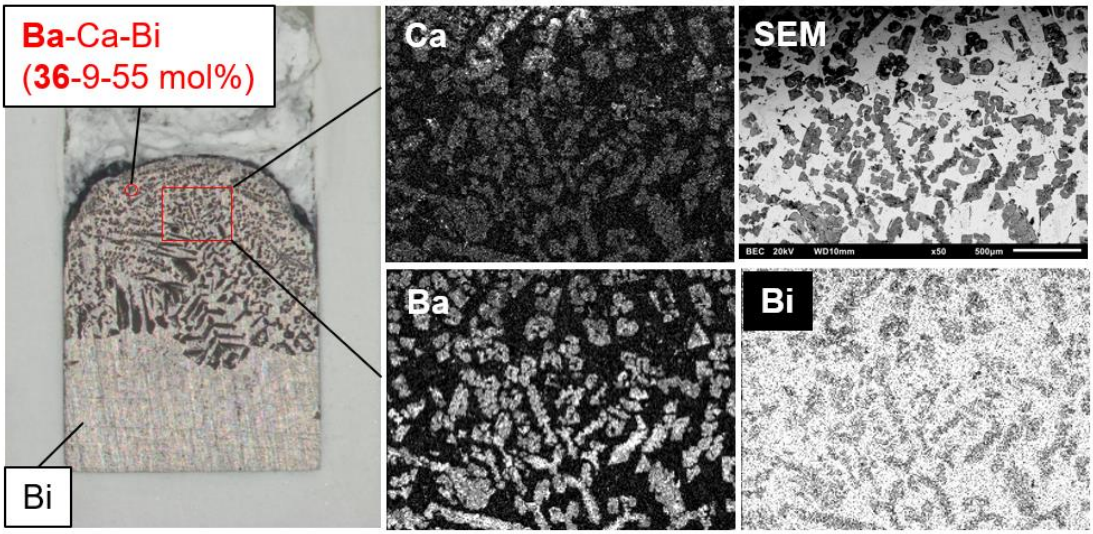

Figure 3. Optical image of the Bi electrode discharged at 50 C g^{-1} from $BaCl_2$-LiCl-$CaCl_2$-NaCl molten salt electrolyte with constant current density (-100 mA cm^{-2}) at 600 °C with accompanying compositional analysis via EDS [4].

Despite the conventionally expected deposition order, which had placed Ba as the last species to leave the electrolyte, the solidified electrode was found to be composed of Ba-Ca-Bi intermetallic (35-9-55 mol%). Strong electron donor-acceptor interactions between the elements are believed to cause a shift in their conventional redox potentials, which means alkali/alkaline earths can theoretically be selectively deposited into a liquid metal electrode from chloride-based electrolyte. Based on Figure 2 and the previous analysis, an inert electrode in a chloride-based salt will be entirely ineffective at removing Ba^{2+}, Sr^{2+}, Cs^{+}; however, an electrode that interacts more strongly with these ions than with Li^{+} or K^{+} could shift the standard reduction potentials unequally, resulting in a different order of reduction as in the $BaCl_2$-LiCl-$CaCl_2$-NaCl electrolyte with the Bi electrode. The effect of the postulated strong atomic interactions between the alkali/alkaline-earth elements and liquid metals can be rationalized using the Nernst equation:

$$E_{\text{eq}} = E^{0}_{\text{A}^{z+}/\text{A}} - \frac{RT}{zF}\ln\left(\frac{a_{\text{A(in M)}}}{a_{\text{A}^{z+}}}\right) \qquad (1)$$

where E_{eq} is the equilibrium potential, $E^{0}_{\text{A}^{z+}/\text{A}}$ is the standard reduction potential of the A^{z+}/A couple, z is the number of electrons exchanged in the half reactions (z = 2 for alkaline-earth, z = 1 for alkali elements), F is Faraday's constant (equal to 96485.3 C mol^{-1}), R is the ideal gas constant,

T is the absolute temperature, $a_{A(\text{in M})}$ is the activity of element A in interacting electrode M, and $a_{A^{z+}}$ is the activity of ion A^{z+} in the electrolyte. Essentially, Eq. 1 describes the shift away from the standard reduction potential due to activity; as the activity of $a_{A^{z+}}$ in a pure chloride salt is equal to 1, the shift is equivalent to $-\frac{RT}{zF}\ln(a_{A(\text{in M})})$. Therefore, if Bi interacts more strongly with Ba^{2+} than Li^+ or Na^+, the equilibrium potentials for each could be altered and switch the deposition order. Available activity data for Ba^{2+}, Li^+, Ca^{2+}, and Na^+ in Bi was used to estimate the shift in standard reduction potential, shown in Figure 4 [4].

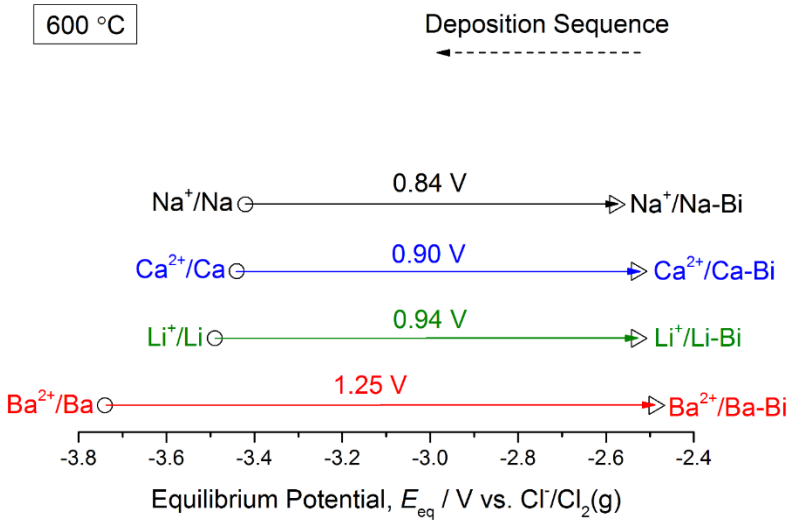

Figure 4. Equilibrium potentials of the Ba, Li, Ca, and Na redox couples at $x_{A(\text{in Bi})} = 0.05$ (triangle) compared to the standard electrode potentials (circle) at 600 °C. Each arrow represents the shift in potential due to the activity of A in the Bi electrode [4].

The low activity of Ba in Bi leads to a large shift in equilibrium potential (1.25 V) compared to the next highest shift (0.94 V for Li), which changes the anticipated reduction order to Ba → Ca → Li → Na. If Ba^{2+}, Sr^{2+}, Cs^+ can be proven to have similarly strong atomic interactions with liquid metals in electrorefiner electrolyte, it may be possible to preferentially remove them from the contaminated electrorefiner salts without causing the decomposition of the electrolyte.

1.3 Proposal/Project Scope

Based on the aforementioned ability of Bi to preferentially remove Ba^{2+} from a molten chloride electrolyte containing Li^+, liquid metal electrodes are a promising option for removing alkaline-earth fission products from LiCl-KCl electrorefiner salt. By leveraging the strong interactions between liquid metals (M = Bi, Sb, Pb) and alkali/alkaline-earths (A = Ba, Sr, Cs), it would be possible to selectively deposit Ba^{2+}, Sr^{2+}, and Cs^+ out of LiCl-KCl-based electrolytes using an electrochemical cell as depicted in Figure 5.

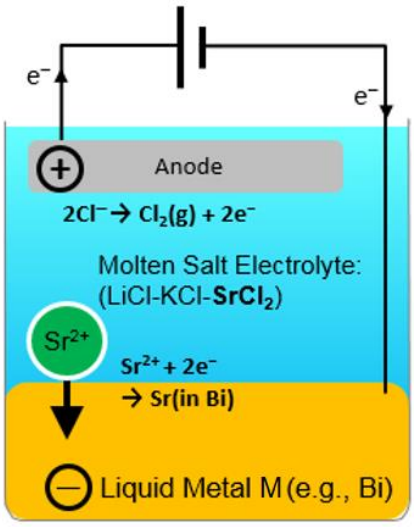

Figure 5. Electrochemical cell design for reduction of Sr^{2+} out of LiCl-KCl-ACl_2 into a Bi electrode, simultaneously producing $Cl_2(g)$ at an inert anode.

By applying a constant current density between the liquid metal working electrode (Bi, in Figure 5) and an inert counter electrode, Sr^{2+} ions in the molten salt electrolyte will be reduced into the Bi and removed from the salt via the following reactions:

$$\textbf{Anode: } 2Cl^- \rightarrow Cl_2(g) + 2e^-$$
$$\textbf{Cathode: } Sr^{2+} + 2e^- \rightarrow \textbf{Sr(in Bi)}$$

Selectively removing Ba, Sr, and Cs from contaminated electrorefiner molten salt electrolytes by leveraging the strong atomic interactions between liquid metals and alkali/alkaline-earth elements will reduce the volume of nuclear waste relegated to permanent storage by allowing for extended use of the electrolyte instead of frequent disposal. Recovery of A in a liquid metal electrode will allow for them to later be separated as oxides (BaO-SrO-Cs_2O) through an oxidation treatment for long-term storage as ceramic or glass waste forms, but at a much lower volume than disposing of the entire LiCl-KCl-ACl_z electrolyte (Figure 6).

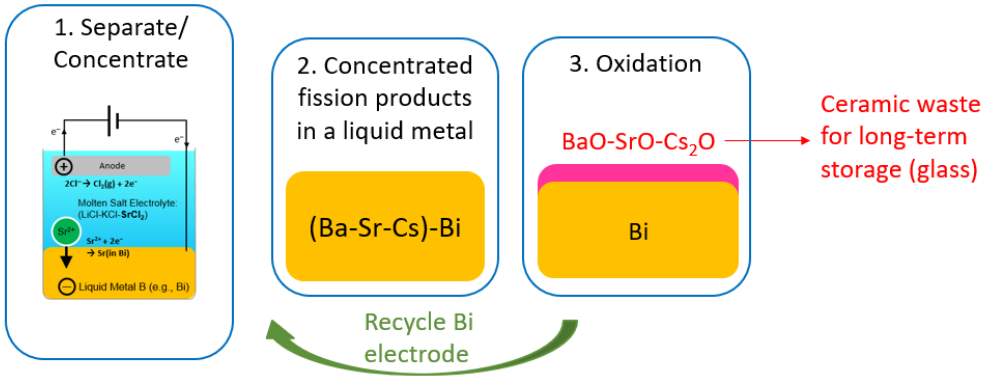

Figure 6. Proposed process for removing A from electrorefiner salts using liquid metal cathodes, followed by oxidation treatments to develop oxide wasteform**.**

2. Outcomes of the Project

2.1 Thermodynamic Properties of Binary Alloys

2.1.1 Experimental Approach

In order to assess the viability of various liquid metal electrodes for removing alkali/alkaline-earths, thermodynamic data including activity are necessary as the strength of the atomic interactions and therefore the shifts in reduction potentials depend on these properties. Activity data for AE-M systems (where AE = Ba, Sr) is sparse or absent in available literature and many of the accepted phase diagrams are incomplete or contain unstable phases [5,6]. To gain a more complete understanding and provide valuable fundamental thermodynamic data on these binary systems, electromotive force measurements were conducted.

The electromotive force method is an elegant approach to measure partial Gibbs energies using a galvanic cell with no external current flowing, relying on the notion that the amount of work necessary to transfer one mole of an element in valence state *z* from its pure state into a solution or compound is related to the transfer of charge by:

$$\Delta G = -zFE \tag{2}$$

, where *E* is the electromotive force produced by the cell [8,9]. In order to accurately measure the electromotive force between AE(s) and AE-M alloys, the following electrochemical cell was devised:

$$\text{AE(s)}|\text{CaF}_2\text{-AEF}_2|\text{AE(in M)} \tag{3}$$

, where pure alkaline-earth metal (AE) acts as the reference electrode (RE), solid CaF_2-AEF_2 (97-3 mol%) as the electrolyte, and AE-M alloys as working electrodes (WE). In this electrochemical cell, the half-cell reactions are:

$$\text{WE: } \text{AE}^{2+} + 2e^- = \text{AE(in M)} \tag{4}$$

$$\text{RE: } \text{AE}^{2+} + 2e^- = \text{AE(s)}$$

, and the overall cell reaction is:

$$\text{AE(s)} = \text{AE(in M)} \tag{5}$$

The change in partial molar Gibbs energy of AE, $\Delta\bar{G}_{\text{AE}}$, for this reaction is given by:

$$\Delta\bar{G}_{\text{AE}} = \bar{G}_{\text{AE(in M)}} - G^0_{\text{AE(s)}} = RT\ln(a_{\text{AE}}) \tag{6}$$

, where $\bar{G}_{\text{AE(in M)}}$ is the partial molar Gibbs energy of AE in liquid metal M and $G^0_{\text{AE(s)}}$ is the chemical potential of pure AE. By applying the Nernst equation to Eq. (1), the change in partial molar Gibbs energy of AE in a given M (and thus activity) is directly related to the cell emf, *E*:

$$E = -\frac{\Delta\bar{G}_{\text{AE}}}{zF} = -\frac{RT}{zF}\ln(a_{\text{AE(in M)}}) \tag{7}$$

One of the most difficult aspects of designing an electrochemical system is the choice of electrolyte; CaF_2-AEF_2 (97-3 mol%) was selected because it satisfies several necessary conditions for a reliable electrolyte [8]:

- Electrolyte choice must provide purely ionic conductivity in the temperature range of cell operation
- Any side reactions between the electrodes and electrolyte must be avoided.

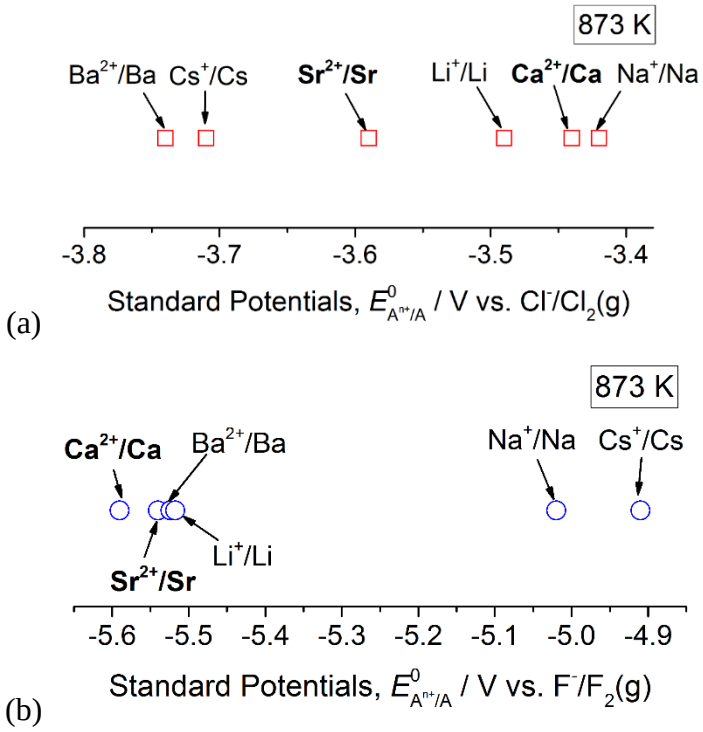

Figure 7. Comparison of standard electrode potentials of selected alkali/alkaline-earth elements calculated using the standard free energies of formation of (a) pure chlorides and (b) pure fluorides at 873 K [2].

Constructing an electrochemical cell to effectively meet these requirements for AE-M alloys is technically challenging due to (i) the high reactivity of pure AE as well as AE-M alloys which can degrade the electrolytes or cell components during emf measurements, and (ii) the high melting temperatures of pure AE ($T_{m,\,Ba}$ = 1000 K, $T_{m,\,Sr}$ = 1042 K) [10] and AE-M alloys. The solid-state CaF_2 is well known to have substantial ionic conductivity (1.5×10^{-3} S cm^{-1} at 1073 K) [11,12], suitable for emf measurements. In recent studies, solid-state CaF_2 electrolyte has been utilized in determining the thermodynamic properties of Ca-Bi, Ca-Sb, and Ca-Mg alloys at 723–1100 K [13–15], employing the high stability of CaF_2 electrolyte in emf measurements of calcium alloys. Delcet and Egan [16] also determined the emf values of Ca-Ag and Ca-In alloys using single-crystal CaF_2 at 1073 K via coulometric titration techniques and derived thermodynamic activity values of calcium.

The investigation of Sr-M alloys required using CaF_2-AEF_2 (97-3 mol%) instead of the pure CaF_2 electrolyte to account for the change in electroactive species. According to the analysis of standard electrode potentials in the fluoride system at 873 K (Figure 7a), CaF_2 is more stable than both BaF_2 and SrF_2 thus, strontium/barium ions are expected to be the most electroactive

species in the CaF_2-AEF_2 binary electrolyte. In contrast, $BaCl_2$ and $SrCl_2$ are more stable than $CaCl_2$ in the chloride system (Figure 7b); therefore, calcium becomes the most electroactive species, invalidating the stable emf measurements of AE-based alloys in $CaCl_2$-$AECl_2$ electrolyte due to side reactions (e.g., $Sr + CaCl_2 = SrCl_2 + Ca$, $\Delta_r G = -28.9$ kJ at 873 K).

Final assembly of the electrochemical cell was performed in a glovebox under an inert argon environment (O_2 concentration < 0.5 ppm) to mitigate the rapid oxidation of AE and AE-M alloys. The CaF_2-AEF_2 electrolyte was placed in an alumina crucible (8.2 cm diameter × 3.0 cm height) and tungsten wires (1 mm × 46 cm in diameter and length) were inserted into alumina tube sheaths, sealed at the top with epoxy, passed through the stainless steel test chamber, through the CaF_2-AEF_2 caps, and into the electrodes (Figure 8). The caps were installed to minimize the contamination of alloys during the measurements by physically blocking the vapor-phase transport of strontium.

The test chamber was then sealed, removed from the glovebox, loaded into a crucible furnace, and evacuated to ~1 Pa. The test chamber was heated at 373 K for 12 h, at 543 K for 12 h under vacuum to remove residual moisture and oxygen, purged three times with high purity argon, and finally heated to 1023 K under flowing argon (~10 mL min^{-1}) atmosphere to melt the electrodes and establish electrical contact with the tungsten wires.

Emf measurements were performed by measuring the potential difference between the reference electrode and each working electrode (AE-M alloys) sequentially in 180 s intervals during thermal cycles using a potentiostat-galvanostat (Autolab PGSTAT302N, Metrohm AG). Emf data were collected throughout a cooling and reheating cycle between ~700 and 1100 K in 25 K increments. The cell temperature was held constant at each increment for 1.5 h to reach thermal and electrochemical equilibria and ramped at ±5 K min^{-1} between increments. The cell temperature was measured using a thermocouple (ASTM type-K) located at the center of the electrolyte, and thermocouple data acquisition system (NI 9211, National Instruments).

The following sections summarize the work performed towards the thermodynamic measurements of AE-M systems, specifically the Sr-(Bi, Sb, Pb) and Ba-(Bi, Sb). Herein, the thermodynamic quantities as a function of both temperature and composition for all systems are reported in their entirety. In addition, the deviations between experimental procedures are given to allow for maximum reproducibility of the results reported in this section.

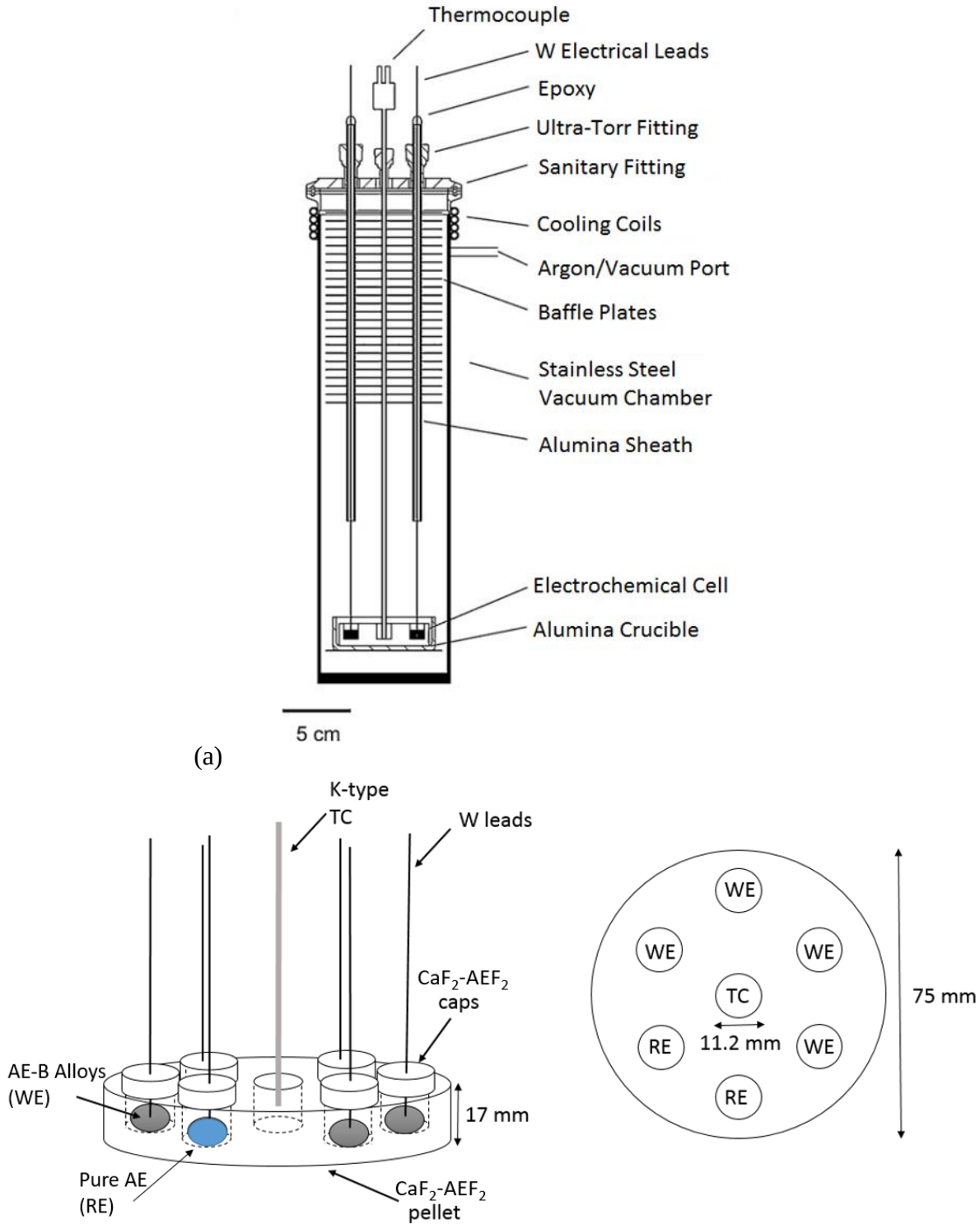

Figure 8. (a) Experimental assembly for electromotive force measurements utilizing the AE(s)|CaF_2-AEF_2|AE(in M) electrochemical cell and (b) close-up schematic of electrochemical cell.

2.1.2 Electromotive Force Measurements on the Sr-Bi System

The use of pure strontium metal as reference electrodes caused gradual degradation of the solid-state CaF_2-SrF_2 electrolytes, resulting in irreproducible emf values during thermal cycles (Figure 9).

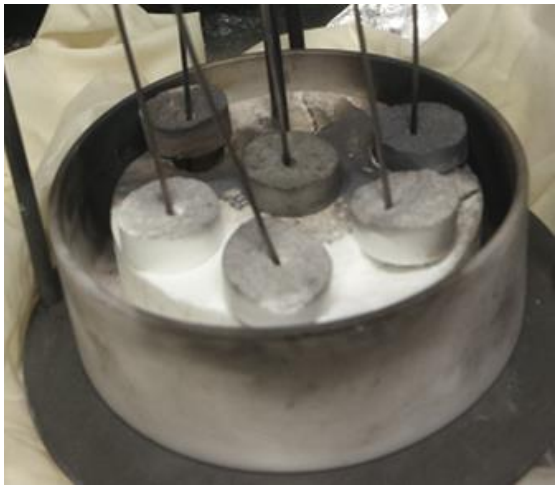

Figure 9. Reaction of the pure Sr electrode with the CaF_2-SrF_2 (97-3 mol%) electrolyte indicated by the darkening of the electrolyte, which leads to the degradation of the electrochemical cell and irreproducible emf measurements.

Instead, a less reactive Sr-Bi alloy (x_{Sr} = 0.10) was employed as the reference electrode in emf measurements of various alloy compositions in a manner similar to Newhouse et al. [15]. The choice of the Sr-Bi alloy x_{Sr} = 0.10 was advantageous because this alloy composition (1) experiences no phase changes at 700−1100 K, resulting in a linear thermal emf (dE_{cell}/dT); (2) produced highly reproducible emf values for various Sr-Bi alloys during the thermal cycle; and (3) the potential difference between identical x_{Sr} = 0.10 electrodes remained less than ±5 mV throughout the emf measurements, implying an excellent stability as a reference electrode.

In separate experiments, the electrode potential of the Sr-Bi alloy x_{Sr} = 0.10 was determined against pure Sr using a Sr(s)|CaF_2-SrF_2|Sr-Bi(x_{Sr} = 0.10) cell (Figure 10a). By performing several measurements with shorter hold times at each increment (1 h) and only one heating/cooling cycle, the pure Sr electrode reactivity was minimized and a reliable calibration curve was obtained. Using the linear fit of this measurement at x_{Sr} = 0.10 (Figure 10b), the emf values of Sr-M alloys E_{cell} are reported versus to pure Sr metal:

$$E_{RE} = 6.9 \times 10^{-5}\ T + 0.922\ [V] \quad \text{vs. pure Sr} \qquad (8)$$

, which allows the measured emf between the Sr-Bi (x_{Sr} = 0.10) reference electrode and the Sr-Bi working electrodes to be directly related to the emf between the Sr-Bi working electrodes and pure Sr:

$$E = E_{cell} + E_{RE} \qquad (9)$$

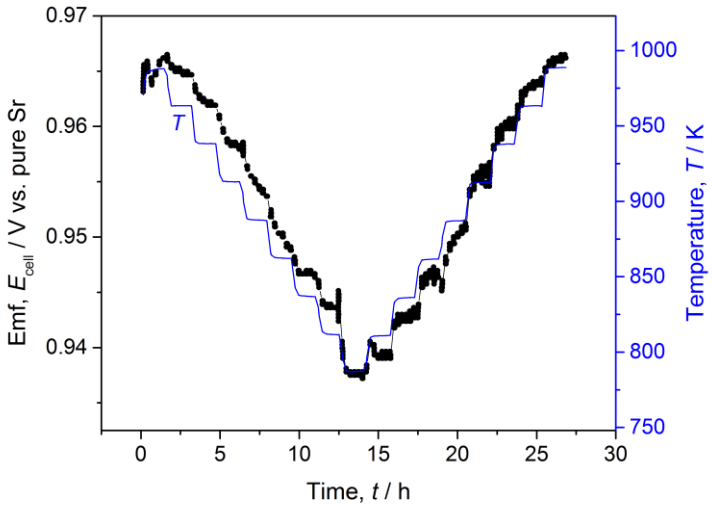

(a)

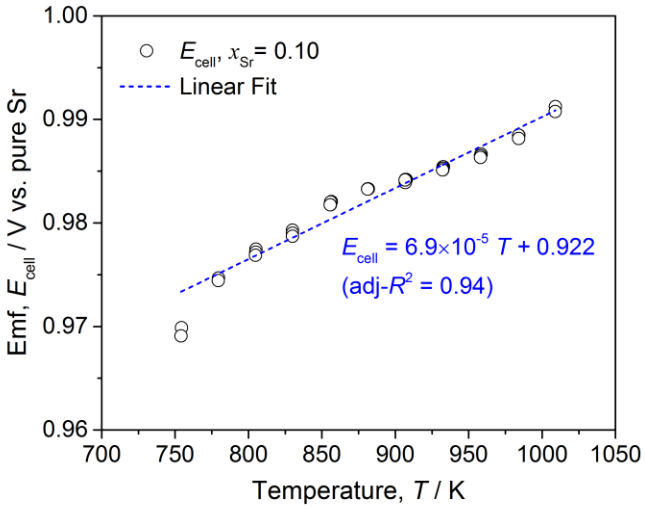

(b)

Figure 10. (a) Electromotive force data as a function of time (blue) with temperature (red) for the electrochemical cell Sr(s)|CaF_2-SrF_2(s)|Sr-Bi (x_{Sr} = 0.10) and (b) emf values as a function of temperature obtained from the aforementioned electrochemical cell.

Electromotive force data can be used to calculate fundamental thermodynamic properties including activity, partial molar entropy, partial molar enthalpy, and partial molar excess Gibbs energy. The emf data as function of time is presented below in Figure 11 and is re-plotted as a function of temperature in Figure 12.

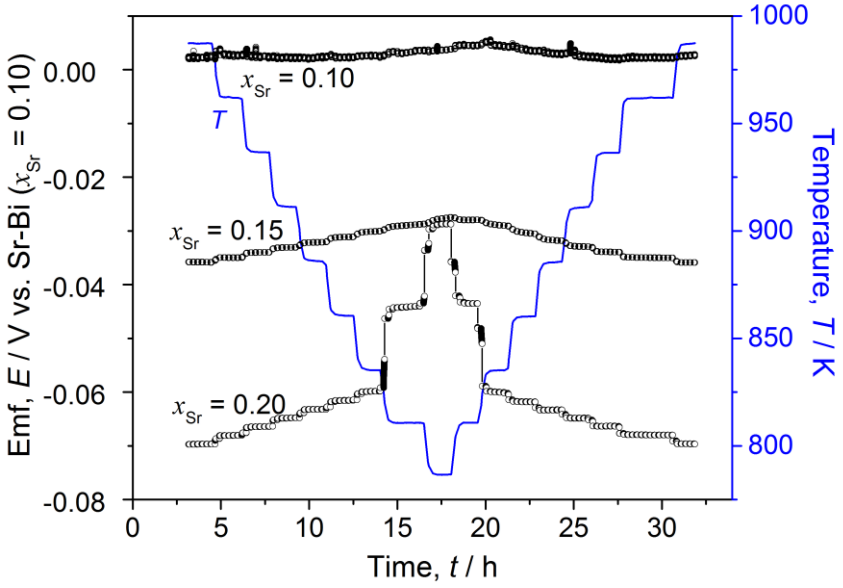

Figure 11. Emf values and temperature measured as a function of time upon cooling and heating a Sr-Bi (x_{Sr} = 0.10)|CaF_2-SrF_2(s)|Sr(in Bi) cell with Sr-Bi alloys x_{Sr} = 0.10, 0.15, and 0.20.

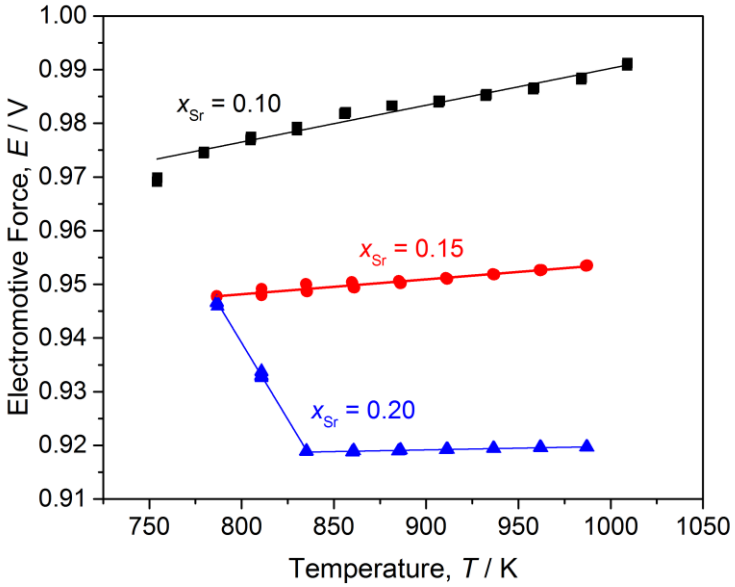

Figure 12. Emf values as a function of temperature upon cooling and heating a Sr-Bi (x_{Sr} = 0.10)|CaF_2-SrF_2(s)|Sr(in Bi) cell with Sr-Bi alloys x_{Sr} = 0.10, 0.15, and 0.20.

The change in the partial molar entropy of strontium, $\Delta\bar{S}_{Sr}$, is calculated from linear fits of the measured emf data in Figure 12 using the following thermodynamic relation, where $\left(\frac{\partial E}{\partial T}\right)_P$ is the slope of the fits:

$$\Delta\bar{S}_{Sr} = -\left(\frac{\partial \Delta\bar{G}_{Sr}}{\partial T}\right)_P = zF\left(\frac{\partial E}{\partial T}\right)_P \quad (10)$$

By re-plotting the emf data again as E_{cell}/T vs. $1/T$ (Figure 13), the partial molar enthalpy of strontium, $\Delta\bar{H}_{Sr}$, can be determined using the Gibbs-Helmholtz relation:

$$\Delta\bar{H}_{Sr} = -T^2\left(\frac{\partial(\Delta\bar{G}_{Sr}/T)}{\partial T}\right)_P = zFT^2\left(\frac{\partial(E/T)}{\partial T}\right)_P = zF\frac{\partial(E/T)}{\partial(1/T)} \quad (11)$$

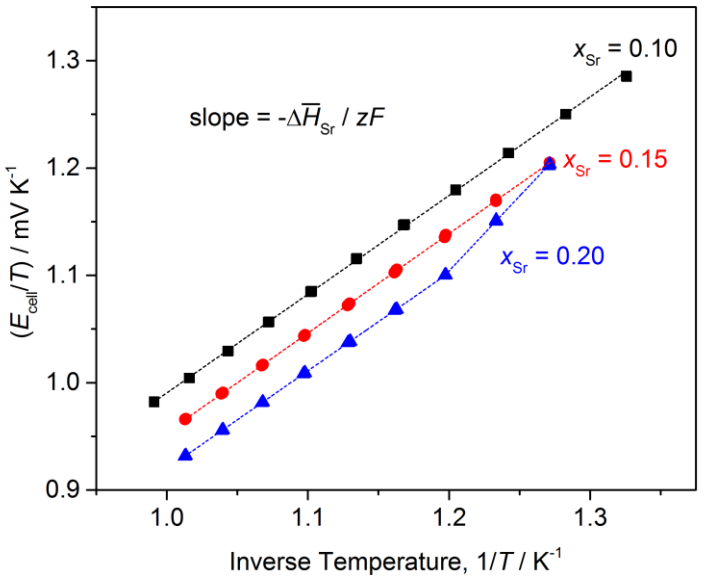

Figure 13. Graphical representation of *E*/T vs. 1/T to estimate the change in partial molar enthalpy of Sr-Bi alloys x_{Sr} = 0.10-0.20, where the slope is -$\Delta\bar{\boldsymbol{H}}_{Sr}/zF$.

Using the Nernst equation, the activity of Sr can be calculated at a given temperature using the emf values:

$$\ln(a_{Sr}) = -\frac{zFE}{RT} \quad (12)$$

The excess partial molar Gibbs energy of Sr, $\bar{G}_{Sr}^{E}$, can then calculated from the activity data:

$$\bar{G}_{Sr}^{E} = RT\ln\gamma_{Sr} = RT(\ln a_{Sr} - \ln x_{Sr}) \quad (13)$$

, where γ_{Sr} is the activity coefficient.

Emf measurements recorded as a function of temperature provide a wealth of thermodynamic data, which allows for a more complete understanding of the capability of each liquid metal (Bi, Sb, Sn) to separate Sr from molten salt electrolytes.

The variation of emf with temperature and composition for Sr-Bi alloys (x_{Sr} = 0.05−0.75) is displayed in Figure 14a-c, obtained upon cooling and reheating the electrochemical cells between 1023 and 748 K [7]. In general, the emf values were in close agreement between the cooling and heating with less than a 5 mV difference up to x_{Sr} = 0.30. In Figure 14a, the emf varies linearly with respect to temperature and increases as x_{Sr} decreases above the liquidus [L = L + $SrBi_3$(s)]; below the liquidus line, the emf does not change with composition and the emf values collapse onto the same line. This is because the emf values are analogous to activity and activity is constant with respect to composition in a two-phase region. In Figure 14b, mole fraction x_{Sr} = 0.30 exhibits two phase transitions, a liquidus [L = L + Sr_2Bi_3] at 908 K and a solidus [L + Sr_2Bi_3 = $SrBi_3$+ Sr_2Bi_3] at 843 K.

Emf values of alloys with high strontium content (0.35 ≤ x_{Sr} ≤ 0.75) exhibited increased hysteresis between the heating-cooling cycles up to a 25 mV difference possibly due to the increased reactivity. For this reason, emf data for high Sr alloys (x_{Sr} ≥ 0.35) were collected from the first cooling cycle only (Figure 14b-c). Mole fraction x_{Sr} = 0.45 exhibited a solidus transition [L + $Sr_{11}Bi_{10}$ = Sr_2Bi_3 + $Sr_{11}Bi_{10}$] at 908 K (Figure 14b); mole fraction x_{Sr} = 0.55 exhibited a solidus phase transition [L + Sr_4Bi_3 = $Sr_{11}Bi_{10}$ + Sr_4Bi_3] at ~985 K (Figure 14c). The transition reactions were inferred based on the observed crystal structures at each composition. It should be noted that the observed crystal structures of the Sr_2Bi_3 and Sr_4Bi_3 phases are well reported in the database, but not included in the most recent Sr-Bi equilibrium phase diagrams.

The change in the partial molar entropy of strontium, $\Delta\bar{S}_{Sr}$, was calculated from linear fits of the measured emf data in Figure 14a-c (Eq. 10). Similarly, the change in the partial molar enthalpy, $\Delta\bar{H}_{Sr}$, was calculated using the Gibbs-Helmholtz relation (Eq. 11). As shown in Figure 13 for Sr-Bi alloys x_{Sr} = 0.05−0.15, the change in partial molar enthalpy was estimated based on the slopes by plotting *E/T* versus 1/*T*. The estimated partial molar quantities as well as the linear fits of temperature-dependent emf values are summarized in Table 1.

Using the Nernst equation (Eq. 12), the activity of Sr in Bi, a_{Sr}, was calculated for specific temperatures of 788 K, 888 K, and 988 K using the measured emf values. The excess partial molar Gibbs energy of Sr, $\bar{G}_{Sr}^{E}$, was then calculated from the activity data (Eq. 13). The results of emf values, natural log of the activity, and the excess partial molar Gibbs energy are summarized in Table 2 and are presented graphically in Figure 15a−c at 888 K.

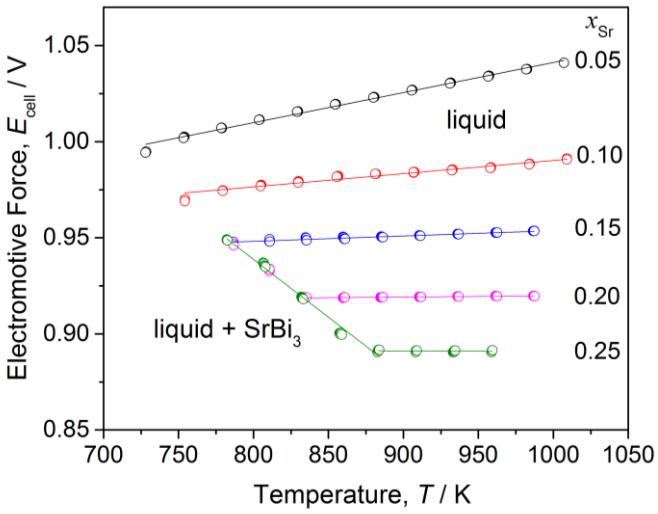

(a)

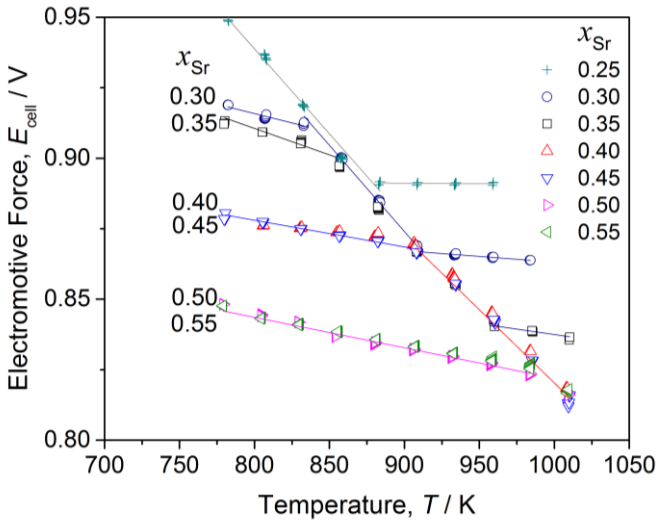

(b)

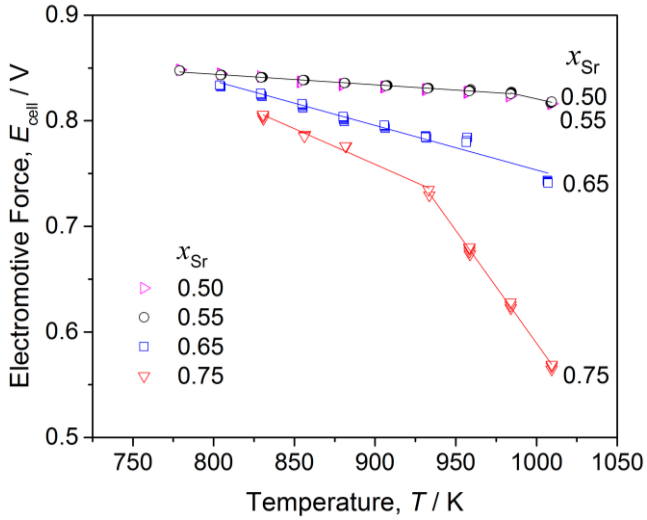

(c)

Figure 14. Emf values of various Sr-Bi alloys versus pure Sr, E, as a function of temperature for (a) x_{Sr} = 0.05 to x_{Sr} = 0.25, (b) x_{Sr} = 0.25 to x_{Sr} = 0.55, and (c) x_{Sr} = 0.55 to x_{Sr} = 0.75.

Table 1. Measured partial molar entropies and partial molar enthalpies for Sr-Bi alloy compositions x_{Sr} = 0.05 to x_{Sr} = 0.75 as well as linear fits of emf values.

x_{Sr}	T (K)	$\partial E/\partial T$ (μV K^{-1})	$\partial(E/T)/\partial(1/T)$ (mV)	$\Delta\bar{S}_{Sr}$ (J mol^{-1} K^{-1})	$\Delta\bar{H}_{Sr}$ (kJ mol^{-1})
0.05	728-1007	157	883	30.3	-170.4
0.10	754-1009	69.2	919	13.4	-177.3
0.15	786-987	27.7	926	5.3	-178.7
0.20	835-987	6.4	913	1.2	-176.2
0.20	786-835	-570	1395	-110	-269.2
0.25	883-959	0.8	914	0.2	-176.4
0.25	782-883	-602	1469	-116	-283.5
0.30	908-984	-40.7	904	-7.9	-174.4
0.30	831-908	-611	1423	-118	-274.6
0.30	782-831	-133	1023	-25.7	-197.4
0.35	959-1010	-76.6	964	-14.8	-186.0
0.35	831-959	-527	1327	-101.7	-256.1
0.35	780-831	-181	1039	-34.9	-200.5
0.40	867-1010	-508	926	-98	-178.7
0.40	780-867	-62	1324	-12	-255.5
0.45	959-1010	-519	1197	-100.2	-231.0
0.45	780-959	-94.7	928	-18.3	-179.1
0.50	983-1009	-292	1111	-56.3	-214.4
0.50	779-983	-108	931	-20.8	-179.7
0.55	984-1009	-346	1167	-66.8	-225.2
0.55	779-984	-100	925	-19.3	-178.5
0.65	804-1007	-422	1169	-81.4	-225.6
0.75	933-1009	-2200	2725	-424.5	-525.8
0.75	830-933	-676	1265	-130.4	-244.1

Table 2. Measured emf, natural log of the activity of Sr in Bi, and the measured excess partial molar Gibbs energy of strontium of x_{Sr} = 0.05 to x_{Sr} = 0.75.

x_{Sr}	E (V)			ln a_{Sr}			$\bar{G}^{E}_{Sr}$ (kJ mol^{-1})		
	788 K	888 K	988 K	788 K	888 K	988 K	788 K	888 K	988 K
0.05	1.008	1.024	1.039	-29.7	-26.8	-24.4	-175	-176	-176
0.10	0.976	0.982	0.989	-28.7	-25.7	-23.2	-173	-173	-172
0.15	0.948	0.951	0.953	-27.9	-24.9	-22.4	-170	-170	-168
0.20	0.946	0.919	0.920	-27.9	-24.0	-21.6	-172	-165	-164
0.25	0.946	0.891	0.891	-27.9	-23.3	-20.9	-174	-162	-160
0.30	0.919	0.881	0.864	-27.1	-23.0	-20.3	-170	-161	-157
0.35	0.912	0.879	0.838	-26.9	-23.0	-19.7	-169	-162	-153
0.40	0.878	0.880	0.829	-25.9	-23.0	-19.5	-164	-163	-153
0.45	0.879	0.870	0.826	-25.9	-22.7	-19.4	-164	-162	-153
0.50	0.845	0.834	0.822	-24.9	-21.8	-19.3	-159	-156	-153
0.55	0.845	0.835	0.824	-24.9	-21.8	-19.4	-159	-157	-154
0.65	0.843	0.801	0.758	-24.8	-20.9	-17.8	-160	-151	-143
0.75	0.836	0.769	0.610	-24.6	-20.1	-14.3	-159	-146	-115

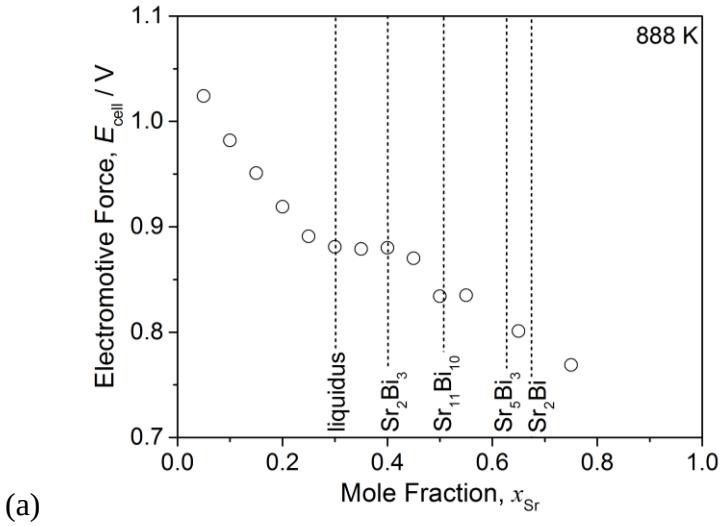

(a)

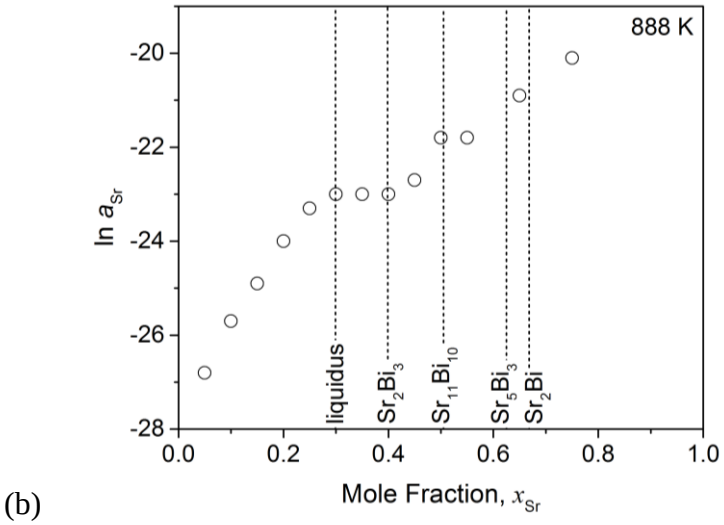

(b)

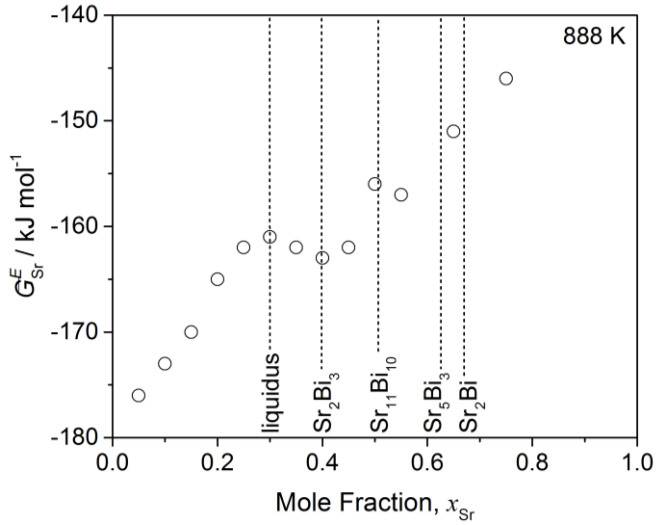

(c)

Figure 15. (a) Measured emf values (E) vs. pure Sr (s), (b) natural logarithm of activity in Sr (ln a_{Sr}), and (c) excess partial molar Gibbs energy ($\overline{\boldsymbol{G}}^{E}_{Sr}$) as a function of mole fraction x_{Sr} at 888 K.

Figure 15a displays the emf values as a function of strontium mole fraction with the phase compositions of each intermetallic compound as well as liquidus composition at 888 K. In the two-phase region [L+ Sr_2Bi_3] at $0.30 < x_{Sr} < 0.40$, the emf is nearly constant because chemical potential (or activity) of Sr becomes invariant with respect to x_{Sr} in two-phase regions (Figure 15a-b). However, in the two-phase region [Sr_2Bi_3 + $Sr_{11}Bi_{10}$] at $0.40 < x_{Sr} < 0.52$, different emf values were obtained within the same two-phase region, indicating non-equilibrium phase behavior. According to the equilibrium phase diagram, we anticipate that the emf values will approach zero in the two-phase composition domain [Sr_2Bi + Sr] at $x_{Sr} > 0.67$, as observed in the Ca-Bi system [13]. However, the emf value at $x_{Sr} = 0.75$ remained above 0.75 V versus pure Sr. This discrepancy was due to the formation of meta-stable phases at this composition, comprised of Sr_2Bi, Sr_5Bi_3, and Sr_4Bi_3 without pure Sr phase. In the Sr-Bi system, a large excess partial molar Gibbs energy (as low as -176 kJ mol^{-1} at $x_{Sr} = 0.05$) was obtained, indicating highly non-ideal solution behavior due to the strong chemical interactions between Sr and Bi (Figure 15c).

This study has determined thermodynamic properties of the binary Sr-Bi system, including activities, partial molar entropies, enthalpies, and excess Gibbs energies. The liquid-state solubility of Sr in Bi was estimated to be ~15 mol% at 788 K and ~40 mol% at 988 K. At high Sr compositions ($x_{Sr} \geq 0.25$), strong non-equilibrium phase behavior was observed; for example, three phases in the binary system and the absent pure Sr phase at $x_{Sr} > 0.67$. In addition, two additional phases of Sr_2Bi_3 and Sr_4Bi_3 were considered in describing the phase behavior of Sr-Bi system, which are not considered in the current Sr-Bi equilibrium phase diagram. Combining the high liquid-state solubility and the strong chemical interactions between Sr and Bi (a_{Sr} as low as 1.2×10^{-13}), Bi shows promise as an electrode material for separating dissolved strontium ions (Sr^{2+}) from molten salt electrolytes (e.g., LiCl-KCl-$SrCl_2$).

2.1.3 Electromotive Force Measurements on the Sr-Sb System

A large amount of metal vapor was observed during the arc-melting of Sr-Sb alloys for electromotive force measurements, which led to the concern that the Sr-Sb alloys could differ from the intended compositions. Induction Coupled Plasma-Atomic Emission Spectroscopy (ICP-AES, Perkin-Elmer Optima 5300DV) was used to verify the compositions of the arc-melted Sr-Sb alloys with a maximum of 4 % error of the measured value. As x_{Sr} increased, so did the discrepancy between the actual composition and the nominal composition likely as a result of increased Sr vaporization during the arc melting process (Table 3). Compositions are referred to using their ICP-AES measured values instead of the as-weighed compositions prior to arc-melting.

Using the electrochemical cell Sr-Bi ($x_{Sr} = 0.10$)|CaF_2-SrF_2(s)|Sr(in Sb) and the aforementioned experimental procedure, emf values were recorded over a temperature range of 833-1113 K for sixteen Sr-Sb alloy compositions ranging from $x_{Sr} = 0.03$ to $x_{Sr} = 0.84$ [17]. Due to undercooling effects (hysteresis between heating/cooling cycles of > 20 mV), only the heating curves were considered in the analysis [18]. Electromotive force measurements were plotted as a function of temperature for all measured mole fractions (Figure 16a-b).

Table 3. Comparison of mole fraction, x_{Sr} between as weighed and as measured by ICP-AES.

Mole Fraction, x_{Sr}	
Nominal (as weighed)	Measured (ICP-AES)
0.025	0.03
0.050	0.04
0.075	0.07
0.100	0.09
0.150	0.14
0.200	0.20
0.250	0.23
0.300	0.30
0.350	0.33
0.400	0.38
0.450	0.43
0.500	0.48
0.550	0.52
0.600	0.57
0.650	0.60
0.700	0.62
0.750	0.69
0.900	0.84

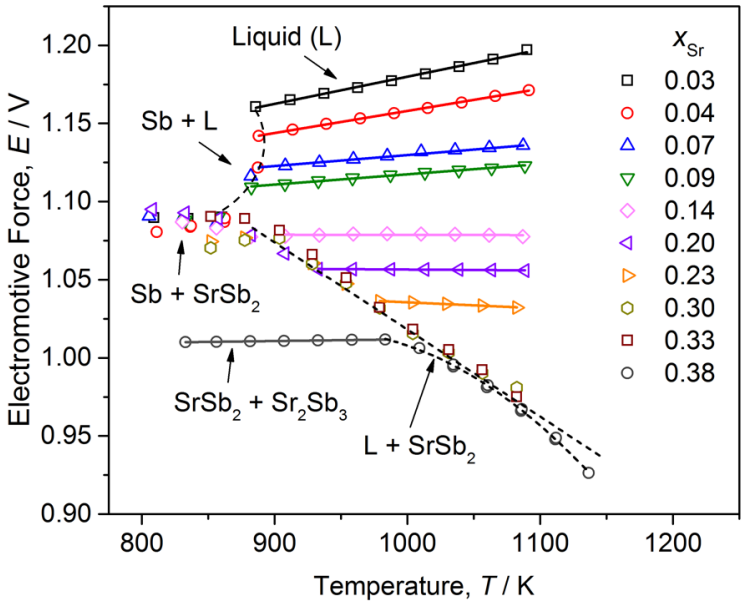

(a)

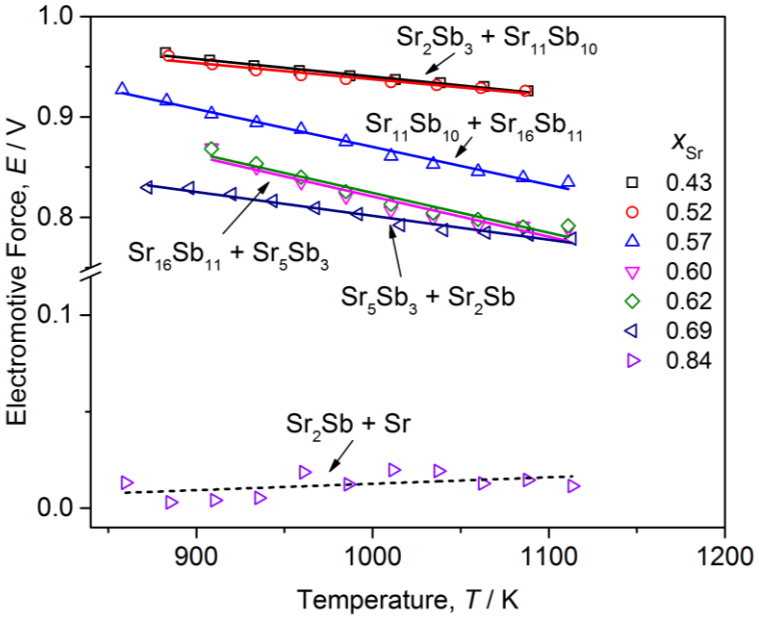

(b)

Figure 16. Emf values of various Sr-Sb alloys versus pure Sr, E_{cell}, as a function of temperature for (a) x_{Sr} = 0.03 to x_{Sr} = 0.53 and (b) x_{Sr} = 0.43 to x_{Sr} = 0.84.

Emf decreases linearly as a function of temperature above the liquidus, while below the liquidus the activity of Sr is invariant as a function x_{Sr}, as the system enters a two-phase region and the emf values collapse onto the same curve. This is because activity is constant in a two-phase region and emf is directly related to activity via the Nernst equation (Eq. 12). As such, phase transitions are indicated in the plots by changes in the slope of the emf, i.e. changes in the partial molar entropy (Eq. 10). At temperatures lower than 875 K, the emf values are less reproducible

and more scattered; this is believed to be due decreased ionic conductivity in the electrolyte at lower temperatures as well as worsening contact between the electrolyte and Sr-Sb alloy electrodes due to the absence of any liquid phase. Higher mole fractions ($x_{Sr} > 0.55$) experienced the least stability with emf variability of up to 50 mV between runs due to increased Sr content in the alloys degrading the electrolyte as well as the high melting temperature of these alloys that prevented intimate contact between the electrode and the electrolyte. Figure 16b shows the effect of transitioning into the $SrSb_2$ + Sr two-phase region with the $x_{Sr} = 0.84$ alloy, as the presence of pure Sr leads to a dramatic decrease in the emf as the activity of pure Sr is unity. The electromotive force data was used to calculate the change in partial molar entropy ($\Delta\bar{S}_{Sr}$) and partial molar enthalpy ($\Delta\bar{H}_{Sr}$) in linear regions (Table 4).

Table 4. Measured partial molar entropies and partial molar enthalpies for Sr-Sb alloy compositions $x_{Sr} = 0.03$ to $x_{Sr} = 0.69$ as well as linear fits of emf values. Errors of the linear fits are represented by parentheses.

x_{Sr}	T (K)	$\partial E/\partial T$ ($\mu V\ K^{-1}$)	$\partial(E/T)/\partial(1/T)$ (mV)	$\Delta\bar{S}_{Sr}$ ($J\ mol^{-1}\ K^{-1}$)	$\Delta\bar{H}_{Sr}$ ($kJ\ mol^{-1}$)	Adj-R^2
0.03	886-1090	174 (4)	1006 (4)	33.6	-194.1	0.996
0.04	888-1092	142 (2)	1017 (2)	27.3	-196.2	0.999
0.07	908-1087	73 (3)	1057 (3)	14.2	-203.9	0.986
0.09	882-1089	66 (2)	1052 (2)	12.7	-202.9	0.994
0.14	908-1087	-1 (4)	1080 (4)	-0.2	-208.4	-0.154
0.20	860-933	-435 (9)	1462 (8)	-83.9	-282.1	0.999
0.20	933-1089	-6 (1)	1062 (1)	-1.1	-205.0	0.764
0.23	928-979	-484 (21)	1510 (20)	-93.4	-291.4	0.996
0.23	979-1082	-38 (2)	1074 (2)	-7.4	-207.3	0.987
0.30	904-1082	-543 (16)	1565 (16)	-104.8	-302.0	0.994
0.33	877-1082	-573 (14)	1596 (14)	-110.6	-308.0	0.995
0.38	833-983	11 (1)	1001 (0)	2.1	-193.1	0.981
0.43	882-1089	-176(8)	1116(8)	-33.9	-215.4	0.984
0.52	884-1087	-162(13)	1099(12)	-31.2	-212.2	0.951
0.57	858-1111	-378 (14)	1248 (14)	-72.8	-240.8	0.987
0.60	908-1111	-400(45)	1221(45)	-77.3	-235.6	0.909
0.62	908-1111	-396(35)	1221(35)	-76.5	-235.6	0.942
0.69	873-1113	-238(13)	1039(13)	-45.9	-200.6	0.971

Using the Nernst equation, the activity of Sr in Sb was calculated for each alloy at 888 K, 988 K, and 1088 K and the partial molar excess Gibbs free energy ($\bar{G}_{Sr}^{E}$) was also calculated. The resulting values are listed below in Table 5 and are depicted graphically for T = 988 K in Figure 17a-c.

Table 5. Measured emf, natural log of the activity of Sr in Sb, and the measured excess partial molar Gibbs energy of strontium for mole fractions x_{Sr} = 0.03 to x_{Sr} = 0.84.

x_{Sr}	E (V)			ln a_{Sr}			$\bar{G}_{Sr}^{E}$ (kJ mol^{-1})		
	888 K	988 K	1088 K	888 K	988 K	1088 K	888 K	988 K	1088 K
0.03	1.161	1.178	1.195	-30.3	-27.7	-25.5	-197	-197	-197
0.04	1.143	1.157	1.171	-29.9	-27.2	-25.0	-197	-197	-198
0.07	1.122	1.129	1.136	-29.3	-26.5	-24.2	-197	-196	-195
0.09	1.111	1.117	1.124	-29.0	-26.2	-24.0	-196	-196	-195
0.14	1.079	1.079	1.079	-28.2	-25.3	-23.0	-194	-192	-191
0.20	1.075	1.056	1.055	-28.1	-24.8	-22.5	-196	-190	-189
0.23	1.080	1.036	1.033	-28.2	-24.3	-22.0	-198	-188	-186
0.30	1.083	1.029	0.974	-28.3	-24.2	-20.8	-200	-189	-177
0.33	1.087	1.030	0.973	-28.4	-24.2	-20.8	-202	-190	-178
0.38	1.011	1.014	0.968	-26.4	-23.8	-20.7	-188	-188	-178
0.43	0.964	0.941	0.925	-25.2	-22.1	-19.7	-180	-175	-171
0.52	0.959	0.939	0.926	-25.1	-22.1	-19.8	-180	-176	-173
0.57	0.912	0.875	0.837	-23.8	-20.6	-17.9	-172	-164	-157
0.60	0.882	0.816	0.786	-23.1	-19.2	-16.8	-166	-153	-147
0.62	0.880	0.824	0.792	-23.0	-19.4	-16.9	-166	-155	-149
0.69	0.828	0.804	0.780	-21.6	-18.9	-16.6	-157	-152	-147
0.84	0.014	0.014	0.013	-0.4	-0.3	-0.3	-1	-1	-1

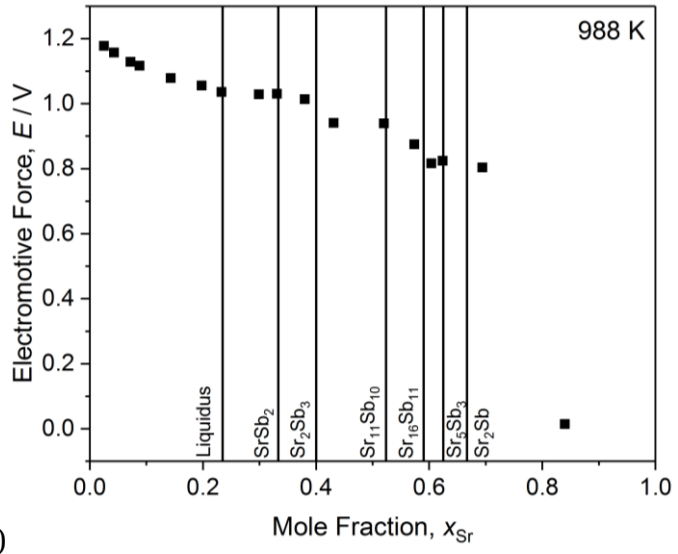

(a)

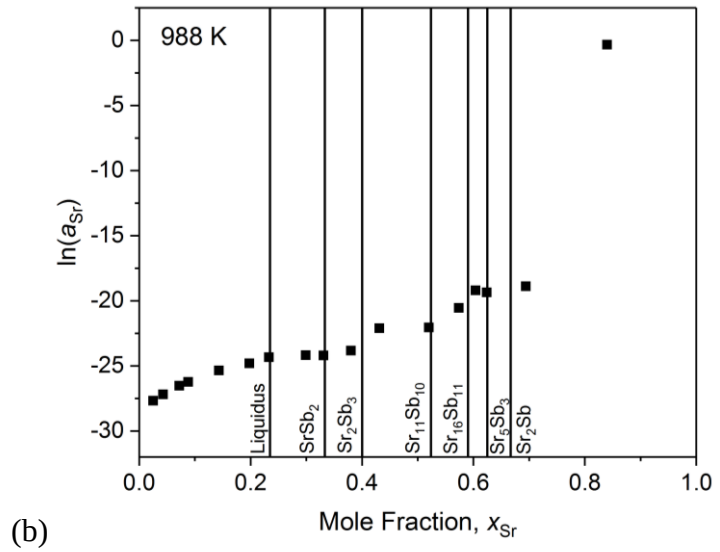

(b)

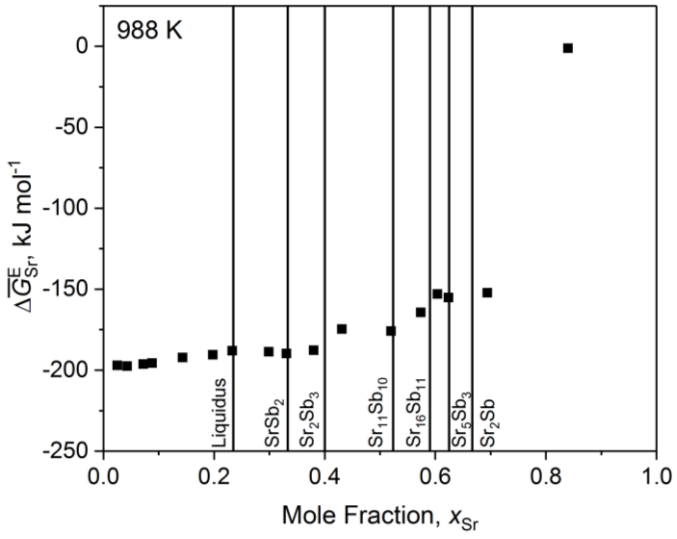

(c)

Figure 17. *(*a) Measured emf values (*E*) vs. pure Sr, (b) natural log of activity (ln a_{Sr}), and (c) excess molar partial Gibbs energy ($\bar{\mathbf{G}}^{E}_{Sr}$) as a function of x_{Sr} at 988 K.

Figure 17a presents the emf values as a function of Sr mole fraction (x_{Sr}) with the liquidus composition and proposed intermetallic phases superimposed at 988 K. The emf clearly decreases as a function of x_{Sr} until hitting the liquidus composition, at which point the emf becomes essentially constant with respect to x_{Sr} in the two-phase regions; this invariance is a result of the chemical potential of Sr being constant in two-phase regions. Figure 17b and Figure 17c depict the natural logarithm of activity of Sr in Sb and the partial molar excess Gibbs energy of Sr respectively as functions of x_{Sr} at 988 K. The activity of Sr in Sb in the x_{Sr} = 0.03 alloy at 988 K is $a_{Sr} = 9.33\times10^{-13}$ with $\bar{G}^{E}_{Sr}$ = -197 kJ mol^{-1} indicating very strong atomic interactions, i.e. non-ideal solution behavior. Also, at mole fraction x_{Sr} = 0.84, $\bar{G}^{E}_{Sr}$ = -1 kJ mol^{-1} with an activity of a_{Sr} = 0.74; this is in line with expectation as the emf values drop to nearly zero as a result of the presence of pure Sr.

This study has determined thermodynamic properties of the binary Sr-Sb system, including activities, partial molar entropies, enthalpies, and excess Gibbs energies. The strong atomic interactions between Sr and Sb (a_{Sr} as low as 1.5×10^{-12} at 988 K and $x_{Sr} = 0.04$) indicate promise as an electrode material for separating dissolved strontium ions (Sr^{2+}) from molten salt electrolytes (e.g., LiCl-KCl-$SrCl_2$).

2.1.4 Electromotive Force Measurements on the Sr-Pb System

The use of the less-reactive Sr-Pb alloy at $x_{Sr} = 0.07$ as the RE resulted in reliable emf measurements (E_I) at 773–1073 K, demonstrated by a symmetric emf profile during cooling-heating cycles for $x_{Sr} = 0.14$ and 0.31 (Figure 18a). The potential difference between the identical RE compositions was maintained at less than ± 5 mV throughout emf measurements. In separate experiments, the RE potential (E_{II}) of the Sr-Pb alloy at $x_{Sr} = 0.07$ was determined relative to pure Sr(s) as a function of temperature over 777–1007 K (Figure 18b), resulting in a linear relationship between the emf and the temperature:

$$E_{II} = 0.676 + 9.4 \times 10^{-5} T \text{ [V] vs. pure Sr(s).} \quad (14)$$

Using the above relation, the emf values of Sr-Pb alloys (E) were reported relative to pure Sr(s). The temperature-dependent variation of emf values is displayed in Figure 19a for Sr-Pb alloys $0.07 \leq x_{Sr} \leq 0.59$, obtained during both cooling and heating cycles. The emf values decreased as the Sr mole fraction increased, and changed linearly as a function of temperature in a single-phase liquid region. Discontinuities in the slope (dE/dT) for $0.11 \leq x_{Sr} \leq 0.45$ occurred due to first-order phase transitions (i.e. liquid (L) = liquid (L) + solid (S)). However, emf values for high Sr mole fractions $x_{Sr} > 0.45$ were unstable and irreproducible between cooling and heating cycles (solid symbols in Figure 19a). Moreover, the emf values at $x_{Sr} > 0.45$ were often higher than those for lower Sr mole fractions, especially at lower temperatures (< 900 K) and thus were not considered for thermodynamic analysis. Such erratic behavior is postulated to occur as a result of (i) unstable electrical contact between the alloy WE, the electrolyte, and the electrical lead (Mo) due to high melting temperatures of these alloys and/or (ii) the formation of metastable phases during thermal cycling. The latter case is supported by the presence of metastable, non-equilibrium phases found at high Sr mole fractions despite annealing for 24 h at 15 K below solidus temperature.

For Sr-Pb alloys at $x_{Sr} = 0.07$–0.18 (Figure 19b), the temperature-dependent emf values were linear in the liquid region, and curvilinear behavior was observed for $x_{Sr} = 0.18$ in the two-phase [L + $SrPb_3$] region. In equilibrium, mole fractions $0.00 < x_{Sr} < 0.25$ would converge onto this curve in the same two-phase [L + $SrPb_3$] region, as the activity of Sr is invariant with respect to composition (Gibbs phase rule). However, the emf values of $x_{Sr} = 0.14$ below the liquidus temperature (847 K) were not reliable, possibly due to the sluggish transformation kinetics (L → L + $SrPb_3$) at low temperatures. Mole fractions $0.27 \leq x_{Sr} \leq 0.34$ exhibited a linear emf trend in the liquid region and converged onto a single linear region below ~900 K, indicating two-phase [$SrPb_3$ + Sr_3Pb_5] behavior (Figure 19c). While two-phase regions of [L + $SrPb_3$] for $x_{Sr} = 0.27$ and [L + Sr_2Pb_3] for $x_{Sr} = 0.34$ were also expected, the difference between the liquidus and solidus temperatures was too narrow (< 35–55 K) to be quantified by the emf measurements with 25 K intervals, requiring a complementary technique such as DSC.

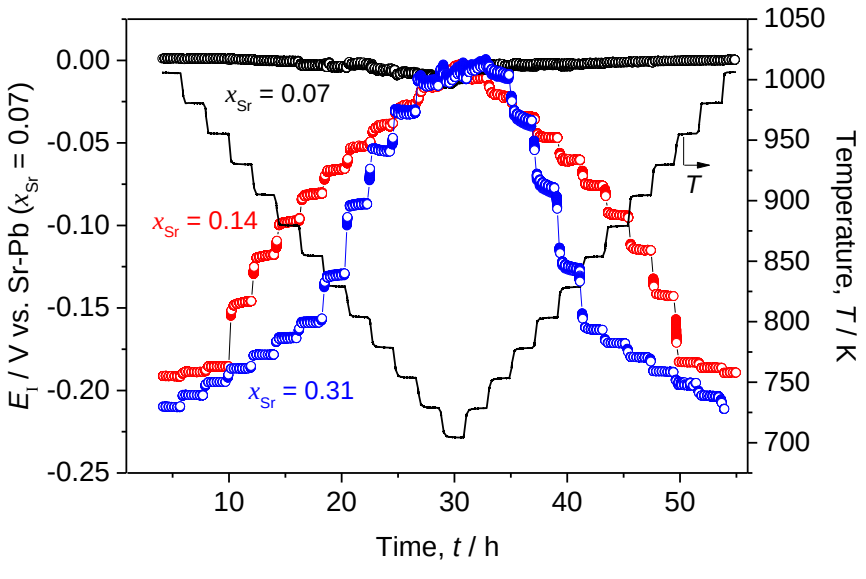

(a)

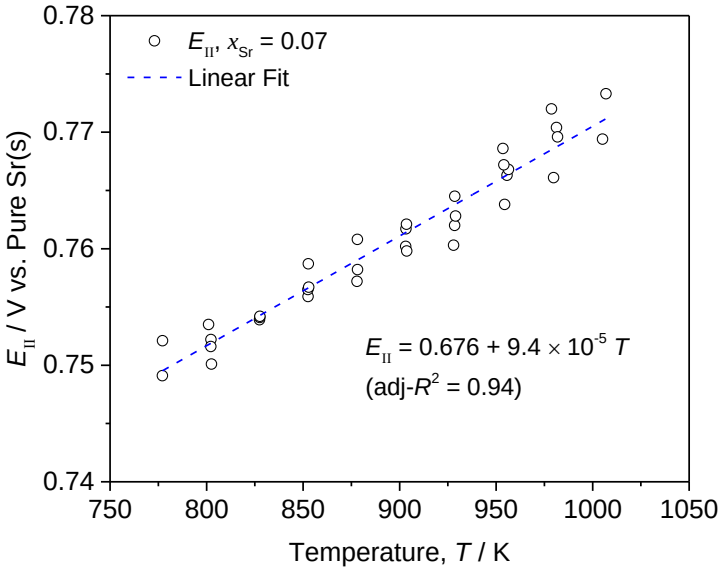

(b)

Figure 18. (a) The measured emf values (E_I) and cell temperature as a function of time during cooling and reheating of a Sr-Pb (x_{Sr} = 0.07) | CaF_2-SrF_2 | Sr(in Pb) cell with Sr-Pb alloy WEs x_{Sr} = 0.07, 0.14, and 0.31, and (b) the measured emf values (E_{II}) as a function of temperature using a Sr(s) | CaF_2-SrF_2 | Sr-Pb (x_{Sr} = 0.07) cell.

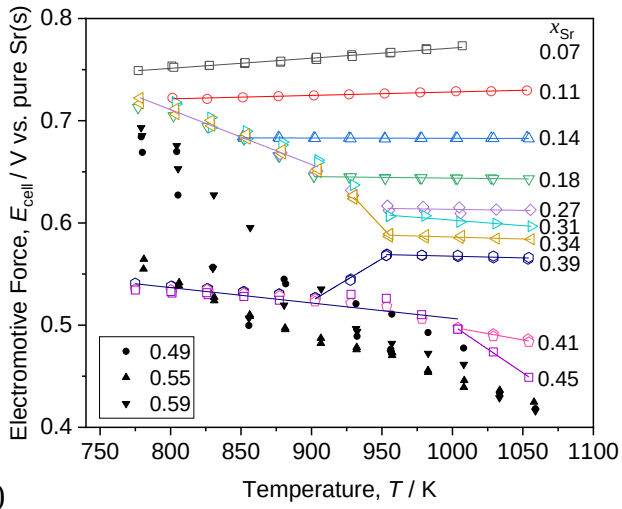

(a)

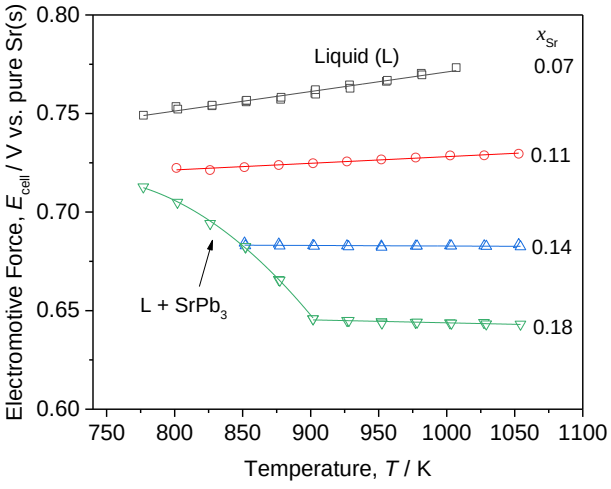

(b)

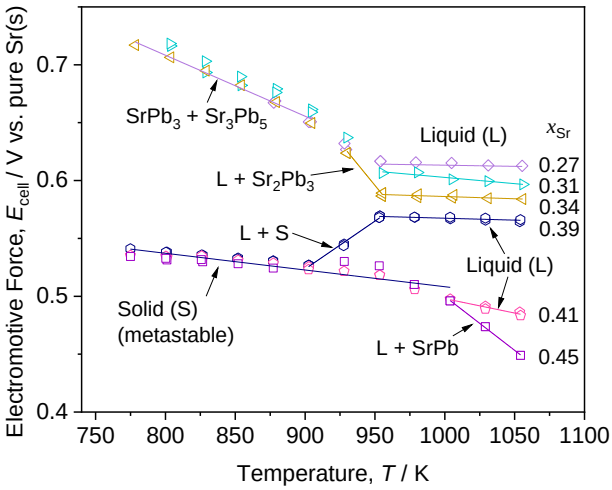

(c)

Figure 19. Electromotive force of Sr-Pb alloys as a function of temperature for (a) x_{Sr} = 0.07–0.59 (b) x_{Sr} = 0.07–0.18 and (c) x_{Sr} = 0.27–0.45, where solid lines represent linear or curvilinear fits.

Interestingly, mole fraction x_{Sr} = 0.39 exhibited two phase transitions of liquidus reaction at ~955 K and solidus reaction at ~904 K. In equilibrium, these reactions would be [L = L + Sr_2Pb_3] for liquidus and [L + Sr_2Pb_3 = Sr_3Pb_5 + Sr_2Pb_3] for solidus. However, the emf values in the [L + S] region deviated away from those in the [L + Sr_2Pb_3] region at x_{Sr} = 0.34, and the emf values below ~904 K were similar to those of x_{Sr} = 0.41 and 0.45, indicating non-equilibrium phase behavior at this composition. The deviation from equilibrium behavior could be attributed to the formation of metastable phases such as $SrPb_3$ based on the XRD analysis. Mole fraction x_{Sr} = 0.41 exhibited a limited liquid region at 1005–1054 K and its emf values converged with those of x_{Sr} = 0.45 below liquidus temperature (~1002 K) in the two-phase [L + SrPb] region.

Overall, emf measurements were reliable for mole fractions up to x_{Sr} = 0.45, in particular at elevated temperatures in the presence of a liquid phase. The linear fits of emf as a function of temperature (E_{cell} vs. T) were used to determine the change in partial molar entropy ($\Delta\bar{S}_{Sr}$), and partial molar enthalpy ($\Delta\bar{H}_{Sr}$) from the Nernst and Gibbs-Helmholtz relations at each mole fraction.

When emf values are linear with respect to temperature, $\Delta\bar{S}_{Sr}$ and $\Delta\bar{H}_{Sr}$ are independent of temperature and can be directly determined from the slope and the intercept at 0 K, respectively. The estimated partial molar quantities and linear fitting parameters (slope and intercept) are summarized in Table 6. For mole fractions x_{Sr} = 0.18 in the [L + $SrPb_3$] region (Figure 19b), temperature-dependent emf values exhibited a curved, non-linear relationship and were fit to the fitting equation used for the Ca-Sb, K-Bi, and Ba-Sb systems [23-25] with the fitting parameters reported in Table 7:

$$E = A + BT\ln(T) + CT, \quad (15)$$

where A, B, and C are fitting parameters.

The activity of Sr in Pb, a_{Sr}, and the natural log of activity, were calculated using measured emf values and the Nernst equation at 873 K, 923 K, and 973 K. The excess partial molar Gibbs energy of Sr, $\bar{G}_{Sr}^{E}$, was then calculated from the activity data. The emf values, natural log of the activity, and the excess partial molar Gibbs energy are summarized in Table 8 and presented graphically as a function of x_{Sr} in Figure 20 at 873 K.

At 873 K, the emf value decreases monotonically in the single-phase liquid region and remains constant within the two-phase regions: [$SrPb_3$ + Sr_3Pb_5] and [Sr_2Pb_3 + SrPb], due to the invariant activity within the two-phase region (Figure 20a). While the emf value in each two-phase region would decrease at higher Sr mole fractions, noticeably similar emf values between different two-phase regions were observed: (i) 0.67 V vs. pure Sr(s) for [L + $SrPb_3$] and [$SrPb_3$ + Sr_3Pb_5] across the $SrPb_3$ phase boundary and (ii) 0.53 vs. pure Sr(s) for [Sr_3Pb_5 + Sr_2Pb_3] and [Sr_2Pb_3 + SrPb] across the Sr_2Pb_3 phase boundary. While a small difference in emf values between two-phase regions is probable, the presence of metastable intermetallic phases could be an additional factor in measuring such close emf values between distinct two-phase regions. In the Sr-Pb system, large excess partial molar Gibbs energy values were observed, reaching as low as –127 kJ mol^{-1} at x_{Sr} = 0.07, indicating highly non-ideal solution behavior in liquid Sr-Pb alloys (Figure 20c).

The thermodynamic properties determined by emf technique were compared to the assessed thermodynamic properties of the binary Sr-Pb system by Zhang et al. [20] (Figure 20b-c). While the overall phase transition behavior agrees qualitatively, the activity values between the assessed thermodynamic properties and this work were different by up to three orders of magnitude in the liquid-phase region (Figure 20b). One possible reason for the large difference in activity values is the limited thermochemical data used to model the Sr-Pb system, as only phase transition temperatures were used to corroborate the CALPHAD and DFT calculations in their assessment,

leading to overestimation of interactions between Sr and Pb, in particular for the liquid-phase region.

Table 6. Change in partial molar entropy ($\Delta\bar{S}_{Sr}$), partial molar enthalpy ($\Delta\bar{H}_{Sr}$) of Sr, calculated from the linear fits of the emf versus temperature of the Sr-Pb alloys at x_{Sr} = 0.07–0.45, where $(\partial E_{cell}/\partial T)_P$ and $T^2(\partial(E_{cell}/T)/\partial T))_P$ are the slope and intercept, respectively.

x_{Sr}	T (K)	$(\partial E_{cell}/\partial T)_P$ (μV K^{-1})	$\Delta\bar{S}_{Sr}$ (J mol^{-1} K^{-1})	$T^2(\partial(E_{cell}/T)/\partial T))_P$ (mV)	$\Delta\bar{H}_{Sr}$ (kJ mol^{-1})
0.07	777–1007	94 ± 4	18.2	676 ± 4	–131
0.11	801–1053	34 ± 2	6.5	694 ± 2	–134
0.14	851–1054	–3 ± 2	–0.5	686 ± 2	–132
0.18	902–1054	–21 ± 5	–4.1	665 ± 5	–128
0.27	954–1055	–20 ± 26	–3.9	633 ± 26	–122
0.31	955–1056	–108 ± 19	–20.8	711 ± 19	–137
0.34	955–1056	–39 ± 13	–7.5	625 ± 13	–121
0.27, 0.31, 0.34	778–904	–547 ± 66	–105.6	1151 ± 57	–222
0.39	953–1054	–33 ± 8	–6.4	601 ± 8	–116
	903–953	827 ± 38	159.7	–221 ± 35	43
	775–903	–108 ± 8	–20.8	623 ± 7	–120
0.41	1005–1054	–249 ± 38	–60.6	747 ± 39	–144
0.45	1005–1054	–933 ± 31	–180.1	1433 ± 32	–277
0.41,0.45	775–1004	–136 ± 33	–26.1	644 ± 29	–124

Table 7. Non-linear fit of the temperature dependence of emf data for x_{Sr} = 0.18 in the [L + $SrPb_3$] two-phase region using $E_{cell} = A + BT\ln(T) + CT$. The standard errors in the parentheses represent the 95% confidence interval of the fit.

Two-phase region	T (K)	A	B	C
L + $SrPb_3$	777–903	–2.206 (±0.783)	–4.0 (±0.9) × 10^{-3}	3.0 (±0.7) × 10^{-2}

Table 8. Measured emf values (E_{cell}), natural log of activity of Sr, and excess partial molar Gibbs free energy ($\bar{G}^E_{Sr}$) of Sr for mole fractions x_{Sr} = 0.07–0.45 at 873 K, 923 K, and 973 K.

x_{Sr}	E_{cell} (V)			ln a_{Sr}			$\bar{G}^E_{Sr}$ (kJ mol^{-1})		
	873 K	923 K	973 K	873 K	923 K	973 K	873 K	923 K	973 K
0.07	0.759	0.763	0.768	–20.2	–19.2	–18.3	–127	–127	–127
0.11	0.724	0.726	0.727	–19.2	–18.2	–17.3	–124	–123	–122
0.14	0.683	0.683	0.683	–18.2	–17.2	–16.3	–118	–117	–116
0.18	0.673	0.646	0.645	–17.9	–16.2	–15.4	–120	–115	–114
0.27	0.673	0.635	0.614	–17.9	–16.0	–14.6	–121	–114	–109
0.31	0.673	0.635	0.606	–17.9	–16.0	–14.4	–122	–114	–108
0.34	0.673	0.635	0.587	–17.9	–16.0	–14.0	–123	–115	–106
0.39	0.530	0.501	0.572	–14.1	–12.6	–13.6	–96	–90	–103
0.41	0.525	0.519	0.512	–14.0	–13.0	–12.2	–95	–93	–92
0.45	0.525	0.519	0.512	–14.0	–13.0	–12.2	–96	–94	–92

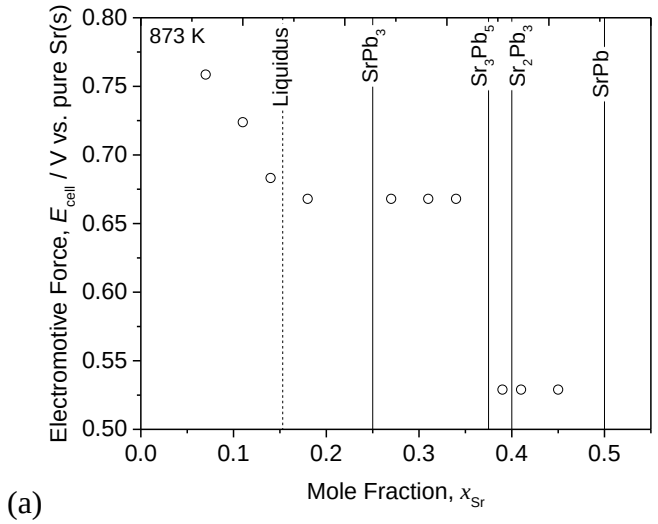

(a)

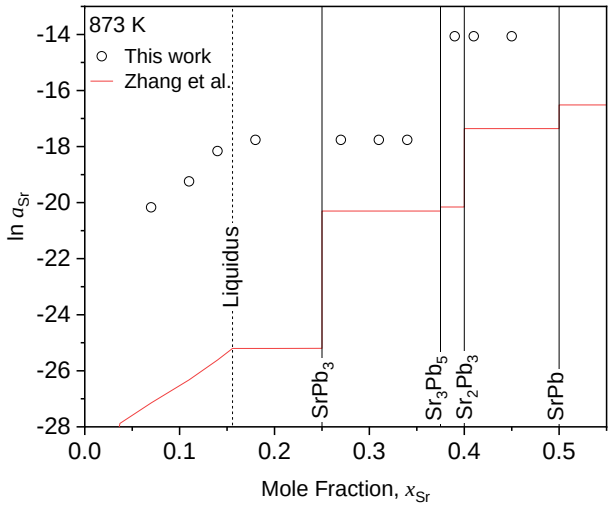

(b)

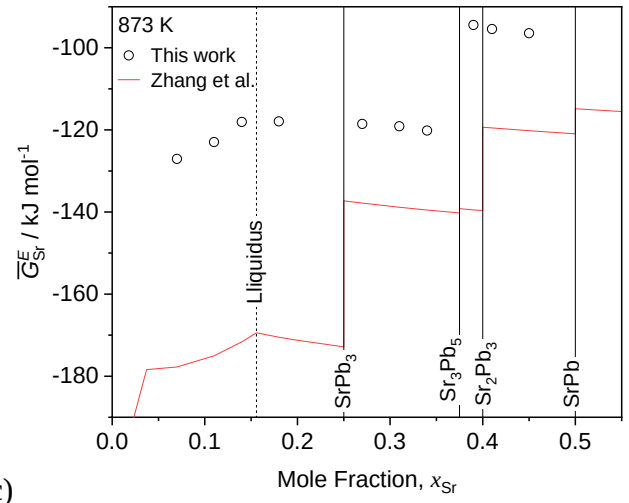

(c)

Figure 20. Plots of the (a) measured emf values, (b) the natural log of the activity of Sr, and (c) the excess partial molar Gibbs free energy of Sr as a function of mole fraction of Sr at 873 K, compared to the work by Zhang et al. [20]. The liquidus composition was obtained from their assessed phase diagram.

2.1.5 Electromotive Force Measurements on the Ba-Bi System

Figure 21a displays the measured emf values, E_I, of Ba-Bi alloys (x_{Ba} = 0.05, 0.10, 0.20) and cell temperature as a function of time, using a Ba-Bi(x_{Ba} = 0.05)|CaF_2-BaF_2|Ba(in Bi) cell. The potential difference between the two identical Ba-Bi alloys at x_{Ba} = 0.05 was less than 2 mV during the entire measurement. Moreover, a symmetric emf profile during the heating and cooling cycles indicates that the emf measurements were reproducible, in particular at low Ba compositions. In general, the use of the less reactive Ba-Bi alloy RE enabled highly reproducible emf measurements (E_I) of Ba-Bi alloys over a wide range of mole fractions x_{Ba} = 0.10–0.80 at 723–1073 K.

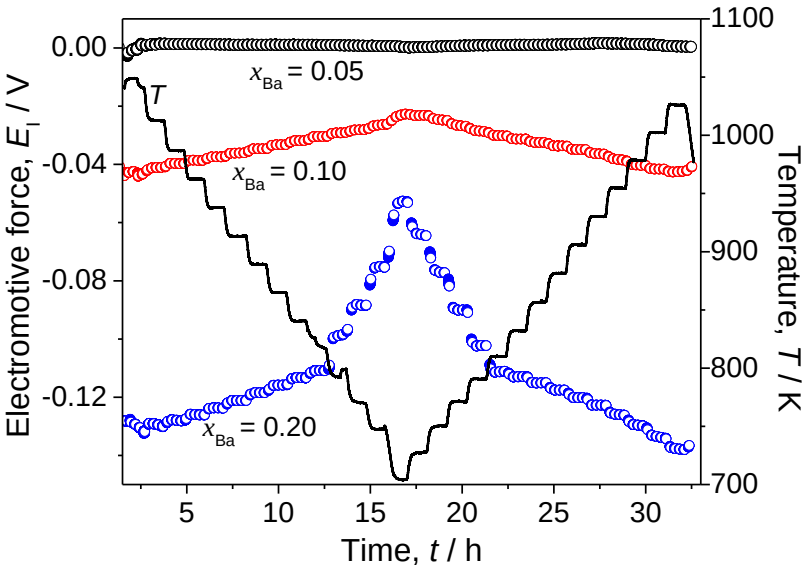

(a)

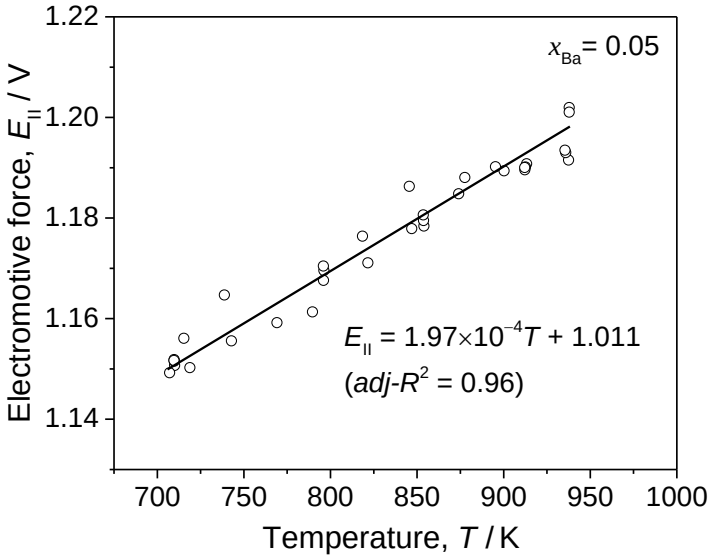

(b)

Figure 21. (a) The measured emf values (E_I) and temperature as a function of time upon cooling and reheating a Ba-Bi(x_{Ba} = 0.05)|CaF_2-BaF_2|Ba(in Bi) cell with Ba-Bi alloys x_{Ba} = 0.05, 0.10, and 0.20 and (b) the measured emf values (E_{II}) using a Ba(s)|CaF_2-BaF_2(s)|Ba-Bi(x_{Ba} = 0.05) cell.

In separate experiments, a Ba(s)|CaF_2-BaF_2|Ba-Bi(x_{Ba} = 0.05) cell was employed to determine the emf values of Ba-Bi alloy at x_{Ba} = 0.05 relative to pure barium, E_{II} (
Figure 21b). The emf values were linear as a function of temperature according to:

$$E_{II} = 1.97\times10^{-4}\,T + 1.011\ [\text{V}]. \qquad (16)$$

Using the linear equation (Eq. 16), emf values of Ba-Bi alloys (E) were reported against pure barium according to: E (= E_I + E_{II}).

Figure 22 displays the variation of emf values with respect to temperature for Ba-Bi alloys x_{Ba} = 0.05–0.80. In Figure 22a, above the liquidus [liquid = liquid + $BaBi_3$], the emf increases linearly as temperature increases, and decreases monotonically as x_{Ba} increases. Below the liquidus, for Ba-Bi alloys up to x_{Ba} = 0.25, emf values converge onto a single line because the activity of barium is invariant with composition in this two-phase region [liquid + $BaBi_3$]. Mole fraction x_{Ba} = 0.30 exhibited a liquidus [liquid = liquid + $BaBi_3$] transition at ~874 K and is expected to undergo solidus transition [liquid + $BaBi_3$ = $BaBi_3$ + $Ba_{11}Bi_{10}$] based on our revised phase diagram; however, the emf values exhibited a discontinuity at ~812–836 K and collapsed onto the line defined as liquid + $BaBi_3$, possibly due to the formation of non-equilibrium Bi phase during the solidification.

In Figure 22b, x_{Ba} = 0.40 exhibited two transition temperatures of liquidus [liquid = liquid + $Ba_{11}Bi_{10}$] at ~ 910 K and solidus [liquid + $Ba_{11}Bi_{10}$ = $Ba_{11}Bi_{10}$ + $BaBi_3$] at ~ 837 K. Interestingly, mole fraction x_{Ba} = 0.35 exhibited a direct eutectic transition [liquid = $Ba_{11}Bi_{10}$ + $BaBi_3$] at ~843 K. Below this solidus (or eutectic) transition temperature, emf values of these two compositions converged together within 10 mV difference. Mole fractions x_{Ba} = 0.45–0.55 exhibited increased hysteresis during a cooling-heating cycle, up to 20 mV difference, possibly due to the increased reactivity at high Ba concentrations and/or unstable physical contact between the solid-state alloy WE and the electrolyte. In the composition range of x_{Ba} = 0.45–0.55, emf values during heating cycles exhibited a reproducible linear behavior and were therefore included in the analysis. As expected, a rapid drop in emf values was observed at high Ba mole fractions x_{Ba} = 0.75–0.80 (Figure 222c) as the alloy composition approached pure Ba (a_{Ba} = 1).

From the linear fits of the data presented in Figure 22, the changes in partial molar entropy ($\Delta\overline{S}_{Ba}$) and enthalpy ($\Delta\overline{H}_{Ba}$) of Ba in Bi were calculated, and the results are summarized in Table 9. The changes in partial molar entropy and enthalpy were assumed independent of temperature over the fitted range.

The activity of Ba was determined using the emf values and the Nernst equation at 773 K, 873 K, and 973 K. The excess partial molar Gibbs free energy $\overline{G}_{Ba}^{E}$ was also obtained. The emf values, natural log of the activity, and the excess partial molar Gibbs free energy are summarized in Table 10 at each temperature. Figure 23 displays these thermodynamic properties as a function of mole fraction at 773 K, including the liquidus composition estimated by emf measurements.

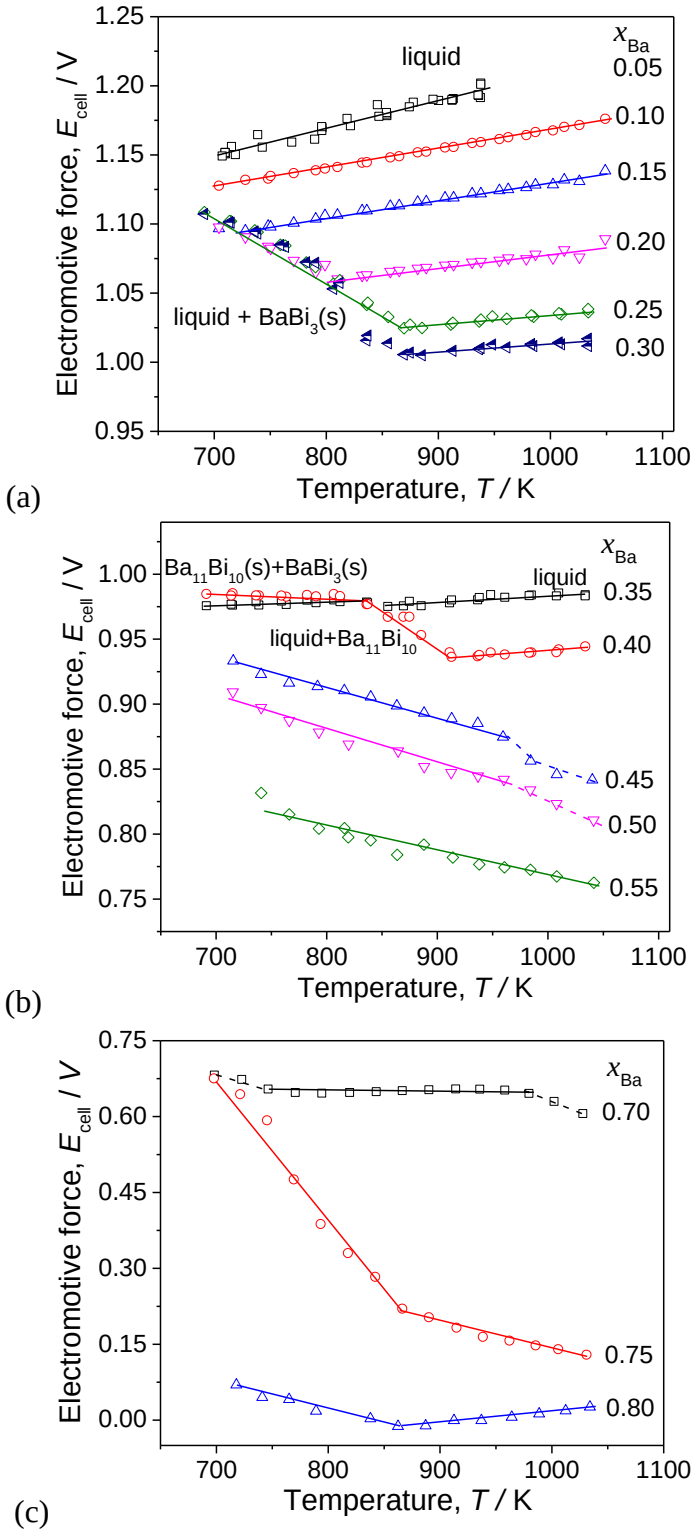

Figure 22. The emf of Ba-Bi alloys vs. pure Ba(s) as a function of temperature for (a) x_{Ba} = 0.05 to 0.30, (b) x_{Ba} = 0.35 to 0.55 and (c) x_{Ba} = 0.70 to 0.80, where solid lines represent linear fits and dashed lines are a visual guide.

Table 9. Change in partial molar entropy and enthalpy of barium calculated from linear fits to the emf data versus temperature for $x_{Ba} = 0.05–0.80$, where the slopes and intercepts are $\partial E_{cell}/\partial T$ and $T^2(\partial(E_{cell}/T)/\partial T)$, respectively. The *adj-R*^{2} value for each linear fit is reported.

x_{Ba}	T (K)	$\partial E_{cell}/\partial T$ (μV K^{-1})	$T^2(\partial(E_{cell}/T)/\partial T)$ (mV)	$\Delta\bar{S}_{Ba}$ (J mol^{-1} K^{-1})	$\Delta\bar{H}_{Ba}$ (kJ mol^{-1})	*adj-R*^{2}
0.05	707-938	197±6	1011±5	38.0	-195.1	0.96
0.10	704-1048	137±1	1031±1	26.4	-199.0	0.99
0.15	728-1048	125±2	1005±2	24.1	-193.9	0.99
0.20	809-1048	94±7	984±6	18.1	-189.9	0.90
0.25	881-1048	73.4±5	961±5	14.2	-185.4	0.93
	704-881	-480±14	1448±13	-92.6	-279.4	0.98
0.30	864-1048	54.7±7	958±7	105.6	-184.8	0.80
	704-864	-614±43	1545±34	-118.5	-298.1	0.93
0.35	875-1033	51.8±7	932±6	10.0	-179.8	0.80
	691-875	19.8±1	961±6	3.8	-185.4	0.85
0.40	913-1033	44.6±11	896±10	8.6	-172.9	0.81
	812-913	-501±71	1398±61	-96.7	-270.0	0.91
	691-812	-29.4±7	1006±8	-5.7	-194.1	0.84
0.45	715-961	-215±9	1085±7	-41.5	-209.4	0.98
0.50	715-961	-271±17	1097±14	-52.3	-211.7	0.97
0.55	740-1041	-201±17	967±15	-38.8	-186.6	0.92
0.70	770-957	6.9±0.6	645±12	1.3	-124.5	0.84
0.75	866-1030	-542±40	683±38	-104.6	-131.8	0.96
	697-866	-2900±155	2716±121	-559.6	-524.1	0.98
0.80	862-1034	222±15	-206±14	42.8	-39.8	0.97
	717-862	-530±49	444±38	-102.3	-85.7	0.96

Table 10. Measured emf values, the natural log of activity of Ba, and the excess partial molar Gibbs free energy of Ba-Bi alloys over x_{Ba} = 0.05–0.80 at 773 K, 873 K, and 973K.

x_{Ba}	E (V)			ln a_{Ba}			$\overline{G}^{E}_{Ba}$ (kJ mol^{-1})		
	773 K	873 K	973 K	773 K	873 K	973 K	773 K	873 K	973 K
0.05	1.164	1.183	1.203	-35.0	-31.5	-28.7	-205	-206	-208
0.10	1.137	1.150	1.164	-34.1	-30.6	-27.8	-205	-205	-206
0.15	1.101	1.114	1.127	-33.0	-29.6	-26.9	-200	-201	-202
0.20	1.075	1.066	1.076	-32.2	-28.3	-25.7	-197	-194	-194
0.25	1.075	1.027	1.032	-32.2	-27.3	-24.6	-198	-188	-188
0.30	1.069	1.006	1.011	-32.0	-26.7	-24.1	-198	-185	-185
0.35	0.986	0.980	0.982	-29.6	-26.1	-23.4	-184	-181	-181
0.40	0.986	0.960	0.939	-29.6	-25.5	-22.4	-184	-178	-173
0.45	0.924	0.899	0.861	-27.7	-23.9	-20.5	-173	-167	-159
0.50	0.877	0.855	0.847	-26.3	-22.7	-20.2	-164	-160	-157
0.55	0.816	0.795	0.773	-24.5	-21.1	-18.4	-154	-149	-144
0.70	0.647	0.651	0.648	-19.4	-17.3	-15.5	-122	-123	-122
0.75	0.474	0.209	0.155	-14.2	-5.6	-3.7	-90	-38	-27
0.80	0.034	0.000	0.010	-1.02	0.0	-0.24	-5	1	0

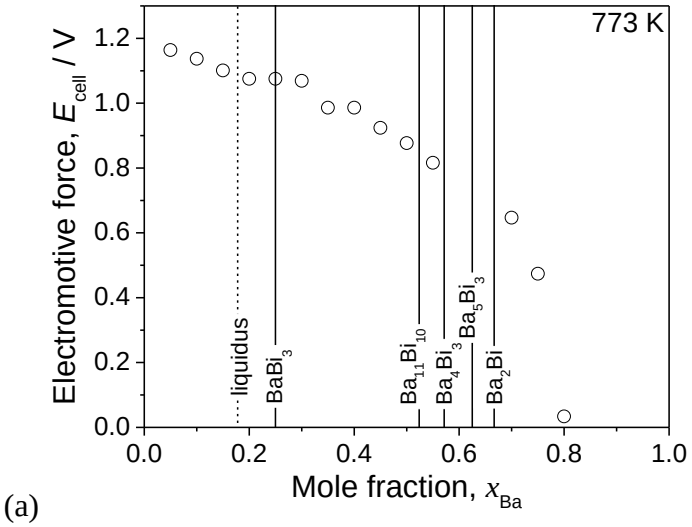

(a)

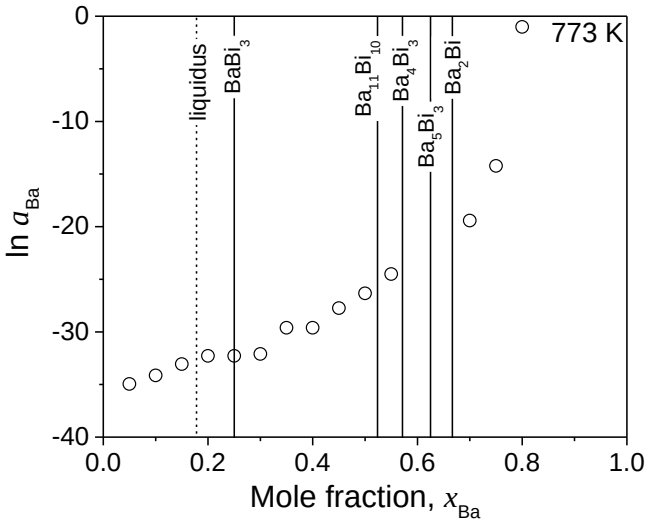

(b)

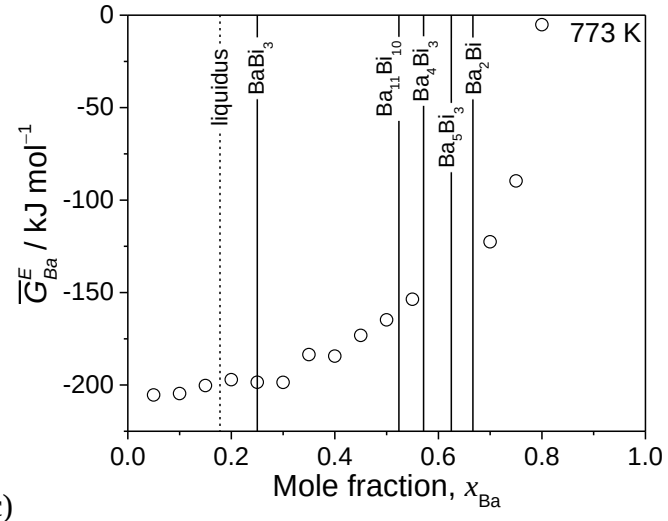

(c)

Figure 23. Plots of the (a) measured emf values (*E*), (b) the natural log of the activity of Ba (ln a_{Ba}), and (c) the calculated excess partial molar Gibbs free energy of Ba as a function of mole fraction at 773 K.

Based on equilibrium thermodynamics at a given temperature, the emf values will decrease in the single-phase region as x_{Ba} increases and remain constant in the two-phase regions, according to the Gibbs phase rule. This equilibrium behavior was well observed at x_{Ba} = 0.05–0.25, as can be seen in Figure 23a where the emf values monotonically decreases as x_{Ba} increases in the liquid phase ($x_{Ba} \leq 0.18$) at 773K. In the two-phase [liquid + $BaBi_3$] region ($0.18 < x_{Ba} < 0.25$), the emf values were nearly constant at 1.08 V, and thus the activity values (Figure 23b). At low Ba mole fractions, a large excess partial molar Gibbs free energy was observed, as low as –205 kJ mol^{-1}, due to strong chemical interactions between Ba and Bi (Figure 23c). However, in the two-phase regions [$BaBi_3$ + $Ba_{11}Bi_{10}$] and [Ba_2Bi + Ba], the emf values continued to decrease as x_{Ba} increased (Figure 23a), deviating from equilibrium phase behavior. Such a deviation was found to originate from the presence of non-equilibrium phases within these composition ranges.

Using the linear fits of emf values in the liquid phase, the emf values of selected mole fractions x_{Ba} = 0.05–0.20 were extrapolated at 1123 K and compared to the results by Delcet *et al*. (Tabl2 11). In general, the difference in emf values at each composition were within 30–70 mV, however, the emf values from this study were consistently lower compared to the values obtained by Delcet *et al* [21]. The difference can be attributed to, in part, the uncertainty in compositional accounting of Ba in their coulombic titration due to increased electronic conductivity at elevated temperatures.

Table 11. The estimated emf, partial molar Gibbs free energy, and activity values of Ba in Bi at 1123 K based on the extrapolation of the linear fit, compared to the results by Delcet *et al*. [3].

x_{Ba}	This study			Delcet *et al*.		
	E_{cell} (V)	$\Delta\overline{G}_{Ba}$ (kJ mol^{-1})	a_{Ba}	E_{cell} (V)	$\Delta\overline{G}_{Ba}$ (kJ mol^{-1})	a_{Ba}
0.05	1.23	-237.8	8.7×10^{-12}	1.30	-250.0	2.4×10^{-12}
0.10	1.18	-228.6	2.3×10^{-11}	1.24	-238.9	7.7×10^{-12}
0.15	1.15	-221.0	5.3×10^{-11}	1.18	-227.9	2.5×10^{-11}
0.20	1.09	-210.3	1.7×10^{-10}	1.12	-215.6	9.4×10^{-11}

2.1.6 Electromotive Force Measurements on the Ba-Sb System

The electromotive force (emf) values were measured for Ba-Sb alloys x_{Ba} = 0.03-0.77 using the electrochemical cell described in the **Error! Reference source not found.**. During the thermal cycles of the electrochemical cell, the emf values exhibited a hysteresis between heating and cooling cycles, as shown in Figure 24a for x_{Ba} = 0.03 and x_{Ba} = 0.09. This hysteresis originated from the undercooling of the alloys, during which the alloys maintain their high temperature phase below its equilibrium transition temperature. The effect of undercooling can also be explicitly observed from the DSC scans of these alloys where the detected transition temperatures were substantially lower during the cooling than during the heating (Figure 24b). For this reason, the emf measurements for Ba-Sb alloys are reported using only the heating cycle.

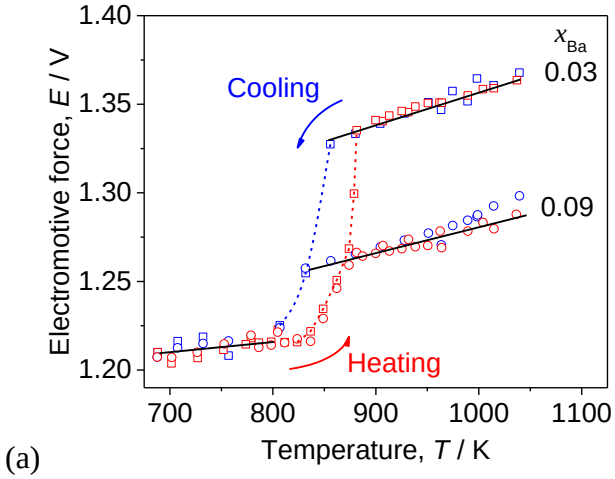

(a)

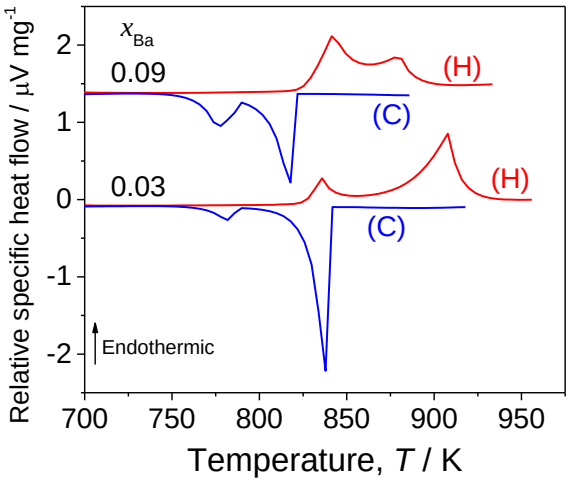

(b)

Figure 24. (a) The emf trace of Ba-Sb alloys as a function of temperature showing a hysteresis between heating (red color) and cooling (blue color) cycles for x_{Ba} = 0.03 and 0.09, arrows indicate the direction of the heating and cooling cycles, and (b) the DSC scans for 0.03 and 0.09 at 20 K min^{-1} heating rate, where (H) and (C) indicate heating and cooling curves, respectively.

Figure 25 displays the variation of emf with temperature for various Ba-Sb mole fractions x_{Ba} = 0.03-0.77. Discontinuities in slope are apparent and indicate first-order phase transitions. For mole fractions x_{Ba} = 0.03-0.25, above the liquidus [liquid = liquid + $BaSb_3$], emf varies linearly with temperature and decreases monotonically as x_{Ba} increases (Figure 25a). Below the solidus [liquid + Sb = $BaSb_3$ + Sb], all the emf values fall onto a single line as barium activity is invariant with respect to composition within the [$BaSb_3$ + Sb] two-phase region. In contrast, the emf trace with temperature exhibits curvature in the [liquid + Sb] two-phase region (Figure 25a).

Mole fraction x_{Ba} = 0.30 exhibited two transition temperatures of liquidus [liquid = liquid + Ba_2Sb_3] at ~955 K and solidus [liquid + Ba_2Sb_3 = $BaSb_3$ + $BaSb_2$] at ~864 K; mole fraction x_{Ba} = 0.40 exhibited a solidus transition [liquid + Ba_2Sb_3 = $BaSb_2$ + Ba_2Sb_3] at ~ 884 K (Figure 25b). The transition reactions at mole fractions x_{Ba} = 0.30 and x_{Ba} = 0.40 were speculated based on XRD analysis and a similar emf trace found at intermediate temperatures, which indicates identical two-phase [liquid + Ba_2Sb_3] behavior at these compositions. As expected from the same equilibrium

phase constituents of [$BaSb_2$ + Ba_2Sb_3] for mole fractions x_{Ba} = 0.35 and x_{Ba} = 0.40, a similar emf trace was observed for both compositions above 884 K; however, the emf trace of x_{Ba} = 0.35 diverged from the trace of x_{Ba} = 0.40 and merged onto the trace of x_{Ba} = 0.30 below 884 K. Such a deviation at x_{Ba} = 0.35 is thought to originate from the formation of metastable phases [$BaSb_3$ + $BaSb_2$] instead of equilibrium phases of [$BaSb_2$ + Ba_2Sb_3] during the thermal cycles.

At x_{Ba} > 0.67, two-phase [Ba_2Sb + Ba] equilibrium is expected and thus, the emf will approach zero due to the presence of the pure Ba phase. This equilibrium behavior was observed for x_{Ba} = 0.77 (Figure 25c) in accordance with its primary phase constituents of Ba_2Sb and Ba. However, mole fraction x_{Ba} = 0.71 had emf values as high as 1.1 V at low temperatures and followed a similar emf trace with x_{Ba} = 0.66 below 924 K (Figure 25c). Such high emf values at x_{Ba} = 0.71 come from the formation of metastable [Ba_2Sb + Ba_5Sb_3] phases which were identified both at x_{Ba} = 0.66 and x_{Ba} = 0.71 by XRD.

In general, the emf measurements for high mole fraction barium alloys (x_{Ba} > 0.30) were less reliable compared to low barium mole fractions due to the formation of metastable phases, increased reactivity, and high melting temperatures (> 1073 K) that may prevent stable electrical contacts among the cell components. For example, emf values as high as 1.21 V were observed at mole fraction x_{Ba} = 0.51 at 728 K, higher than those of low barium mole fractions x_{Ba} = 0.03-0.40 (Figure 25b-c).

The emf traces as a function of temperature can be used to determine the change in partial molar entropy $\Delta\bar{S}_{Ba}$ and partial molar enthalpy $\Delta\bar{H}_{Ba}$ from the Nernst and Gibbs-Helmholtz relations. When the temperature dependence of emf values is linear, $\Delta\bar{S}_{Ba}$ and $\Delta\bar{H}_{Ba}$ are independent of temperature and can be directly determined from the slope and intercept at 0 K, respectively. The estimated partial molar quantities as well as the linear fits of emf values are summarized in Table 12. For mole fractions x_{Ba} = 0.03-0.14, the emf trace exhibited curved, non-linear behavior in the two-phase region of [liquid + Sb], and was fit to the aforementioned fitting equation. The curve fit for the two-phase region of [liquid + Sb] is shown in Figure 25a and the fitting parameters are reported in Table 13.

The activity of Ba was calculated using the measured emf values and the Nernst equation ($\ln a_{Ba} = -2FE/RT$) at 873 K, 923 K, and 973 K, summarized in Table 14. The excess partial molar Gibbs free energy, $\bar{G}^{E}_{Ba}$ was calculated in the same manner as in **Error! Reference source not found.**. At 923 K, the emf, natural log of activity, and excess partial molar Gibbs free energy of barium are graphically presented as a function of mole fraction in Figure 26. The equilibrium phase behavior is clearly visible in the [liquid + Ba_2Sb_3] two-phase region where emf values remain constant at 1.12 V due to the invariant activity in this composition range. In contrast, emf values at x_{Ba} = 0.71 and x_{Ba} = 0.77 are different by ~0.8 V due to the formation of metastable phases of [Ba_5Sb_3 + Ba_2Sb] at x_{Ba} = 0.71, as previously discussed.

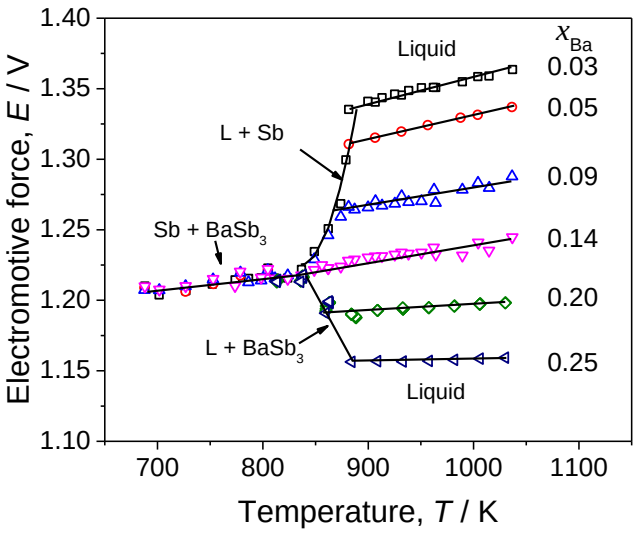

(a)

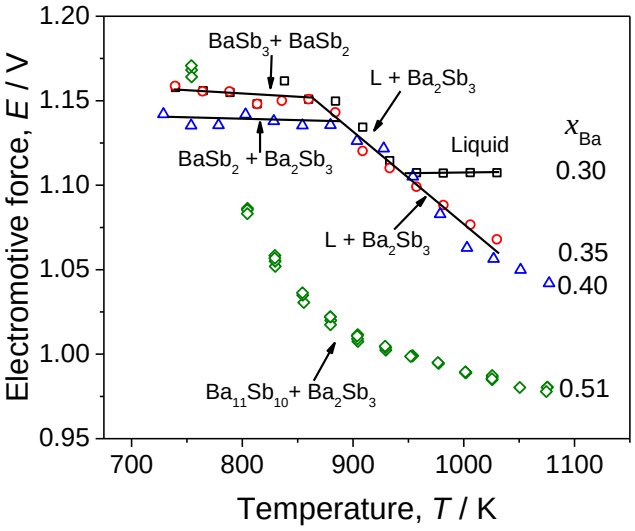

(b)

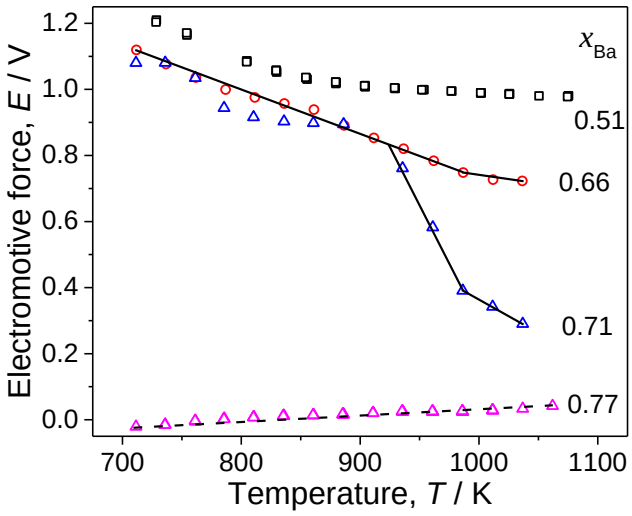

(c)

Figure 25. The emf as a function of temperature for Ba-Sb alloys (a) x_{Ba} = 0.03–0.25 (b) x_{Ba} = 0.30–0.51 and (c) x_{Ba} = 0.51–0.77.

Table 12. Change in partial molar entropy, $\Delta\overline{\boldsymbol{S}}_{\mathbf{Ba}}$, and partial molar enthalpy, $\Delta\overline{\boldsymbol{H}}_{\mathbf{Ba}}$, of barium calculated from the linear fits of the emf versus temperature data of the Ba-Sb alloys at x_{Ba} = 0.03-0.71, where $(\boldsymbol{\partial E/\partial T})_P$ and $\boldsymbol{T^2(\partial(E/T)/\partial T))_P}$ are the slope and intercepts, respectively.

x_{Ba}	T (K)	$(\boldsymbol{\partial E/\partial T})_P$ (μV K^{-1})	$\Delta\overline{S}_{Ba}$ (J mol^{-1} K^{-1})	$\boldsymbol{T^2(\partial(E/T)/\partial T))_P}$ (mV)	$\Delta\overline{H}_{Ba}$ (kJ mol^{-1})	*adj-*R^2
0.03	888-1036	161±8	31.1	1196±8	-231	0.97
	698-836	75±18	14.5	1156±14	-223	0.80
0.05	876-1036	170±3	32.8	1162±3	-224	0.99
0.09	863-1036	136±16	26.2	1144±15	-221	0.83
0.14	831-1036	104±10	20.1	1135±9	-219	0.84
0.20	863-1030	47±2	9.1	1150±2	-221	0.96
0.25	884-1030	21±2	4.1	1137±2	-219	0.81
	835-884	-1120±96	-216	2151±83	-415	0.89
0.30	957-1030	6.4±2	1.2	1101±2	-212	0.82
0.30/0.35	736-862	-75.9±25	-14.6	1213±19	-234	0.64
0.35/0.40	884-1055	-503±19	-97.1	1584±18	-305	0.94
0.40	739-884	-23.9±22	-4.6	1156±18	-223	0.60
0.66	986-1036	-601±78	-116	1340±80	-259	0.86
	711-986	-1280±22	-247	2019±20	-390	0.99
0.71	986-1036	-1980±35	-382	2348±40	-453	0.99
	935-986	-7320±180	-1412	7612±17	-1469	0.99

Table 13. Non-linear fit of the temperature dependence of emf data in two-phase region. The [liquid + Sb] data were fit to $\boldsymbol{E = A + BT\,ln(T) + CT}$. Range of values given represent the 95% confidence interval of the fit.

two-phase region	T (K)	A	B	C
liquid + Sb	830-889	59.2±46.6	6.9±5.4 × 10^{-2}	-0.54±0.42

Table 14. Measured emf values, natural logarithm of activity of Ba in Sb, and the excess partial molar Gibbs free energy of Ba over x_{Ba} = 0.03-0.71 at 873 K, 923 K, and 973 K.

x_{Ba}	E (V)			ln a_{Ba}			$\overline{G}^{E}_{Ba}$ (kJ mol^{-1})		
	873 K	923 K	973 K	873 K	923 K	973 K	873 K	923 K	973 K
0.03	1.279	1.346	1.353	-34.0	-33.8	-32.3	-221	-233	-233
0.05	1.279	1.319	1.327	-34.0	-33.2	-31.7	-225	-232	-232
0.09	1.263	1.270	1.276	-33.6	-31.9	-30.4	-226	-227	-227
0.14	1.226	1.231	1.236	-32.6	-31.0	-29.5	-222	-222	-223
0.20	1.191	1.193	1.196	-31.7	-30.0	-28.5	-218	-218	-218
0.25	1.173	1.156	1.157	-31.2	-29.1	-27.6	-216	-213	-212
0.30	1.147	1.120	1.111	-30.5	-28.2	-26.4	-213	-207	-204
0.35	1.147	1.120	1.095	-30.5	-28.2	-26.1	-214	-208	-203
0.40	1.135	1.120	1.095	-30.2	-28.2	-26.1	-212	-209	-203
0.51	1.019	1.003	0.991	-27.1	-25.2	-23.6	-191	-188	-186
0.66	0.902	0.838	0.774	-24.0	-21.1	-18.5	-171	-158	-146
0.71	0.902	0.838	0.490	-24.0	-21.1	-11.7	-171	-159	-92

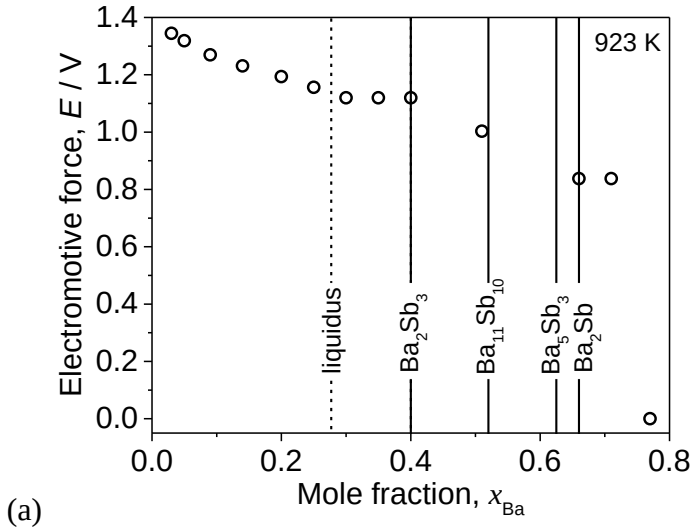

(a)

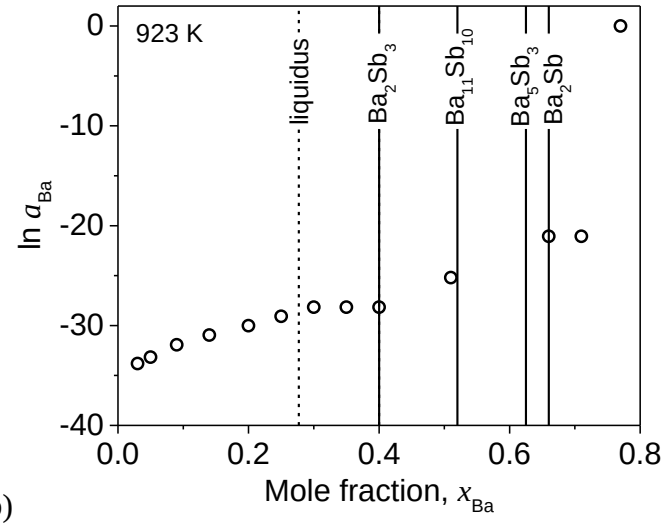

(b)

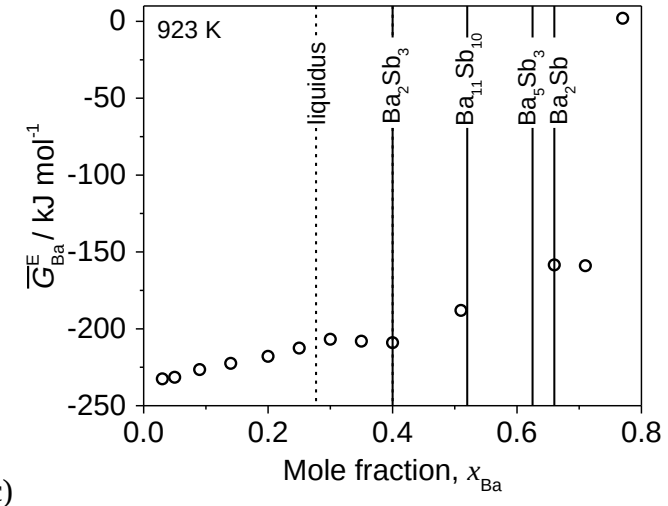

(c)

Figure 26. Plots of the (a) measured emf values, (b) the natural log of the activity of Ba, and (c) the calculated excess partial molar Gibbs free energy of Ba as a function of mole fraction at 923 K.

Delcet *et al*. reported the partial molar Gibbs free energies $\bar{G}_{\mathrm{Ba}}$ at 1073 K, above the melting temperature of pure barium ($T_{\mathrm{m,\ Ba}}$ = 1000 K), using the coulometric titration technique [21]. To compare their results with this study, the linear fits of emf values (Table 12) were extrapolated to 1073 K. Since the emf values in this study were reported with respect to Ba(s), the linear slopes of emf values ($= \Delta\bar{S}_{\mathrm{Ba}}/2F$) were adjusted to consider the phase change of the pure barium metal above its melting temperature (1000 K) by subtracting $\Delta S_{f,\mathrm{Ba}}/2F$, where $\Delta S_{f,\mathrm{Ba}}$ is the entropy of fusion of pure barium, 7.12 J mol^{-1} K^{-1} ($= \Delta H_{f,\mathrm{Ba}}/T_{m,\mathrm{Ba}}$) [23].

Based on the extrapolated emf values with respect to Ba(l) at 1073 K, the partial molar free energies were calculated up to x_{Ba} = 0.40 and compared to the results by Delcet *et al*. (Figure 27). While the partial molar free energies agree well with each other within a 6-13 kJ mol^{-1} difference, a distinct phase behavior is evident between two studies. At 1073 K, this work estimates the liquidus composition at x_{Ba} = ~0.35 and the presence of Ba_2Sb_3; however, Delcet *et al*. reported the liquidus at x_{Ba} = ~0.27, the presence of $BaSb_2$, and neglected the presence of Ba_2Sb_3. Considering the emf traces of various mole fractions in Figure 25, the liquidus composition is expected to be more than 30 mol% Ba and the presence of $BaSb_2$ was only evident at temperatures below 864 K. As indicated by Delcet et al., the uncertainty in composition accounting (up to 3 mol% Ba) might have caused inaccuracies in determining the phase boundaries of Ba-Sb system [21].

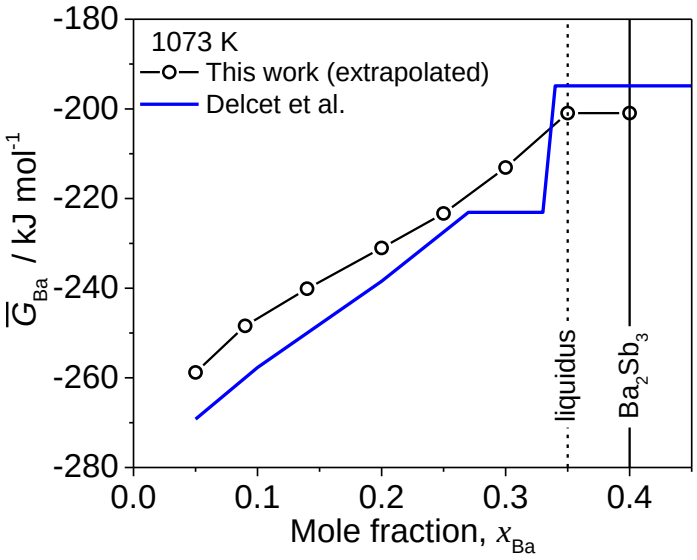

Figure 27. The partial molar Gibbs free energy of Ba in Sb at 1073 K, compared to the work by Delcet *et al*. [10]. The partial molar Gibbs free energy values were estimated by extrapolating the measured emf values at 1073 K relative to pure liquid Ba(l).

2.2 Thermodynamic Modeling of Alloys

Computational approaches to investigating and refining phase diagrams rely heavily on experimentally generated thermodynamic data in order to inform models. Studies often employ a hybrid approach, using first-principles calculations based on density functional theory (DFT) to assess the stability of viable intermetallic compounds and then incorporating these calculations into the CALculation of Phase Diagrams (CALPHAD) technique. Due to the quantity and quality of the fundamental thermodynamic data generated for the Sr-Bi, Sr-Sb, Sr-Pb, Ba-Bi, and Ba-Sb systems, computational modeling was the next logical step for improving understanding of the AE-M systems as well as ternary/quaternary systems involving multiple alkaline-earths or liquid metals, which could potentially yield improved behavior.

2.2.1 Thermodynamic Modeling of the Sr-Sb System

The lack of a computational description for the Sr-Sb system as well the drastic changes proposed, i.e. the removal of the $SrSb_3$, SrSb, and Sr_3Sb_2 phases and the addition of the $SrSb_2$, Sr_2Sb_3, $Sr_{11}Sb_{10}$, $Sr_{16}Sb_{11}$, and Sr_5Sb_3 phases, necessitated further investigation of the system to confirm the predicted changes. As such, a computational approach using a combination of first-principles calculations and the CALPHAD technique was applied to the Sr-Sb system in order to complete understanding of the Sr-Sb phase behavior [24]. The phase behavior of the Sr-Sb system predicted using X-ray diffraction (XRD) was corroborated with first-principles DFT-based calculations, which were used to confirm the stability of all phases noted by XRD ($SrSb_2$, Sr_2Sb_3, $Sr_{11}Sb_{10}$, $Sr_{16}Sb_{11}$, and Sr_5Sb_3) as well as to confirm the instability of several phases suggested in previously published phase diagrams (SrSb, $SrSb_3$, and Sr_3Sb_2). To corroborate the experimental XRD results, first-principles calculations were performed to determine the theoretical stability of all the phases present in the Sr-Sb system, both those observed via the aforementioned XRD as well as those predicted in previous phase diagrams. DFT-based first-principles calculations were completed on eight intermetallic compounds i.e. system: $SrSb_2$, Sr_2Sb_3, $Sr_{11}Sb_{10}$, Sr_2Sb, Sr_3Sb_2, $Sr_{16}Sb_{11}$, and two crystal structures (hex and ortho) for the Sr_5Sb_3 intermetallic. The Vienna Ab-initio Simulation Package (VASP) was used to perform the first-principles calculations [25]. The lowest energy structures were obtained from the Materials Project for all the intermetallics [26–35], except $Sr_{16}Sb_{11}$ [36]. The relaxed structures were deformed into 5 different volumes in order to complete an equation of state (EOS) fitting of the energy vs. volume (*E*-*V*) curve. A four-parameter Birch-Murnaghan EOS equation was used based on the suggestion by Shang et al. [37]:

$$E_0(V) = a + bV^{-2/3} + cV^{-4/3} + \mathrm{d}V^{-2} \tag{17}$$

, where *a*, *b*, *c* and *d* are fitting parameters. From the EOS fitting, the equilibrium properties at 0 K without the contribution of zero-point vibration energy, including equilibrium volume (*V*), energy (*E*), bulk modulus (*B*), and the first derivative of bulk modulus with respect to pressure (*B'*) were calculated. The finite temperature properties were approximated with the Neumann-Kopp approach. The projector augmented-wave (PAW) method [38,39] was used to describe the electron-ion interactions with the exchange correlation functional elucidated by the generalized gradient approximation (GGA) implemented by Perdew and Wang (PW91) [40]. A sigma value of 0.2 eV and a plane wave energy cutoff of 1.3 times higher than the highest default cutoff were adopted. The Brillouin zone sampling was done with Blöchl corrections [39] using a gamma centered Monkhorst-Pack (MP) scheme [41]. The k-points grid used was an automated k-point mesh generator in VASP with the length of the subdivisions specified as 50 Å. The energy

convergence criterion of the electronic self-consistency was set as 10^{-4} eV atom^{-1} with a stopping criteria for the ionic relaxation loop of 10^{-4} eV A^{-1} for all of the calculations. In order to ensure the accuracy of the DFT-based first-principles calculations, the lattice parameters and equilibrium properties including volume (*V*), energy (*E*), bulk modulus (*B*), and first derivative of bulk modulus with respect to pressure (*B'*) were compared with both previous experimental and DFT-calculated results. The lattice parameters from the DFT-based first-principles calculations vary from the experimentally determined lattice parameters by less than 0.07 nm; this variance is quite small and can be attributed to the temperature difference between the calculations (0 K) and experiments (> 130 K). With the accuracy of the calculations verified, the enthalpy of formation of the intermetallic compounds is calculated at 0 K and plotted in Figure 28.

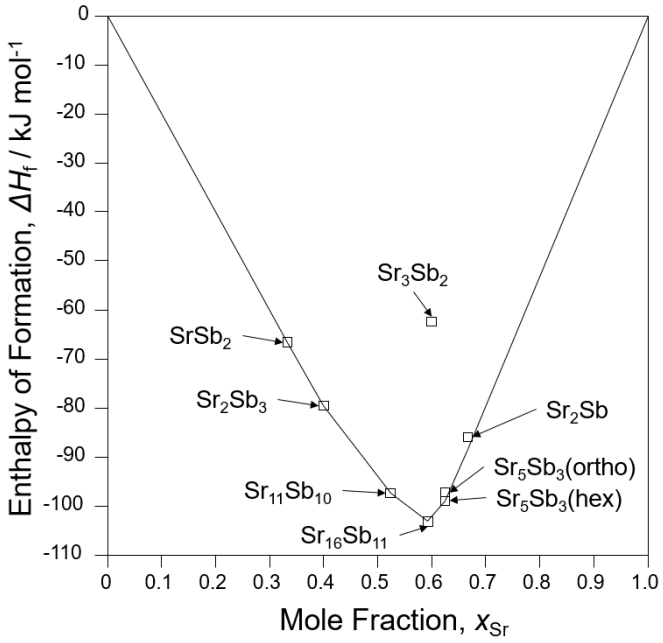

Figure 28. The formation energy of the intermetallics as a function of temperature from DFT-based first-principles calculations, where □ represent the enthalpies of formation computed via DFT and the line (convex hull) was determined using CALPHAD modeling.

The first-principles results indicate the stability of $Sr_{16}Sb_{11}$ and $Sr_{11}Sb_{10}$ as well as the Sr_2Sb, $SrSb_2$, and Sr_2Sb_3 phases as evidenced by their close proximity to the convex hull. In addition, Sr_5Sb_3 in the hexagonal structure is found to be more stable than the orthorhombic structure and Sr_3Sb_2 to be a metastable structure at all temperatures. Based on the excellent agreement between the first-principles analysis and the XRD measurements for the stability of $SrSb_2$, Sr_2Sb_3, $Sr_{11}Sb_{10}$, $Sr_{16}Sb_{11}$, Sr_5Sb_3 (hex), and Sr_2Sb phases, confidence in the experimentally determined results is increased.

The results of the first-principles calculations were used to assist in the thermodynamic CALPHAD modeling; the ThermoCalc software [24] was used to describe the Gibbs energy equations by the Redlich-Kister polynomial equations [42] described by:

$$G_m^{\phi} = x_A G_A^{\phi} + x_B G_B^{\phi} + RT(x_A \ln x_A + x_B \ln x_B) + {}^{E}G_m^{\phi} \quad (18)$$

, where x_A and x_B are mole fractions of pure elements A and B, respectively, and G_A^ϕ and G_B^ϕ are the pure element Gibbs energy functions taken from the SGTE database compiled by Dinsdale [43]. The second part of the equation describes the ideal interactions between the elements, where *R* is the ideal gas constant and *T* is the temperature. Finally, the excess Gibbs energy (${}^E G_m^\phi$) describes the non-ideal interactions between elements and is expressed [42]:

$$ {}^E G_m^\phi = x_A x_B \sum_j {}^j L^\phi (x_A - x_B)^j \quad (19)$$

, where ${}^j L^\phi$ is the interaction parameter described by:

$$ L^\phi = a + bT \quad (20)$$

, where *a* and *b* are modeled interaction parameters representing the enthalpy and entropy, respectively. Previous modeling of binary systems has shown that in most cases only two interaction parameters are needed to describe the non-ideal interaction between solution phases. The intermetallic compounds were treated as stoichiometric compounds (A_qB_p) and modeled by:

$$ G_m^{A_qB_p} = qGHSER_A + pGHSER_B + a + bT \quad (21)$$

, where a and b are fitting parameters representing the enthalpy and entropy, respectively, *p* and *q* represent the number of A and B in the stoichiometric compound and $GHSER_A$ and $GHSER_B$ represent the Gibbs energy functions of element A and B in their standard element reference state (SER) at ambient temperature and pressure (Sr is fcc and Sb is rhombohedral).

In order to describe the activity measurements observed in the liquid, the associate solution model is applied in the database. The associate species chosen in this model was Sr_3Sb_2 due to its high melting temperature, i.e. proximity to liquid phases; though $Sr_{16}Sb_{11}$ is the stable phase with the highest melting temperature, it was avoided as a result of the complexity of its crystal structure and size which would have slowed calculations down considerably. Sr_3Sb_2 is one of the closest phases to $Sr_{16}Sb_{11}$ and also represents the natural valence of the constituents, i.e. +2 for Sr and -3 for Sb, making it a reasonable substitute. The Gibbs energy of the associate species is described as,

$$ {}^0 G_{Sr_3Sb_2}^{Liq} = \frac{3}{5} {}^0 G_{Sr}^{Liq} + \frac{2}{5} {}^0 G_{Sb}^{Liq} + \mathrm{A} + \mathrm{BT} + \mathrm{CTlnT} \quad (22)$$

, where A, B, and C are the model parameters for the Gibbs energy of formation of the associate species relative to the pure Sr and Sb liquid phases. The results were used to assist in the thermodynamic CALPHAD modeling.

The developed CALPHAD model was used to predict the activity values of x_{Sr} at 988 K and was compared to the experimental results from the electromotive force measurements (Figure 29).

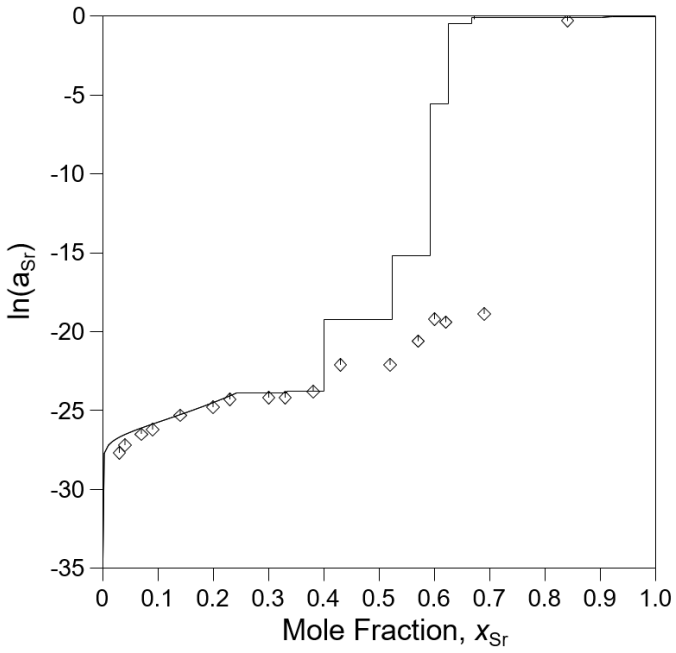

Figure 29. Comparison of modeled activity of Sr in Sb vs. the activity values determined from the electromotive force measurements at 988 K.

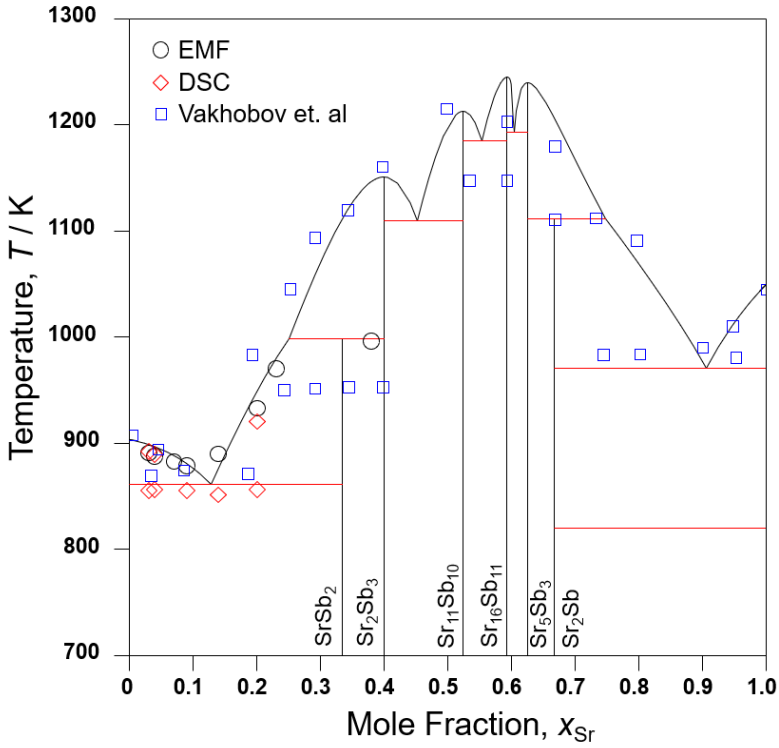

Figure 30. Computationally constructed Sr-Sb phase diagram using the CALPHAD technique, based on experimental data from emf/DSC measurements, first-principles calculations, as well as thermal analysis from Vakhobov et al. [41].

Table 15. Modeled parameters in SI units for the phases in the Sr-Sb binary system. These parameters were incorporated with the SGTE data for the pure elements.

Phase (model)	Modeled Parameters
fcc (Sr, Sb)	${}^{0}L^{\mathrm{fcc}}_{\mathrm{Sr,Sb}} = -19.888 + 1.052 * T$
Rhombohedral (Sr, Sb)	${}^{0}L^{\mathrm{rhom}}_{\mathrm{Sr,Sb}} = -25{,}926.413 + 0.995 * T$
Liquid (Sr, Sb)	$G^{\mathrm{liquid}}_{\mathrm{Sr3Sb2}} = 2 * G^{\mathrm{Liq}}_{\mathrm{Sb}} + 3 * G^{\mathrm{Liq}}_{\mathrm{Sr}} - 480{,}500 + 1.05 * T$
	${}^{0}L^{\mathrm{liquid}}_{\mathrm{Sr,Sr_3Sb_2}} = -15{,}006$
	${}^{0}L^{\mathrm{liquid}}_{\mathrm{Sr_3Sb_2,Sb}} = -110{,}110$
	${}^{1}L^{\mathrm{liquid}}_{\mathrm{Sr_3Sb_2,Sb}} = -35{,}000.8$
$SrSb_2$	$G^{\mathrm{SrSb_2}} = {}^{0}G^{\mathrm{fcc}}_{\mathrm{Sr}} + 2 * {}^{0}G^{\mathrm{rhom}}_{\mathrm{Sb}} - 199{,}922 - 7.7 * T$
Sr_2Sb_3	$G^{\mathrm{Sr_2Sb_3}} = 2 * {}^{0}G^{\mathrm{fcc}}_{\mathrm{Sr}} + 3 * {}^{0}G^{\mathrm{rhom}}_{\mathrm{Sb}} - 397{,}906.48 - 13 * T$
$Sr_{11}Sb_{10}$	$G^{\mathrm{Sr_{11}Sb_{10}}} = 11 * {}^{0}G^{\mathrm{fcc}}_{\mathrm{Sr}} + 10 * {}^{0}G^{\mathrm{rhom}}_{\mathrm{Sb}} - 2{,}045{,}599$
$Sr_{16}Sb_{11}$	$G^{\mathrm{Sr_{16}Sb_{11}}} = 16 * {}^{0}G^{\mathrm{fcc}}_{\mathrm{Sr}} + 11 * {}^{0}G^{\mathrm{rhom}}_{\mathrm{Sb}} - 2{,}785{,}080 + 66 * T$
Sr_5Sb_3	$G^{\mathrm{Sr_5Sb_3}} = 5 * {}^{0}G^{\mathrm{fcc}}_{\mathrm{Sr}} + 3 * {}^{0}G^{\mathrm{rhom}}_{\mathrm{Sb}} - 791{,}786 + 20.5 * T$
Sr_2Sb	$G^{\mathrm{Sr_2Sb}} = 2 * {}^{0}G^{\mathrm{fcc}}_{\mathrm{Sr}} + {}^{0}G^{\mathrm{rhom}}_{\mathrm{Sb}} - 265{,}438 + 6.9 * T$

Figure 29 presents the natural logarithm of activity values as a function of Sr mole fraction (x_{Sr}) at 988 K comparing the experimentally determined emf values with the activity predicted using the CALPHAD technique. The activity decreases as a function of x_{Sr} until hitting the liquidus composition, at which point it becomes essentially constant with respect to x_{Sr} in the two-phase regions; this invariance is a result of the chemical potential of Sr being constant in two-phase regions. The experimental values agree superbly with the CALPHAD-based model in the liquid phase, but begin to deviate from the theory further with when entering solid-solid phase regions. This phenomenon is likely due to the presence of non-equilibrium phases at higher x_{Sr} compositions indicated by the XRD measurements; for instance, trapped meta-stable Sr_5Sb_3 (hex) at x_{Sr} = 0.69 would result in a higher experimentally determined emf, i.e. lower activity, when compared to the theoretical model which assumes an x_{Sr} = 0.69 alloy to contain Sr_2Sb and Sr only.

Based on the emf and DSC data, as well as the first principles calculations, CALPHAD modeling was performed to develop the Sr-Sb phase diagram (Figure 30); model parameters are listed in Table 15.

The strength of the correlation between the experimentally determined XRD and emf data with the computational first-principles and CALPHAD analysis was useful in developing the Sr-Sb system and providing the more complete thermodynamic understanding possible. As such, refining previously analyzed systems using computational method in conjunction with the activity values and transitions determined using emf data will certainly be an aspect of future research in this field.

2.2.2 Thermodynamic modeling of the Ba-Bi System

The thermodynamic properties and phase stability of the Ba-Bi system were investigated computationally with the enthalpies of formation and the finite temperature thermodynamic properties of seven compounds predicted by first-principles calculations based on density functional theory (DFT), indicating five compounds ($BaBi_3$, $Ba_{11}Bi_{10}$, Ba_4Bi_3, Ba_5Bi_3, and Ba_2Bi) to be stable. The extremely low chemical activity of Ba in liquid for a wide range of temperatures and compositions indicates very strong short-range ordering in the liquid phase which is modeled in the present work by introducing the Ba_4Bi_3 and $BaBi_3$ associates in the liquid phase. Both thermodynamic and phase equilibrium data were then used to evaluate the model parameters in Gibbs energy functions of the five stable compounds and three solution phases of liquid, bcc, and rhombohedral phases by the CALPHAD technique. According to this work, the Ba-Bi system consists of three eutectic reactions, two peritectic reactions, one peritectoid reaction, and two congruent reactions, as well as that the concentrations of associates are very high in the liquid phase with very low concentration of atomic Ba, which provides the fundamental understanding as to why Bi can be used to remove Ba ions from molten salt solutions.

The enthalpy of formation for each intermetallic compound is plotted in **Error! Reference source not found.** at 300 K and 970 K. Based on the results, five intermetallics $BaBi_3$, $Ba_{11}Bi_{10}$, Ba_4Bi_3, Ba_5Bi_3, and Ba_2Bi are stable, which agrees with the conclusions by Lichtenstein et al. [44]. The Ba_3Bi_2 phase is shown to be unstable which also agrees with the work by Lichtenstein et al. [44]. First-principles results show that the Ba_2Bi_3 phase has a formation energy close to the convex hull at low temperatures; however, it is not stable at high temperatures and was not observed at 723-1073 K based on the experimental work by Lichtenstein et al. [44]

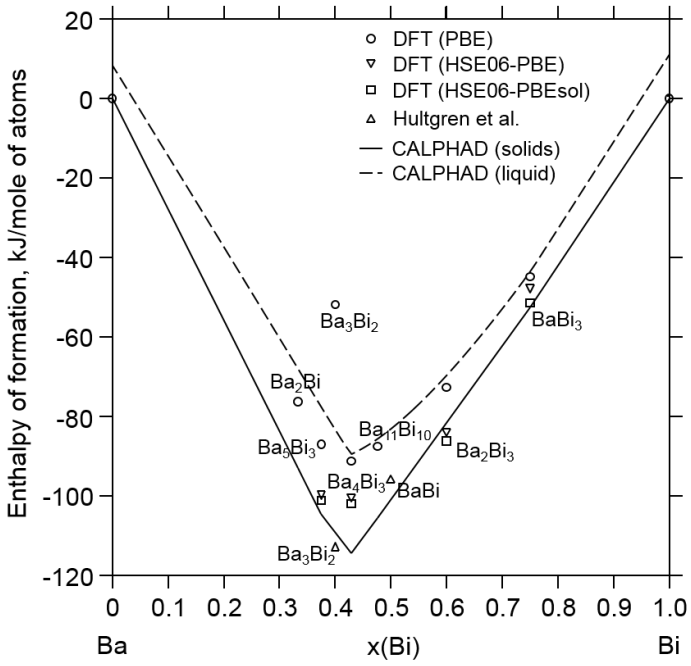

Figure 31. Enthalpies of formation of the solids (solid line) and the liquid (dash line) at 300 K from the present CALPHAD modeling and the present first-principles results for solids at 300 K by PBE, HSE06-PBE, and HSE06-PBEsol together with the experimental enthalpies of formation at 298 K by Hultgren et al. [45].

Table 16. Thermodynamic models and model parameters (in SI units) for the Ba-Bi phases. These parameters are incorporated with the SGTE data starting with GHSER [43].

Phase	model	Thermodynamic parameters
Liquid	(Ba, Ba_4Bi_3, $BaBi_3$, Bi)$_1$	${}^0G^{\mathrm{Liq}}_{\mathrm{Ba_4Bi_3}} = 4\ {}^0G^{\mathrm{Liq}}_{\mathrm{Ba}} + 3\ {}^0G^{\mathrm{Liq}}_{\mathrm{Bi}} - 692362$
		${}^0G^{\mathrm{Liq}}_{\mathrm{BaBi_3}} = {}^0G^{\mathrm{Liq}}_{\mathrm{Ba}} + 3\ {}^0G^{\mathrm{Liq}}_{\mathrm{Bi}} - 215939 + 3.5T$
		${}^0L^{\mathrm{Liq}}_{\mathrm{Ba,Ba_4Bi_3}} = -7000 - 10T$
		${}^1L^{\mathrm{Liq}}_{\mathrm{Ba,Ba_4Bi_3}} = +8000 - 20T$
		${}^0L^{\mathrm{Liq}}_{\mathrm{Ba_4Bi_3,BaBi_3}} = -103112 + 49.1T$
		${}^1L^{\mathrm{Liq}}_{\mathrm{Ba_4Bi_3,BaBi_3}} = 2223$
		${}^0L^{\mathrm{Liq}}_{\mathrm{BaBi_3,Bi}} = -515 - 3.0T$
Bcc	(Ba, Bi)$_1$	${}^0L^{\mathrm{Bcc}}_{\mathrm{Ba,Bi}} = +18002$
Rhom_A7	(Ba, Bi)$_1$	${}^0L^{\mathrm{Rhom}}_{\mathrm{Ba,Bi}} = +1023$
		${}^0G^{\mathrm{Rhom}}_{\mathrm{Ba}} = +\mathrm{GHSER}_{\mathrm{Ba}} + 101333$
$BaBi_3$	$(Ba)_{0.25}(Bi)_{0.75}$	${}^0G^{\mathrm{BaBi_3}}_{\mathrm{Ba:Bi}} = +0.25\mathrm{GHSER}_{\mathrm{Ba}} + 0.75\mathrm{GHSER}_{\mathrm{Bi}} - 52567 - 7.5T$
$Ba_{11}Bi_{10}$	$(Ba)_{0.5238}(Bi)_{0.4762}$	${}^0G^{\mathrm{Ba_{11}Bi_{10}}}_{\mathrm{Ba:Bi}} = +0.5238\mathrm{GHSER}_{\mathrm{Ba}} + 0.4762\mathrm{GHSER}_{\mathrm{Bi}} - 105443 + 6.1T$
Ba_4Bi_3	$(Ba)_{0.5714}(Bi)_{0.4286}$	${}^0G^{\mathrm{Ba_4Bi_3}}_{\mathrm{Ba:Bi}} = +0.5714\mathrm{GHSER}_{\mathrm{Ba}} + 0.4286\mathrm{GHSER}_{\mathrm{Bi}} - 114444 + 9.7T$
Ba_5Bi_3	$(Ba)_{0.625}(Bi)_{0.375}$	${}^0G^{\mathrm{Ba_5Bi_3}}_{\mathrm{Ba:Bi}} = +0.625\mathrm{GHSER}_{\mathrm{Ba}} + 0.375\mathrm{GHSER}_{\mathrm{Bi}} - 104421 + 11.7T$
Ba_2Bi	$(Ba)_{0.667}(Bi)_{0.333}$	${}^0G^{\mathrm{Ba_2Bi}}_{\mathrm{Ba:Bi}} = +0.667\mathrm{GHSER}_{\mathrm{Ba}} + 0.333\mathrm{GHSER}_{\mathrm{Bi}} - 92780 + 10.5T$

Table 16 summarizes the present thermodynamic models and model parameters for the Ba-Bi system. Figure 32 shows the calculated Ba-Bi phase diagram, which is nearly identical to the one proposed by Lichtenstein et al. [44], excepting a few experimental points at the Ba-rich side as discussed above [44]. In addition, the work by Grube and Dietrich [46] is mostly reproduced by the present thermodynamic description; however, in some cases Grube and Dietrich's results [46] as well as those from Zhuravlev and Smirnova [47], vary from both the present modeling results and the results by Lichtenstein et al. [44] and hence are thought to be less reliable.

The strength of the correlation between the experimentally emf data with the computational first-principles and CALPHAD analysis was useful in developing the Sr-Sb and Ba-Bi systems and providing the most complete thermodynamic understanding possible. As such, refining previously analyzed systems using computational method in conjunction with the activity values and transitions determined using emf data will certainly be an aspect of future research in this field.

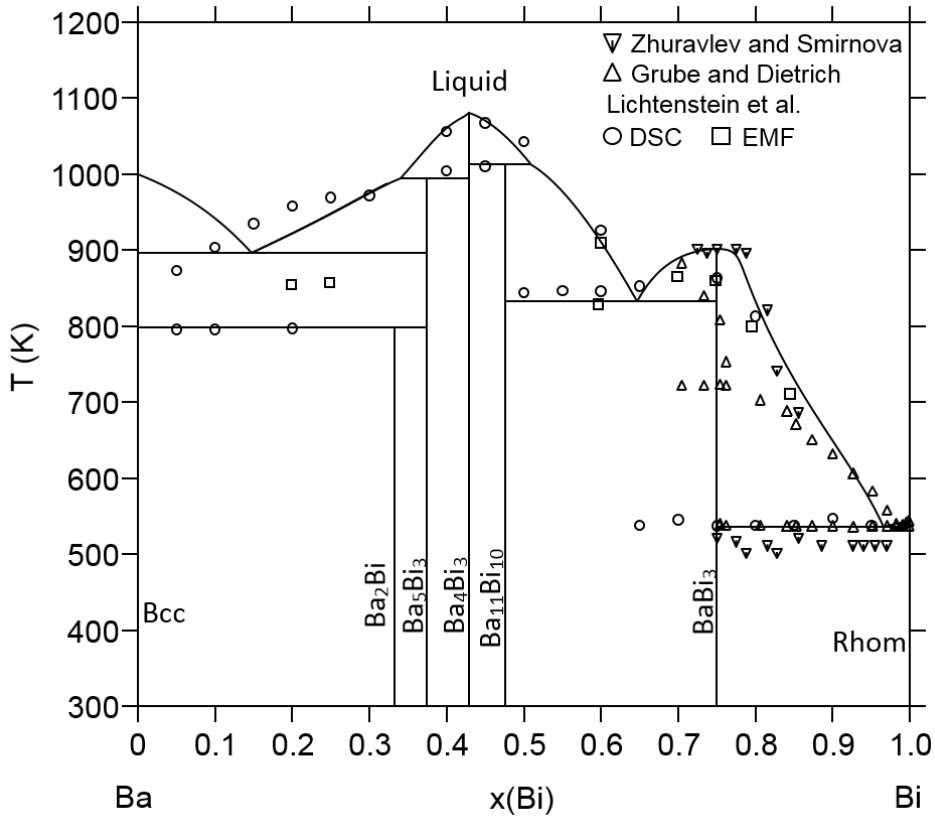

Figure 32. Calculated Ba-Bi phase diagram using the present thermodynamic description compared with experimental data by Lichtenstein et al. [44], Grube and Dietrich [46], and Zhuravlev and Smirnova [47]. The peritectoid reaction Ba_5Bi_3 + Bcc → Ba_2Bi is determined from the present modeling and the supplemental XRD in the present work.

2.3 Recovery of Alkali/Alkaline-Earth Elements into Liquid Metals

2.3.1 Experimental

Due to the hygroscopic nature of chloride salts and reactivity of alkaline-earth metals, all preparations were handled in an argon filled glovebox (<1 ppm O_2, <1.5 ppm H_2O) to prevent reactions with moisture and oxygen.

Electrolytes: Electrolytes were prepared from appropriate weights of LiCl (Ultra dry, 99.9%, Alfa Aesar, Product No. 14540), KCl (Ultra dry, 99.95%, Alfa Aesar, Product No. 14466), $SrCl_2$ (anhydrous, 99.5%, Alfa Aesar, Product No. 16790) and $BaCl_2$ (anhydrous, 99.998%, Alfa Aesar, Product No. 10995). The nominal compositions of the mixtures were eutectic LiCl-KCl (59.2-40.8 mol%) containing 5 mol% total of $SrCl_2$ and/or $BaCl_2$, e.g., LiCl-KCl-$SrCl_2$ (56.7-38.3-5 mol%) or LiCl-KCl-$SrCl_2$-$BaCl_2$ (56.7-38.3-2.5-2.5 mol%). The mixture at each specified composition was placed in a quartz crucible (Technical Glass Products) for premelting in a stainless steel vacuum chamber. The chamber was loaded into a crucible furnace (Mellen, CC-12), initially evacuated to less than 10 mtorr, and heated under vacuum at 100 °C for 12 h and at 270 °C for 12 h to remove residual moisture. Then, the chamber was purged with ultra-high purity argon three times and heated to 700 °C for 3 h under a slowly flowing (50 mL min^{-1}) argon atmosphere for premelting the electrolyte. After cooling, the dry and homogeneous electrolyte was ground into a fine powder for electrochemical assembly.

Electrodes: The Bi working electrodes (WEs) were prepared from bismuth pieces (99.999%, Sigma Aldrich, Product No. 556130) by melting 3.50 g of Bi in a boron nitride (BN) crucible (Saint-Gobain Advanced Ceramics, Product No. AX05), using an induction heater (IH15A-2T, Across International) custom installed inside the glove box. The dimensions of the BN crucible were 20 mm in height, 12 mm outer diameter, 8 mm inner diameter, and 15 mm in depth, giving a nominal surface area of 0.5 cm^2. A tungsten wire (99.95%, Thermo Shield, 1 mm diameter) was inserted into the liquid Bi to establish electrical contact during inducting heating. In the three-electrode cells, a graphite cylinder (0.95 cm in diameter and 5 cm in length) was used as the counter electrode (CE), female threaded at the top and connected to a male threaded steel rod for electrical connection.

The Ag/Ag^+ reference electrode (RE) was constructed using a closed one end mullite tube (6.4 mm in outer diameter and 45.7 cm in length) which contained ~0.5 g of LiCl-KCl-AgCl electrolyte and Ag wire (1 mm in diameter and 48.3 cm in length, 99.9%, Alfa Aesar, Product No. 11434) to establish a reversible half-cell potential (Ag/Ag^+). The reference electrolyte was prepared using the same procedures as described earlier by adding 1 wt% of AgCl (anhydrous, 99.998%, Sigma Aldrich, Product no. 449571) into eutectic LiCl-KCl.

Cell assembly: The electrodes and thermocouple (ASTM Type K) were arranged inside an alumina crucible (60 mm in diameter and 100 mm in height; Advalue Technology, Product No. AL-2250) and then, approximately 100 g of the electrolyte was poured over the electrodes. The assembled cell was placed into a test chamber; the chamber was sealed inside the glovebox and loaded into a crucible furnace. The chamber was first evacuated and dried, following a similar procedure for preparing the electrolytes, then purged with ultra-high purity argon gas three times and heated to 500 °C under a slowly flowing (50 mL min^{-1}) argon atmosphere. The electrodes were allowed to equilibrate for 12 h at 500 °C for electrochemical measurements and the cell

temperature was monitored and recorded using a data acquisition board (National Instruments, NI 9211).

Electrochemical deposition into liquid Bi was implemented using the graphite CE and the Ag/Ag^+ RE at 500 °C, in eutectic LiCl-KCl electrolytes with the addition of 5 mol% total of $SrCl_2$ and/or $BaCl_2$. The Bi WEs were cathodically discharged to the specific charge capacity (coulombs per gram of Bi) of 270 C g^{-1} under constant current control (j = –50 mA cm^{-2}) using a potentiostat-galvanostat (Autolab PGSTAT302N). After each deposition experiment, the cell was cooled to room temperature and the discharged Bi electrodes were isolated from the cell assembly. The Bi electrodes were rinsed with deionized water to remove entrained salt from the surface, and cross-sectioned for compositional and microstructural analyses. The electrodes were mounted in epoxy, polished using silicon carbide emery paper (up to 1200 grit) with mineral oil as a lubricant to minimize reaction with moisture and oxygen, and characterized using a scanning electron microscope (SEM, FEI Quanta 200) fitted with energy dispersive X-ray spectroscopy (EDS) capabilities. The compositions of the Bi WEs were also determined using inductively coupled plasma-atomic emission spectroscopy (ICP-AES, Perkin-Elmer Optima 5300DV) with an accuracy of 4% of the measured value.

2.3.2 Results

In order to establish a thermodynamic basis for separating Sr and Ba from LiCl-KCl-$SrCl_2$-$BaCl_2$ electrolytes at 500 °C, the equilibrium potentials of the liquid Bi electrode were first analyzed based on the thermodynamic properties of binary (Li, K, Sr, Ba)-Bi systems. The half-reaction of each constituent A (= Li, K, Sr, and Ba) in liquid Bi is written as:

$$A^{z+} + ze^- = A(\text{in Bi}) \tag{23}$$

where z is the number of electrons exchanged in each half-reaction (z = 1 for alkali and z = 2 for alkaline-earth elements). The equilibrium potential (E_A^{eq}) of each half-reaction is determined according to the Nernst equation:

$$E_A^{eq} = E_A^0 - \frac{RT}{zF}\ln\left(\frac{a_{A(\text{in Bi})}}{a_{A^{z+}}}\right) \quad \text{vs. } Cl^-/Cl_2(g) \tag{24}$$

where E_A^0 is the standard potential of the A^{z+}/A couple (vs. $Cl^-/Cl_2(g)$) in pure supercooled liquid chloride[48], R is the ideal gas constant, T is absolute temperature, F is Faraday's constant, $a_{A(\text{in Bi})}$ is the activity of metal A in Bi, and $a_{A^{z+}}$ is the activity of cation A^{z+} in the electrolyte which is assumed to be unity by taking pure supercooled liquid chloride as the standard state ($a_{A^{z+}}$ = 1). The activity values of A (= Li, K, Sr, and Ba) in liquid Bi were experimentally determined by the electromotive force (emf) technique where the emf values were measured between the pure metal A and A-Bi alloys as functions of both temperature and mole fraction, $x_{A(\text{in Bi})}$ using the A (pure) | A^{z+} | A(in Bi) electrochemical cell.[7,22,44,49] For these measurements, the emf is given by:

$$\text{emf} = -\frac{RT}{zF}\ln a_{A(\text{in Bi})} \tag{25}$$

and provides a direct measure of the activity ($a_{A(\text{in Bi})}$). By incorporating (Eq. 25) into (Eq. 24), the following relation is obtained:

$$E_{\mathrm{A}}^{\mathrm{eq}} = E_{\mathrm{A}}^{0} + \mathrm{emf} \quad \text{vs. } \mathrm{Cl^-/Cl_2(g)} \tag{26}$$

, indicating that the emf values represent the shift in electrode potentials away from the standard potential dependent upon the strength of chemical interactions (solution properties) of each A-Bi alloy.

In order to facilitate comparison between alkali/alkaline-earth constituents, we selected two emf values at mole fractions of $x_{\mathrm{A(in\ Bi)}} = 0.05$ and $x_{\mathrm{A(in\ Bi)}} = 0.10$ for each constituent and compared the relative shift in electrode potentials utilizing the currently available emf values of A-Bi alloys, with the recent data for Sr-Bi and Ba-Bi[7,44]. The quantitative results at 500 °C are summarized in Table 17 and presented graphically in Figure 33. Comparing the series of electrode potentials in standard states (E_{A}^{0}) and in the liquid Bi ($E_{\mathrm{A}}^{\mathrm{eq}}$) in Figure 33, the sequence of deposition changes from [Li → Sr → K → Ba] in standard states to [Ba → Sr → Li → K] in liquid Bi for selected mole fractions ($x_{\mathrm{A(in\ Bi)}} = 0.05$–$0.10$). Clearly, the larger emf values of Sr and Ba in Bi resulted in a drastic change in the electrode potentials of Sr and Ba in liquid Bi, supporting the notion that the deposition of Sr and Ba becomes thermodynamically achievable using liquid Bi. In addition, the experimentally verified activity coefficient of Ba in Bi at $x_{\mathrm{Ba(in\ Bi)}} = 0.05$ was 1.3×10^{-11} at 723 °C[44], which is five orders of magnitude lower than the value estimated by Matsumiya et al.: $\gamma_{\mathrm{Ba(in\ Bi)}} = 10^{-6}$ at 723 °C[50].

Table 17. Standard potentials ($\boldsymbol{E_{\mathrm{A}}^{0}}$) of A^{z+}/A redox couple (A = Li, K, Sr, and Ba) in pure supercooled liquid chloride vs. $Cl^-/Cl_2(g)$ [48], experimentally determined emf values of A-Bi alloys at mole fractions of $x_{\mathrm{A(in\ Bi)}} = 0.05$ and $x_{\mathrm{A(in\ Bi)}} = 0.10$ [7,22,44,49], and the resultant equilibrium potentials of A in Bi ($\boldsymbol{E_{\mathrm{A}}^{\mathrm{eq}}}$) vs. $Cl^-/Cl_2(g)$ according to (Eq. 26) at 500 °C.

A	E_{A}^{0} (V)* vs. $Cl^-/Cl_2(g)$	*emf* (V)		$E_{\mathrm{A}}^{\mathrm{eq}}$ (V) vs. $Cl^-/Cl_2(g)$	
		$x_{\mathrm{A(in\ Bi)}} = 0.05$	$x_{\mathrm{A(in\ Bi)}} = 0.10$	$x_{\mathrm{A(in\ Bi)}} = 0.05$	$x_{\mathrm{A(in\ Bi)}} = 0.10$
Li	–3.550	0.924	0.874	–2.626	–2.676
K	–3.690	0.967	0.906	–2.723	–2.784
Sr	–3.623	1.004	0.972	–2.619	–2.651
Ba	–3.755	1.164	1.137	–2.591	–2.618

*: calculated from the free energy of formation of pure chlorides in the supercooled liquid state[48]: $\mathrm{A(l,s)} + \frac{z}{2}\mathrm{Cl_2(g)} = \mathrm{ACl}_z\mathrm{(l)}$.

It should be noted that the equilibrium potentials of each A-Bi alloy continuously change from the standard potential in the positive direction due to the formation of an A-Bi solution phase over an entire composition range, and thus the estimated potentials will overlap among alkali/alkaline-earth elements (A = Li, K, Sr, and Ba). In other words, each constituent in liquid Bi can have the same electrode potential as the composition of the electrode changes, implying the possibility of co-deposition of multiple components into the interacting Bi electrode. For example, during cathodic discharge one may anticipate the co-deposition of Ba, Sr, Li, and K into Bi at a given potential (e.g., –2.60 V vs. $Cl^-/Cl_2(g)$) with Ba being the most abundant and K the least (Figure 33).

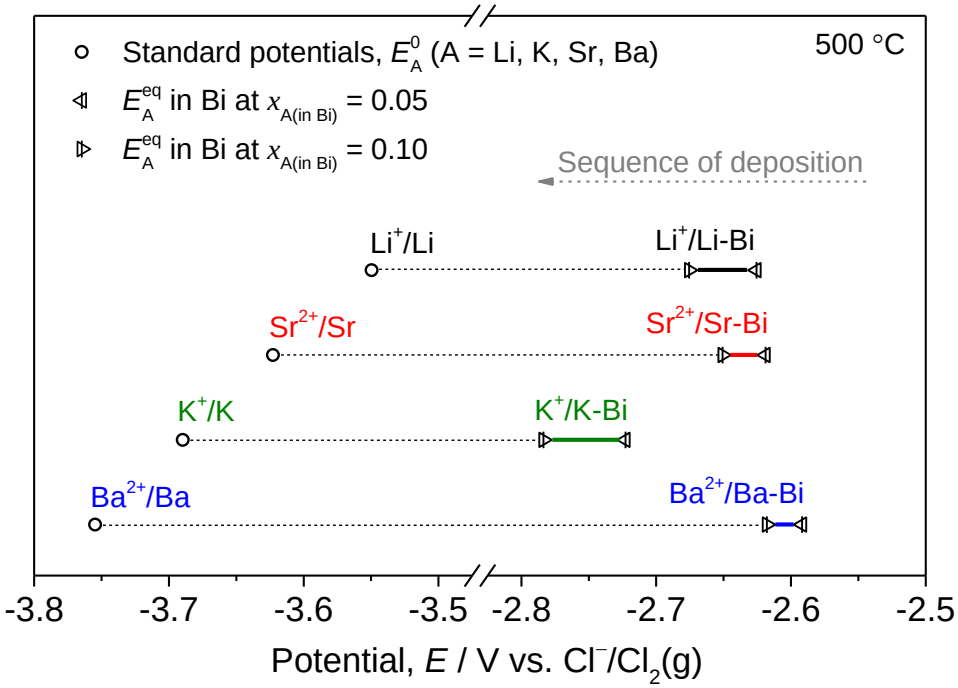

Figure 33. Graphical representation of standard potentials ($\boldsymbol{E^0_A}$) of A^{z+}/A redox couple (A = Li, K, Sr, and Ba) in pure supercooled liquid chloride (open circle), compared to equilibrium potentials of A in liquid Bi ($\boldsymbol{E^{eq}_A}$) at constant mole fractions of $x_{A(in\ Bi)}$ = 0.05 and $x_{A(in\ Bi)}$ = 0.10 (open triangle) at 500 °C.

Based upon the thermodynamic projection described above, liquid Bi electrodes were cathodically discharged in three-electrode cells using a graphite counter electrode and a Ag/Ag^+ reference electrode under a constant current density (j = –50 mA cm^{-2}) at 500 °C. The electrode potentials of liquid Bi were measured in eutectic LiCl-KCl electrolytes by adding 5 mol% total of $SrCl_2$ and/or $BaCl_2$, up to a specific charge capacity of 270 C g^{-1} (Figure 34). The addition of less conductive $SrCl_2$ and $BaCl_2$ in eutectic LiCl-KCl electrolyte would typically result in an increased solution resistance, leading to an increased ohmic potential drop in the negative direction during cathodic discharge. Conversely, the addition of 5 mol% $SrCl_2$ or $BaCl_2$ in eutectic LiCl-KCl resulted in the electrode potentials being shifted in the positive direction, compared to the potentials obtained in the binary eutectic LiCl-KCl electrolyte where lithium is the predominant electroactive species (Figure 34). More specifically, the change in electrode potentials from eutectic LiCl-KCl was 3–28 mV in LiCl-KCl-$SrCl_2$ (56.7-38.3-5 mol%) and 43–118 mV in LiCl-KCl-$BaCl_2$ (56.7-38.3-5 mol%). This behavior agrees with the thermodynamic analyses which suggest that (1) the deposition potentials of both Sr and Ba are more positive than Li and K due to their stronger chemical interactions with Bi and (2) the potentials of Ba-Bi are more positive than those of Sr-Bi (Figure 33). The electrode potentials in quaternary electrolytes containing both $SrCl_2$ and $BaCl_2$ were also more positive than the LiCl-KCl eutectic, but located between LiCl-KCl-$BaCl_2$ and LiCl-KCl-$SrCl_2$ electrolytes.

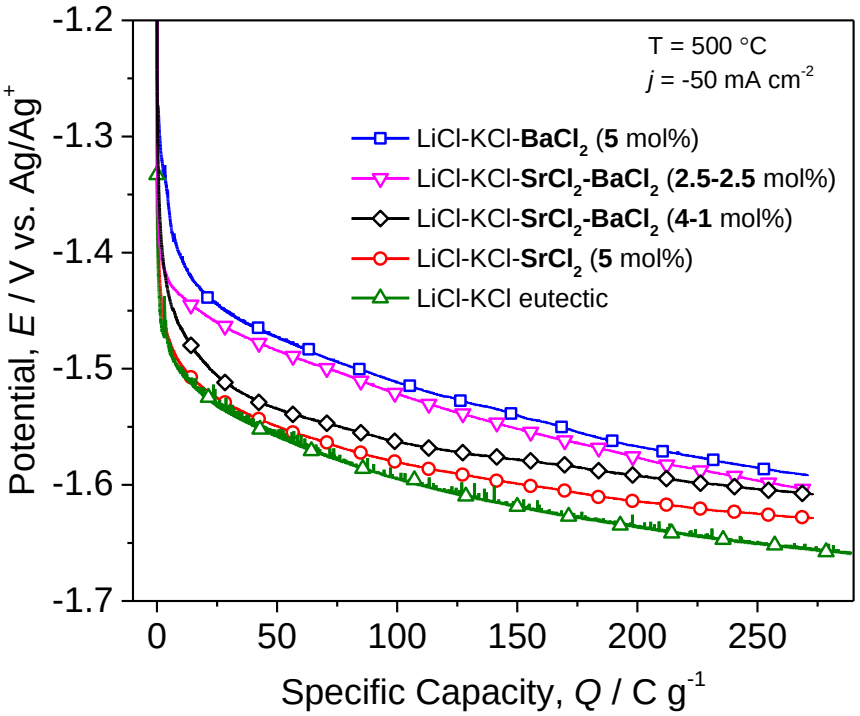

Figure 34. Electrode potential of liquid Bi (vs. Ag/Ag^+) at a constant current density (j = –50 mA cm^{-2}) and 500 °C as a function of specific charge capacity in eutectic LiCl-KCl (59.2-40.8 mol%) electrolytes with the addition of 5 mol% total of $SrCl_2$ and/or $BaCl_2$.

The discharged electrodes were cooled and characterized to verify the composition of the deposited products in Bi using SEM-EDS and ICP-AES. The microstructural features of the Bi electrode, elucidated by SEM-EDS, included a Bi matrix as well as intermetallic phases of Sr-Bi (29-71 mol%) in LiCl-KCl-$SrCl_2$, Ba-Bi (31-69 mol%) in LiCl-KCl-$BaCl_2$, and Sr-Ba-Bi (13-13-74 mol%) in LiCl-KCl-$SrCl_2$-$BaCl_2$, confirming the deposition of Sr and Ba into liquid Bi (Figure 35). In general, the detected phase constituents and their compositions in the discharged Bi electrodes qualitatively agreed with the phase behavior reported for binary Sr-Bi and Ba-Bi systems: [Bi + $SrBi_3$] and [Bi + $BaBi_3$], respectively.[7,44] However, there existed an unidentified region where both Sr and Bi were depleted (e.g., dark region in Figure 35a), suggesting the presence of the light-element Li, which cannot be detected by EDS.

Quantitative compositions of Bi electrodes were determined using ICP-AES, summarized in Table 18. In addition to confirming the deposition of Sr and Ba by EDS, the presence of Li in Bi electrodes was evident for all the tested electrodes with 5.9–16.2 mol% of Li and minimal presence of K (< 0.9 mol%), confirming that the dominant cathodic reactions were the co-deposition of Sr, Ba, and Li. The overall coulombic efficiency of the discharge process was estimated to be 63–67% by comparing the charge required for the measured electrode composition (Table 18) to the total charge passed during electrolysis (270 C g^{-1}). The loss in coulombic efficiency is thought to come from the high reactivity of alkali/alkaline-earth metals which could result in their selective loss during the sample preparation using deionized water to eliminate entrained salts for ICP-AES, and back dissolution of alkali/alkaline-earth elements into the electrolyte during electrolysis up to 270 C g^{-1} at 500 °C.

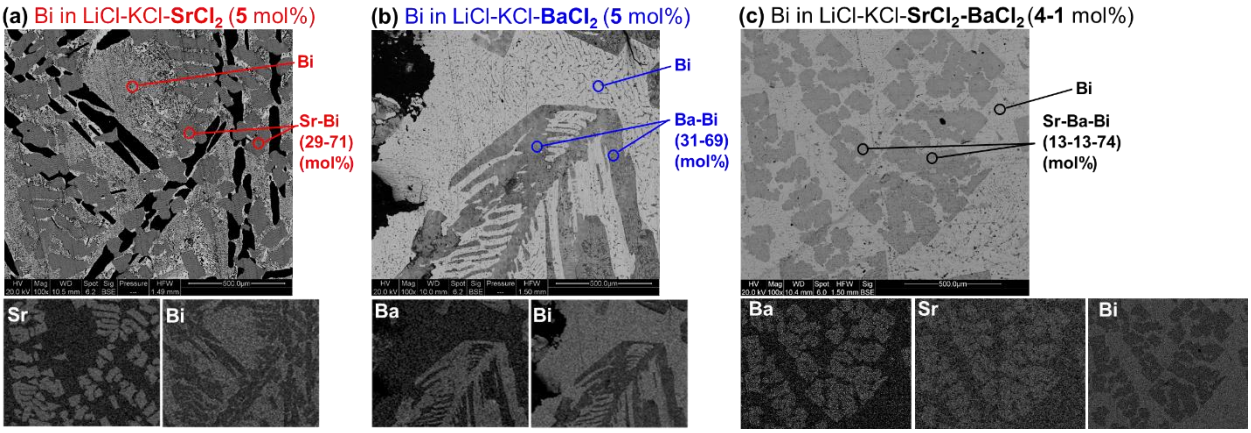

Figure 35. SEM and elemental X-ray mapping images of Bi electrodes after deposition to the specific capacity of 270 C g^{-1} at 500 °C in (a) LiCl-KCl-$SrCl_2$ (56.7-38.3-5 mol%), (b) LiCl-KCl-$BaCl_2$ (56.7-38.3-5 mol%), and (c) LiCl-KCl-$SrCl_2$-$BaCl_2$ (56.7-38.3-4-1 mol%).

Table 18. The composition of Bi electrodes after deposition to the specific capacity of 270 C g^{-1} at 500 °C in eutectic LiCl-KCl electrolytes containing 5 mol% total of $SrCl_2$ and/or $BaCl_2$ by ICP-AES and the estimated coulombic efficiency.

$SrCl_2$-$BaCl_2$ in electrolyte (mol%)	Composition of Bi electrode (mol%)					Coulombic efficiency (%)
	Li	K	Sr	Ba	Bi	
5.0-0.0 ($SrCl_2$ only)	16.2	0.7	6.5	—	76.6	67%
4.0-1.0	10.9	0.9	4.5	4.1	79.6	63%
2.5-2.5	7.8	0.6	2.0	8.7	80.9	63%
0.0-5.0 ($BaCl_2$ only)	5.9	0.3	—	12.8	81.0	67%

The composition of Sr and Ba in the Bi electrode increased with increased $SrCl_2$ and $BaCl_2$ content in the electrolytes. In the equimolar $SrCl_2$-$BaCl_2$ (2.5-2.5 mol%) electrolyte, the electrode potentials approached those of the electrolyte containing 5 mol% $BaCl_2$ (Figure 34), resulting in more preferential deposition of Ba (8.7 mol%) than Sr (2.0 mol%) in Bi. Interestingly, the composition of Li in Bi also increased with increased $SrCl_2$ in the electrolytes. This trend can be understood from the fact that the increased $SrCl_2$ content in the electrolyte resulted in the electrode potentials shifting in the negative direction (Figure 34) where the potentials reflect more prominent deposition of Li, according to the thermodynamic analyses (Figure 33). For the same reason, the minimum composition of Li in Bi (5.9 mol%) was obtained in the electrolyte containing 5 mol% $BaCl_2$ where electrode potentials were the most positive.

Overall, the electrode potentials and the compositions of Bi electrodes were qualitatively consistent with the thermodynamic analyses based upon the binary solution properties of A-Bi alloys in pure liquid chloride; however, understanding the quantitatively measured compositions of co-deposited products in Bi would require sophisticated models (e.g., Li-Sr-Ba-Bi) beyond the simple binary A-Bi solution. In practice, the detailed composition and distribution of the alkali/alkaline-earth constituents in Bi will require the activity of each constituent in the multi-component electrolytes beyond the standard state assumption above, as well as the comparison of electrode kinetics among the electroactive constituents at each stage of discharge.

2.4 Electrochemical studies of alkali/alkaline-earth elements and Bi

The electrochemistry of Ba, Cs, and Sr on a liquid Bi cathode has been studied via cyclic voltammetry (CV) and electrochemical impedance spectroscopy (EIS) techniques. Data sets from these techniques have been used to inform about the electrochemical potential, charge transfer kinetics, ohmic losses, and mass transport properties of alkali/alkaline-earth species at the electrode-electrolyte interface. These properties are important for understanding of the fundamental electrochemical behavior of these ions within the LiCl-KCl/Bi system.

2.4.1 Experimental

All experiments and sample preparations were performed inside an argon-atmosphere glovebox with oxygen and moisture levels maintained below 5 ppm. A Kerrlab automelt furnace was used in $BaCl_2$ experiments for drying and maintaining the high temperatures of the experimental apparatus. There were several issues with the Kerrlab automelt furnace; therefore, a change was made to use a Thermofisher benchtop furnace. Prior to experimentation, salts were dried for 5 hours at 573 K and then melted at 723 K for 24 hours. All current and potential measurements were performed using a Biologic VSP-300 potentiostat. Table 19 gives a description of the materials used in the experiments and a diagram of the experimental cell is shown in Figure 36.

For CV experiments, an experimental program was created to produce voltammograms of the LiCl-KCl system with and without addition of the salt species of interest at temperatures of 723–823 K and scan rates of 10–1000 mV/s. First, voltammograms of the pure LiCl-KCl system were produced at all experimental temperatures and scan rates. Then, the species of interest was added (0.5–4.0 wt%) and voltammograms were obtained. In order to study the electrochemical behavior from the species of interest, the background CV without electroactive component was subtracted, as shown in Figure 37.

Table 19. Description of materials used in electrochemical cell.

Materials	**Specifications**	**Materials**	**Specifications**
Vessel & Safety Vessel	Crucible (Coorstek 99.8%)	Counter Electrode	2mm Glassy Carbon rod (HTW)
Working Electrode	Liquid Bismuth (Alfa Aesar 99.99%) with 0.5 mm Molybdenum wire lead, within Pyrex crucible attached to 5mm Pyrex tube	Reference Electrode	1 mm Ag Wire in LiCl-KCl-5mol%AgCl (Alfa Aesar), within 7mm Pyrex tube with custom thinned bottom
LiCl-KCl	41.8 mol% KCl – 58.2 mol% LiCl (Alfa Aesar 99.99%)	Thermocouple with alumina sheath	K-type thermocouple (Omega), alumina sheath (Coorstek 99.8%)
$BaCl_2$	Ampoules (Alfa Aesar 99.99%)	CsCl	Ampoules (Alfa Aesar 99.99%)
$SrCl_2$	Ampoules (Alfa Aesar 99.99%)	$CeCl_3$	Ampoules (Alfa Aesar 99.99%)

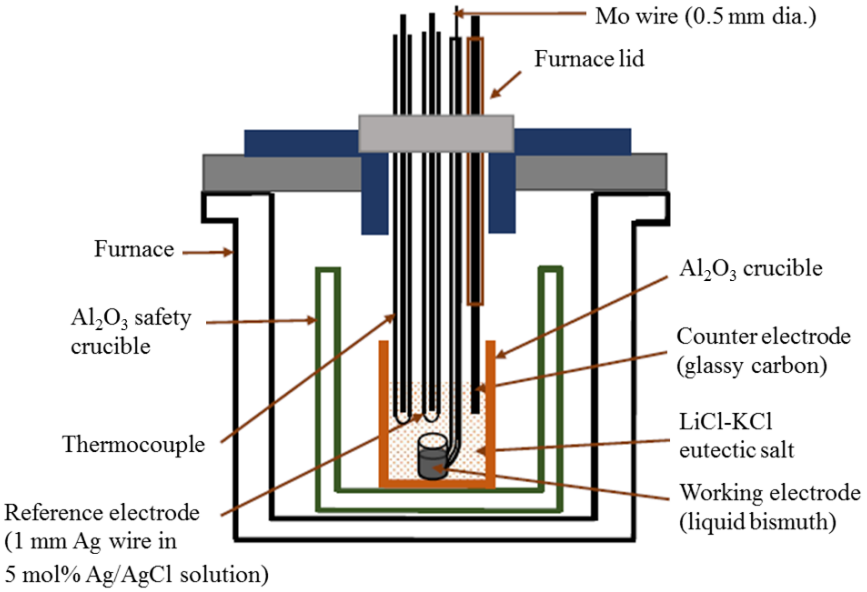

Figure 36. Diagram of electrochemical cell used in experiments.

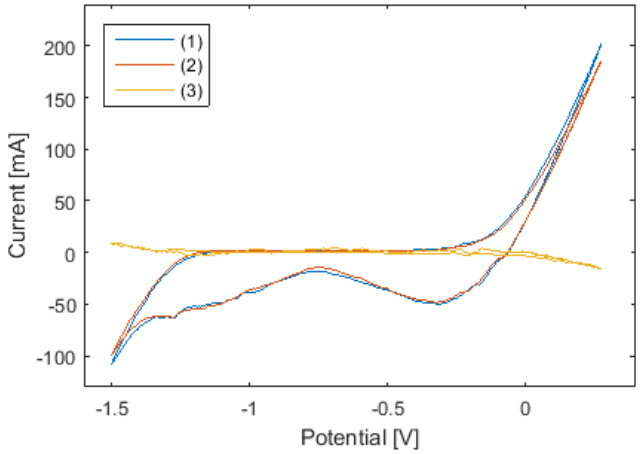

Figure 37. Subtraction method to eliminate background current of LiCl-KCl (1) from LiCl-KCl-$BaCl_2$ (1 wt%) (2), to give only the electrochemical behavior of barium (3).

2.4.2 Results

Current-potential (I-V) behavior: We have noted in general that the alkali/alkaline-earth species of interest are not very electroactive on the Bi cathode. Representative subtraction CVs are shown for Sr, Cs, and Ba in Figure 38. Subtraction CV curves for $SrCl_2$ system (798 K, 25 mV/s), CsCl system (773 K, 150 mV/s), and $BaCl_2$ system (798 K, 200 mV/s).Figure 38. In the case of Sr, the reduction and oxidation of Li at the negative end of the potential window was inhibited, leading to the positive current peak during the negative sweep and the negative current peak during the positive sweep. Cs exhibited two small redox peaks, one with a reduction potential of approximately -1.15 V and another with reduction potential -1.35 V. The presence of Ba in the LiCl-KCl resulted in a small reduction at approximately -1.4 V and a much larger oxidation at approximately -1.2 V. This could be the result of an intermetallic of Ba-Bi.

During experimental testing, we studied the behavior of $CeCl_3$ in the LiCl-KCl/liquid Bi system to compare the results with a similar system and validate the experimental design [51]. The

electrochemical behavior of $CeCl_3$ in our system was similar in a satisfactory way and served to confirm the results of our systems containing Sr, Ba, and Cs. Representative subtraction CVs for the $CeCl_3$ system are shown in Figure 39.

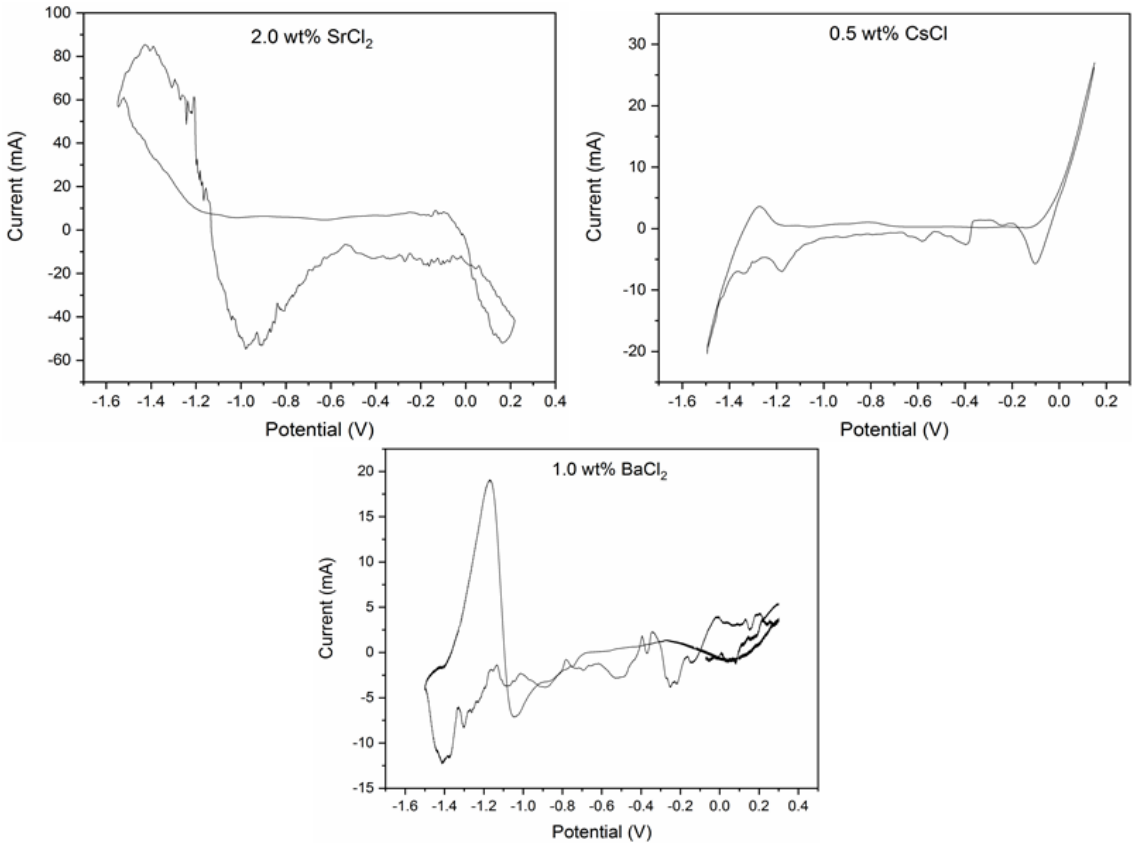

Figure 38. Subtraction CV curves for $SrCl_2$ system (798 K, 25 mV/s), CsCl system (773 K, 150 mV/s), and $BaCl_2$ system (798 K, 200 mV/s).

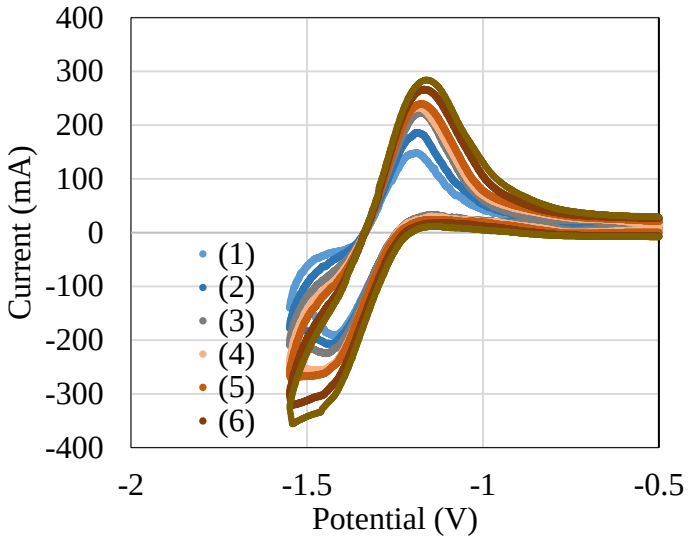

Figure 39. Subtraction CV curves for the LiCl-KCl-$CeCl_3$ (4 wt% $CeCl_3$) system at 773 K and scan rates: (1) 15, (2) 20, (3) 30, (4) 40, (5) 50, (6) 75, and (7) 100 mV/s.

Mass transport properties: Many studies have shown that the reduction of an electroactive species at a liquid bismuth cathode in LiCl-KCl salts is diffusion controlled. Therefore, the diffusion coefficient of a species in the LiCl-KCl salt is important for understanding the reduction behavior. CV can be performed at different scan rates to give a measurement of the diffusion coefficient (D) according to the Berzins-Delahay equation for a soluble-insoluble reversible process [52],

$$i_p = 0.611\, nFSC_0 \left(\frac{nF\upsilon D}{RT}\right)^{1/2} \quad \textbf{(1)}$$

where i_p is the peak cathodic current, n is the number of electrons transferred, S is the surface area of the cathode, F is the Faraday constant, R is the universal gas constant, T is the absolute temperature, C_0 is the concentration of the electroactive species in the salt (mol m^{-3}), and v is the scan rate. Plotting i_p vs. $v^{1/2}$ will give an experimental value for D which helps to understand the kinetics of the system. We have calculated values of the diffusion coefficient based on the small reduction peaks for the Sr, Cs, Ba, and Ce systems with a liquid Bi cathode. Calculated diffusion coefficient values for Ba are shown in Figure 40. We have also calculated and presented diffusion coefficient values for the two peaks observed in the Cs system, the Sr system, and the Ce system in our reports.

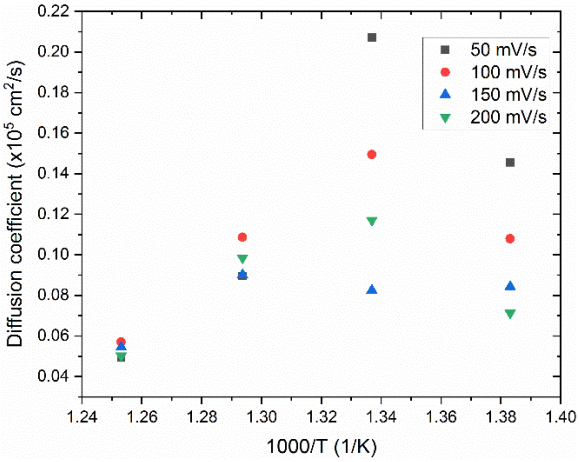

Figure 40. Calculated diffusion coefficients for LiCl-KCl-$BaCl_2$ (1.0 wt%) system.

Exchange current and charge transfer properties: From the CVs obtained for the systems, we have analyzed the data to get electrochemical properties values for the ionic species at the cathode. We have calculated values for the exchange current density (i_0) of the ionic species at the cathode via the Butler-Volmer equation for small overpotentials [53]. We have also performed EIS experiments to produce values of the exchange current densities of the ionic species at the Bi cathode surface in the systems. The equivalent circuit used to fit these data is shown in Figure 41 and calculated values of i_0 for the Ba^{2+}/Ba species (Figure 42).

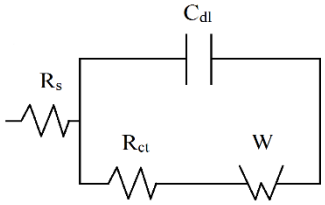

Figure 41. Equivalent circuit used to fit EIS data.

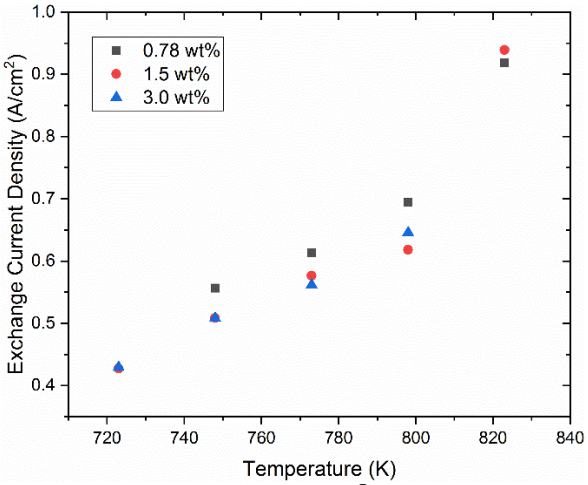

Figure 42. Calculated exchange current density of Ba^{2+}/Ba at Bi cathode at 773 K.

2.5 Thermal analysis of LiCl-KCl-$BaCl_2$ system

The thermal properties of the LiCl-KCl and $BaCl_2$ binary system have been studied to obtain phase transition temperatures. The liquidus line was measured to be between 652 K and 902

K for varying concentrations of $BaCl_2$ up to 60 wt%.

2.5.1 Experimental

Samples of $BaCl_2$-LiCl-KCl were prepared in an argon atmosphere glovebox. Salts were weighed and mixed to give a 10 g sample, which was then placed into an alumina crucible and dried in a Kerrlab Auto Electro Melt furnace for 5 hours at 573 K to remove any remaining moisture content. The salts were then melted at 773 K for 24 hours before being extracted by dipping a clean pyrex tube into the molten salt to obtain a salt disk inside the tube. Thermal analyzer (model: TGA-DSC Q600) was used to study the thermal transitions via a heat-flux technique, measuring the amount of heat required to increase the temperature of the sample versus a reference. Alumina pans were used to hold the salt sample and to act as the empty reference pan. Salt sample size and heating rate have significant effects on the shape of the DSC scan. A high heating rate enhances the instrumental sensitivity but decreases the resolution; that is, it results in thermograph peaks that are taller, but also broader. The mass of the DSC sample also has an effect on the heat flow measurement. Using small sample masses will achieve high resolution but poor sensitivity. In contrast, larger samples increase sensitivity but can also cause thermal lag due to heat transfer between the bulk material and the sensor. After testing several experiments with different sample sizes and heating rates, we decided upon the system of using a 10 mg sample and 5 °C min^{-1} heating rate.

2.5.2 Results

Detailed temperature values for observed peaks are listed in Table 20. Data for DSC experiments using the third experimental pattern.Table 20. The temperature values for the first and second peak were then plotted vs. weight fraction of $BaCl_2$ to construct a partial binary phase diagram of the $BaCl_2$ and LiCl-KCl system, as shown in Figure 43. The first peak temperatures represent values on the solidus line, below which the composition is completely crystalline. The second peak temperatures represent values on the liquidus line, above which the solution is completely liquid. The eutectic composition of the salt is seen to exist somewhere between 10 and 30 wt%. The importance of this study is a confirmation that $BaCl_2$ is fully liquid in the system at the temperatures of the electrochemical study. This DSC study has shown that at the low weight percentages used in the electrochemistry studies (1 to 4 wt%), the $BaCl_2$ might not be fully liquid at temperatures below 481 °C.

Table 20. Data for DSC experiments using the third experimental pattern.

Weight Percent $BaCl_2$ (wt%)	Weight (mg)	Heating Rate (°C/min)	Peak 1 temperature (°C)	Peak 2 temperature (°C)
1	8.2562	5	352.83	481.35
10	9.0789	5	346.21	441.44
20	9.0203	5	341.27	379.92
30	8.1955	5	343.41	429.66
40	13.916	5	337.46	469.64
50	9.8121	5	348.86	576.87

60	7.8963	2	344.52	629.81

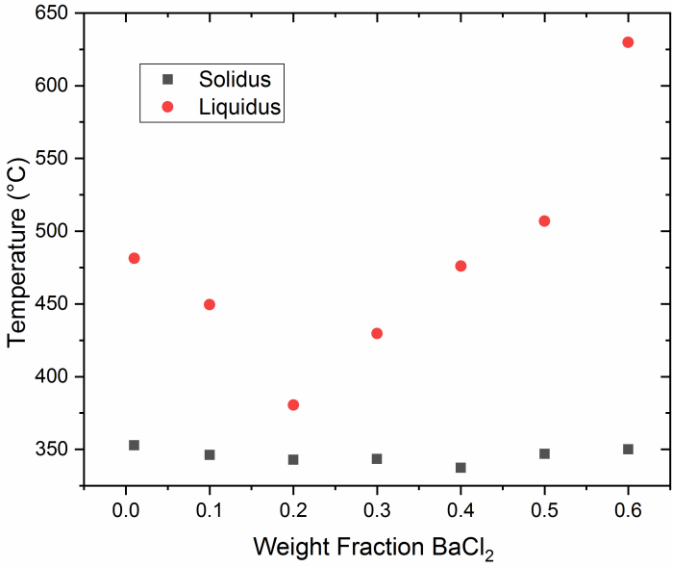

Figure 43. Binary phase diagram of $BaCl_2$ and LiCl-KCl salt system.

3. Conclusions

The presence of radioactive fission products such as ^{137}Cs and ^{90}Sr which oxidize from used nuclear fuels during the electrorefining process necessitates frequent disposal and replacement of the electrolyte, thereby increasing the amount of nuclear waste accumulating in on-site storage facilities without long-term contingency plans for disposal. The primary objective of this research project was to determine the viability of liquid metal electrodes for separating alkali/alkaline-earth elements from molten salt electrolytes with the intention of providing a route towards removing Ba and Sr from LiCl-KCl electrolyte. While an inert cathode will be unable to reduce Ba^{2+}/Sr^{2+} out of the electrolyte without first removing Li due to the order of the standard reduction potentials of the alkali/alkaline-earth elements in the chloride system, liquid metal electrodes (e.g. Bi, Sb, Sn) were able to shift the standard reduction potential of the alkali/alkaline-earths, possibly allowing preferential deposition out of LiCl-KCl-based molten salts.

In order to determine the effectiveness of Bi, Sb, and Pb at potentially altering the redox potential of Ba^{2+}/Ba and Sr^{2+}/Sr, electromotive force measurements were conducted for the Sr-Bi, Sr-Sb, Sr-Pb, Ba-Bi, and Ba-Sb binary systems to determine the strength of the atomic interactions between alkaline-earth and each of the liquid metals, i.e. the activity of alkaline earths in liquid metals (Bi, Sb, Pb). The electromotive force measurements concluded that Sr-Sb exhibits the strongest interactions with Sr (a_{Sr} as low as 1.5×10^{-12} at 988 K and $x_{Sr} = 0.04$), followed by Sr-Bi (a_{Sr} as low as 2.5×10^{-11} at 988 K and $x_{Sr} = 0.05$), and finally that Sr-Pb exhibits the weakest interactions with Sr (a_{Sr} as low as 7.6×10^{-10} at 950 K and $x_{Sr} = 0.05$).

Based on the measured thermodynamic properties in this work, Sb and Bi were predicted to be the most efficient liquid metal electrodes for removing Sr and Ba from molten chlorides. Additionally, Ba followed the same trend as Sr, with Ba-Sb having the strongest interactions (a_{Ba} as low as 2.0×10^{-15} at 923 K and $x_{Ba} = 0.05$) followed by Ba-Bi (a_{Ba} as low as 6.6×10^{-16} at 773 K and $x_{Sr} = 0.05$). The recovery of Sr and Ba was confirmed with deposition experiments in which constant current was applied between a liquid metal electrode and an inert graphite counter electrode in LiCl-KCl-$SrCl_2$-$BaCl_2$ molten salt. Post-mortem analysis via ICP-AES compositional analysis indicated significant presence of Sr (~6.5 mol%) and Ba (~12.8 mol%) in the Bi electrodes; however, reasonable amounts of Li were also deposited in the electrodes (~16.2 mol% in Bi). Despite the undesirable presence of Li, the substantial amount of Sr and Ba deposited in the liquid metals is encouraging.

Overall, the results indicate that the strong interactions between Sr/Ba and Bi/Sb can be leveraged to remove alkaline-earth fission products from molten salt electrolytes, providing a potential path towards reducing the volume of nuclear waste from electrorefining process.

Complete data sets for the Sr-Sn, Ba-Pb, and Ba-Sn sets were also collected with manuscripts for each in preparation. Preliminary experiments also indicate the Cs exhibits similar deposition behavior into liquid metals as Sr and Ba.

4. References

[1] Department of Energy, Nuclear Field Data Survey, U.S. Energy Inf. Assoc. (2013) For GC–859.

[2] HSC Chemistry 5.1, F. Outokumpu Oy, Finland, (2002).

[3] J. Bruno, R.C. Ewing, Spent nuclear fuel, Elements. (2006). doi:10.2113/gselements.2.6.343.

[4] H. Kim, N. Smith, K. Kumar, T. Lichtenstein, Electrochemical Separation of Barium into Liquid Bismuth by Controlling Deposition Potentials, Electrochim. Acta. (2016).

[5] H. Okamoto, Binary Alloy Phase Diagrams, II Edition, T.B. Massalski, ASM International, 1990.

[6] A.V. Vakhobov, Z.U. Niyazova, B.N. Polev, Phase diagram of the system Sr-Sb, Inorg. Mater. 11 (1975) 306–307.

[7] N.D. Smith, T. Lichtenstein, J. Gesualdi, K. Kumar, H. Kim, Electrochimica Acta Thermodynamic Properties of Strontium-Bismuth Alloys Determined by Electromotive Force Measurements, Electrochim. Acta. 225 (2017) 584–591. doi:10.1016/j.electacta.2016.12.051.

[8] H. Ipser, A. Mikula, I. Katayama, Overview: The emf method as a source of experimental thermodynamic data, Calphad Comput. Coupling Phase Diagrams Thermochem. (2010). doi:10.1016/j.calphad.2010.05.001.

[9] A. Bard, L. Faulkner, Electrochemical Methods: Fundamentals and Applications, 2nd ed., John Wiley and Sons, Hoboken, 2001.

[10] Y. Wang, J. Xin, C. Chen, S. Liu, B. Hu, Y. Du, Thermodynamic assessment of the Sr-In and Sr-Bi systems supported by first-principles calculations, Calphad Comput. Coupling Phase Diagrams Thermochem. (2014). doi:10.1016/j.calphad.2013.12.001.

[11] J. Delcet, R.J. Heus, J.J. Egan, Electronic Conductivity in Solid CaF at High Temperature, J. Solid State Chem. J. Appl. Electrochem. This J. J. Chim. Phys. J. Appl. Electrochem. J. Solid State Chem. J. Fouletier J. Solid State Chem. 125 (1976) 369–217.

[12] N.I. Sorokin, B.P. Sobolev, Solid-State Fluoride Electrolyte Review, Crystallogr. Reports. 52 (2007) 842–853.

[13] H. Kim, D.A. Boysen, D.J. Bradwell, B. Chung, K. Jiang, A.A. Tomaszowska, K. Wang, W. Wei, D.R. Sadoway, Thermodynamic properties of calcium–bismuth alloys determined by emf measurements, Electrochim. Acta. 60 (2011) 154–162. doi:10.1016/j.electacta.2011.11.023.

[14] S. Poizeau, H. Kim, J.M. Newhouse, B.L. Spatocco, D.R. Sadoway, Determination and modeling of the thermodynamic properties of liquid calcium-antimony alloys, Electrochim. Acta. (2012). doi:10.1016/j.electacta.2012.04.139.

[15] J.M. Newhouse, S. Poizeau, H. Kim, B.L. Spatocco, D.R. Sadoway, Thermodynamic properties of calcium-magnesium alloys determined by emf measurements, Electrochim. Acta. (2013). doi:10.1016/j.electacta.2012.11.063.

[16] J. Delcet, J.J. Egan, THERMODYNAMICS OF LIQUID Ca-Ag AND Ca-In ALLOYS, J. Less-Common Met. Elsevier Sequoia S.A. 59 (1978) 229–236.

[17] N.D. Smith, J. Soldan-Palma, N. Orabona, C. Marker, S.L. Shang, P. Guan, T. Lichtenstein, J. Gesualdi, T.P. Nigl, Z.K. Liu, H. Kim, Thermodynamic Properties of the Strontium-Antimony Binary System via Experimental and Computational Approaches,

Prep. (n.d.).
[18] T. Lichtenstein, J. Gesualdi, T.P. Nigl, C.T. Yu, H. Kim, Thermodynamic Properties of Barium-Antimony Alloys Determined by Emf Measurements (Accepted Manuscript), Electrochim. Acta. (2017).
[19] A. Petric, A.D. Pelton, M.L. Saboungi, Thermodynamic properties of liquid K-Bi alloys by electromotive force measurements, J. Phys. F Met. Phys. 18 (1988) 9–14. doi:10.1088/0305-4608/18/7/015.
[20] H. Zhang, C. Zhang, W.W. Wang, Y. Du, P. Zhou, B. Hu, Z. Liu, J.C. Wang, J. Wang, Thermodynamic assessment of the Pb-Sr system, J. Min. Metall. Sect. B Metall. 53 (2017) 179–187. doi:10.2298/JMMB170302013Z.
[21] J. Delcet, A. Delgado-Brune, J.J. Egan, Coulometric Titrations Using CaF2 and BaF2 Solid Electrolytes to Study Alloy Phases, in: Y.A. Chang, J.F. Smith (Eds.), Symp. Calc. Phase Diagrams Thermocehmistry Alloy Phases, Metallurgical Society of AIME, Milwaukee, 1979: pp. 275–287.
[22] A. Petric, A.D. Pelton, M.-L. Saboungi, Thermodynamic properties of liquid K-Bi alloys by electromotive force measurements, J. Phys. F Met. Phys. 18 (1988) 1473–1489.
[23] Haynes W. M., CRC Handbook of Chemistry and Physics, 97th Edition, 2017.
[24] J.O. Andersson, T. Helander, L. Hoglund, P.F. Shi, B. Sundman, Thermo-Calc and DICTRA, Computational tools for materials science, Calphad. 26 (2002) 273–312.
[25] G. Kresse, J. Furthmüller, Efficiency of ab-initio total energy calculations for metals and semiconductors using a plane-wave basis set, Comput. Mater. Sci. 6 (1996) 15–50.
[26] A. Jain, S.P. Ong, G. Hautier, W. Chen, W.D. Richards, S. Dacek, S. Cholia, D. Gunter, D. Skinner, G. Ceder, The Materials Project: A materials genome approach to accelerating materials innovation, Apl Mater. 1 (2013) 11002.
[27] Materials Project, (n.d.).
[28] G. Bergerhoff, R. Hundt, R. Sievers, I.D. Brown, The inorganic crystal structure data base, J. Chem. Inf. Comput. Sci. 23 (1983) 66–69.
[29] G. Bergerhoff, I.D. Brown, Inorganic Crystal Structure Database (FIZ Karlsruhe), (1978).
[30] W.M. Hurng, J.D. Corbett, Alkaline-Earth-Metal Antimonides and Bismuthides with the A5Pn3 Stoichiometry., 1. (1989) 311–319.
[31] B. Eisenmann, Sr2Sb3, eine Zintl-Phase mit Sb6-Kettenanion, Z. Naturforsch. B. 34 (1979) 1162–1164.
[32] K. Deller, B. Eisenmann, NEW INTERMETALLIC COMPOUND SRSB2, ZEITSCHRIFT FUR Naturforsch. Sect. BA J. Chem. Sci. 31 (1976) 1146–1147.
[33] A. Rehr, S.M. Kauzlarich, Sr11Sb10, Acta Crystallogr. 50 (1994) 1859–1861.
[34] A. Rehr, S.M. Kauzlarich, A New Modification of Sr5Sb3, Acta Crystallogr. 49 (1993) 1442–1444.
[35] M. Martinez Ripoll, A. Haase, G. Brauer, The Crystal Structure of Sr2Sb, Acta Crystallogr. 29 (1973) 1715–1717.
[36] E.A. Leon Escamilla, W.M. Hurng, E.S. Peterson, J.D. Corbett, Synthesis, Structure, and Properties of Ca16Sb11, a Complex Zintl Phase., Inorg. Chem. 36 (1997) 703–710.
[37] S.L. Shang, Y. Wang, D.E. Kim, Z.-K. Liu, First-principles thermodynamics from phonon and Debye model: Application to Ni and Ni3Al, Comput. Mater. Sci. 47 (2010) 1040–1048.
[38] G. Kresse, D. Joubert, From ultrasoft pseudopotentials to the projector augmented-wave method, Phys. Rev. B. 59 (1999) 1758–1775.

[39] P.E. Blöchl, Projector augmented-wave method, Phys. Rev. B. 50 (1994) 17953.
[40] K. Perdew, J. P., Ruzsinszky, A., Csonka, G. I., Vydrov, O. A., Scuseria, G. E., Constantin, L. A., Zhou, X. & Burke, Restoring the density-gradient expansion for exchange in solids and surfaces, Phys. Rev. Lett. 100 (2008) 136406.
[41] H.J. Monkhorst, J.D. Pack, Special points for Brillouin-zone integrations, Phys. Rev. B. 13 (1976) 5188–5192.
[42] O. Redlich, A.T. Kister, Algebraic representation of thermodynamic properties and the classification of solutions, Ind. Eng. Chem. 40 (1948) 345–348.
[43] A.T. Dinsdale, SGTE Data for Pure Elements, CALPHAD. 15 (1991) 317–425.
[44] T. Lichtenstein, N.D. Smith, J. Gesualdi, K. Kumar, H. Kim, Thermodynamic properties of Barium-Bismuth alloys determined by emf measurements, Electrochim. Acta. 228 (2017) 628–635. doi:10.1016/j.electacta.2016.12.141.
[45] R. Hultgren, P.D. Desai, D.T. Hawkins, M. Gleiser, K.K. Kelley, Selected values of the thermodynamic properties of binary alloys, National Standard Reference Data System, 1973.
[46] G. Grube, D. Dietrich, Electrical conductivity and phase diagrams of binary alloys, XXIV Alloy. Barium with Bismuth, Magnes. Lead. Z Elektrochem. 44 (1938) 755–767.
[47] N.N.Zhuravlev, E.M.Smirnova, Investigation of Alloys of the Bi-Ba and Bi-Sr Systems, Inorg.Mater. (1966) 654–656.
[48] C.W. Bale, E. Bélisle, P. Chartrand, S.A. Decterov, G. Eriksson, A.E. Gheribi, K. Hack, I.H. Jung, Y.B. Kang, J. Melançon, A.D. Pelton, S. Petersen, C. Robelin, J. Sangster, P. Spencer, M.A. Van Ende, FactSage thermochemical software and databases, 2010-2016, Calphad Comput. Coupling Phase Diagrams Thermochem. 54 (2016) 35–53. doi:10.1016/j.calphad.2016.05.002.
[49] W. Weppner, R.A. Huggins, Thermodynamic Properties of the Intermetallic Systems Lithium-Antimony and Lithium-Bismuth, 125 (1976).
[50] M. Matsumiya, M. Takano, R. Takagi, R. Fujita, Recovery of Ba2+ Using Liquid Metallic Cathodes in Molten Chlorides, J. Nucl. Sci. Technol. 35 (1998) 836–839. doi:10.1080/18811248.1998.9733952.
[51] Castrillejo Y., Bermejo M.R., Diaz Arocas P., de la Rosa F., Barrado E., Electrode Reaction of Cerium into Liquid Bismuth in the Eutectic LiCl-KCl, Electrochemistry, 73, 636-643. 2005.
[52] Delahay P. New Instrumental Methods in Electrochemistry: Theory, Instrumentation and Application to Analytical and Physical Chemistry, Interscience, New York. 1954.
[53] Yoon, D., Phongikaroon, S., & Zhang, J. Electrochemical and Thermodynamic Properties of CeCl3 on Liquid Cadmium Cathode (LCC) in LiCl-KCl Eutectic Salt, Journal of The Electrochemical Society, 163(3), E97–E103. 2016.

5. List of publications and presentations

5.1. Publications

(1) Hojong Kim, Nathan Smith, Kuldeep Kumar, Timothy Lichtenstein, "Electrochemical Separation of Barium into Liquid Bismuth by Controlling Deposition Potentials", Electrochimica Acta 220 (2016) 237-244.

(2) Nathan D. Smith, Timothy Lichtenstein, Jarrod Gesualdi, Kuldeep Kumar, Hojong Kim, "Thermodynamic Properties of Strontium-Bismuth Alloys Determined by Electromotive Force Measurements", Electrochimica Acta 225 (2017) 584-591.

(3) Timothy Lichtenstein, Nathan D. Smith, Jarrod Gesualdi, Kuldeep Kumar, Hojong Kim, "Thermodynamic properties of Barium-Bismuth alloys determined by emf measurements", Electrochimica Acta 228 (2017) 628-635.

(4) Timothy Lichtenstein, Jarrod Gesualdi, Thomas P. Nigl, Chen Ta Yu, Hojong Kim, "Thermodynamic Properties of Barium-Antimony Alloys Determined by Emf Measurements", Electrochimica Acta 251 (2017) 203-211.

(5) Thomas Nigl, Nathan D. Smith, Timothy Lichtenstein, Jarrod Gesualdi, Kuldeep Kumar, Hojong Kim, "Determination of Thermodynamic Properties of Alkaline Earth-Liquid Metal Alloys Using the Electromotive Force Technique", Journal of Visulaized Experiments 129 (2017) e56718.

(6) Timothy Lichtenstein, Thomas Nigl, Nathan D. Smith, Hojong Kim, "Electrochemical Deposition of Alkaline-Earth Elements (Sr and Ba) from LiCl-KCl-SrCl2-BaCl2 Solution Using a Liquid Bismuth Electrode", Electrochimica Acta 281 (2018) 810-815.

(7) Jinming Liu, Pin-Wen Guan, Cassie Marker, Nathan D. Smith, Nicole Orabona, Shun-Li Shang, Hojong Kim, Zi-Kui Liu, "First-principle calculations and thermodynamic modeling of the Ba-Bi system supported by X-ray diffraction measurements", Journal of Alloys and Compounds 771 (2019) 281-289.

(8) Thomas Nigl, Timothy Lichtenstein, Nathan D. Smith, Jarrod Gesualdi, Yuran Kong, Hojong Kim, “Thermodynamic properties of strontium-lead alloys determined by emf measurements, Journal of the Electrochemical Society, 165 (2018) H991-H998.

(9) J. Gesualdi, T. Lichtenstein, N. Smith, H. Kim, “Thermodynamic properties of barium-lead alloys determined by emf measurements”, In preparation, 2018.

(10) N. Smith, H. Kim, “Thermodynamic properties of barium-tin alloys determined by emf measurements”, In preparation, 2019.

(11) T. Lichtenstein, H. Kim, “Thermodynamic properties of strontium-tin alloys determined by emf measurements”, In preparation, 2019.

(12) Timothy Lichtenstein, “Recovery of alkaline-earth fission products into liquid metals: The influence of electrolyte composition and electrode kinetics”, In preparation, 2019.

(13) M. Woods, S. Phongikaroon, “Electrochemical Behavior of Ce^{3+}/Ce Couple on Liquid Bi Electrode in LiCl-KCl Eutectic”, In preparation, 2018.

(14) M. Woods, S. Phongikaroon, “Assessment of Liquid Bi for Electrochemical Separation of Sr, Cs, and Ba in LiCl-KCl”, In preparation, 2019.

5.2. Presentations and Posters

(1) H. Kim (Invited), "Electrochemical Separation of Alkali/Alkaline-earths (Ba, Sr, and Cs) from LiCl-KCl Electrolyte: Used Nuclear Fuel Recycling Process," Nuclear Engineering Colloquium, Mechanical and Nuclear Engineering, The Pennsylvania State University, University Park, PA, January 21, 2016.

(2) Hojong Kim (Invited), "Electrochemical Properties of alkali/alkaline-earth elements (Cs, Sr, and Ba) in liquid metals: Used Nuclear Fuel Recycling," Reactive Metal Processing Workshop (RMW11), MIT, Cambridge, MA, February 19, 2016.

(3) Michael Woods, "Electrochemical Properties and Analyses of $BaCl_2$ in LiCl-KCl Eutectic Salt," (Poster) ANS Student Conference, Madison, WI, April 2, 2016.

(4) Hojong Kim (Invited), "Separating Alkali/Alkaline-earths (Ba, Sr, and Cs) from Molten Salt Electrolytes Using Liquid Metal Electrodes", Nuclear Engineering Colloquium, The Virginia Commonwealth University, Richmond, VA, April 8, 2016.

(5) Hojong Kim, "Electrochemistry and Materials Science (Electrometallurgy) for Recycling Materials (Used Nuclear Fuel), Invited Lecture for Materials Engineering Methodology and Design (MATSE492W) Class, The Pennsylvania State University, University Park, PA, April 15, 2016.

(6) Hojong Kim, Nathan Smith, Timothy Lichtenstein, "Electrochemical deposition of Ba in liquid bismuth from BaCl2-LiCl-CaCl2-NaCl electrolyte", The 10th International Conference on Molten Slags, Fluxes, and Salts, Seattle, WA, May 25, 2016.

(7) Hojong Kim (Invited), "Electrochemistry and Materials Science for Sustainable Society: Closing Materials Cycle (Used Nuclear Fuels)", Invited Lecture for Research Experiences for Teachers (RET) Program, The Pennsylvania State University, University Park, PA, July 27, 2016.

(8) Hojong Kim, Nathan Smith, Timothy Lichtenstein, "Electrochemical separation of Ba from molten slat electrolyte using liquid bismuth electrode", International Pyroprocessing Research Conference (IPRC), Jeju Island, South Korea, September 21, 2016.

(9) Hojong Kim (Invited), "Materials Research based on Electrochemical Techniques and Methods: Corrosion, Energy Storage, and Separation (Recycling)", Invited Lecture for Undergraduate freshman seminar class (EMSC 100S), The Pennsylvania State University, University Park, PA, October 14th and 24th, 2016.

(10) Michael Woods, "Electrochemical Behavior of $BaCl_2$-LiCl-KCl on a Liquid Bismuth Cathode" Poster at ANS Winter Conference 2016, Las Vegas, NV, November 8th, 2016

(11) H. Kim, N. Smith, K. Kumar, and T. Lichtenstein, "Electrochemical deposition of Ba into liquid Bi from $BaCl_2$-LiCl-$CaCl_2$-NaCl electrolyte", TMS 2017 annual meeting, San Diego, CA, Mar. 1, 2017.

(12) T. Lichtenstein, N. Smith, and H. Kim, "Thermochemical Properties of Ba-Bi Alloys Determined by Electromotive Force Measurements", TMS 2017 annual meeting, San Diego, CA, Mar. 2, 2017.

(13) N. Smith, T. Lichtenstein, and H. Kim, "Thermodynamic Properties of Sr-Bi Alloys Determined by Electromotive Force Measurements", TMS 2017 annual meeting, San Diego, CA, Mar. 2, 2017.

(14) H. Kim (Invited), "Electrochemistry and Materials Science (Electrometallurgy) for Recycling Materials (Used Nuclear Fuel)", Invited lecture for undergraduate juniors in Materials Engineering Methodology and Design (MATSE492) class, The Pennsylvania State University, University Park, PA, April 21, 2017.

(15) N. Smith, T. Lichtenstein, J. Gesualdi, H. Kim, "Thermodynamic Properties of Sr-Bi and Sr-Sb Alloys for Electrochemical Separation of Strontium from Molten Salt Electrolyte", 41st Actinide Separations Conference, Argonne, IL, May 23, 2017.

(16) M. Woods, S. Phongikaroon, "Electrochemical Study of $BaCl_2$ and CsCl on a Liquid Bismuth Cathode in LiCl-KCl Eutectic Salt", ANS 2017 annual meeting, San Francisco, CA, June 14th, 2017.

(17) H. Kim (invited), "Electrochemistry for Materials Research from Fundamentals to Applications: Separation and recycling of used nuclear fuel", Ulsan National Institute of Science and Technology (UNIST), Chemical Engineering, Ulsan, South Korea, July 21, 2017.

(18) H. Kim (invited), "Thermodynamic Properties of Alkaline-earths (Ca, Ba, and Sr) in Liquid Metals (Bi and Sb) by Emf technique", High Temperature Batteries for Staionary Energy Storage Workshop, Trondheim, Norway, Sept 19, 2017.

(19) M. Woods (speaker), S. Phongikaroon, "Electrochemical Study of $BaCl_2$ and CsCl on Liquid Bismuth Cathode in LiCl-KCl Eutectic Salt," American Nuclear Society-Annual Meeting, San Francisco, CA, June 2017.

(20) M. Woods (speaker), S. Phongikaroon, "Electrochemical and Thermal Behavior of $BaCl_2$ on Liquid Bi Electrode in LiCl-KCl Melts," American Nuclear Society-Winter Meeting, Las Vegas, Nevada, November 2016.

(21) H. Kim, T. Lichtenstein, N. Smith, "Electrochemical Separation of Barium Ions from LiCl-KCl-$BaCl_2$ Electrolyte Using Liquid Bi and Sb", 232nd ECS Meeting, National Harbor, MD, October 2, 2017.

(22) T. Nigl, T. Lichtenstein, N. Smith, and H. Kim, "Thermodynamic Properties of Strontium-Lead Alloys Determined by Electromotive Force Measurements", 232nd ECS Meeting, National Harbor, MD, October 2, 2017.

(23) H. Kim, "Materials Research based on Electrochemical Techniques and Methods", Invited research seminar (EMSE100S) for undergraduate freshman in Materials Science and Engineering at the Pennsylvania State University, September 28, 2017.

(24) M. Woods, S. Phongikaroon, "Electrochemistry of $CeCl_3$-LiCl-KCl on a Liquid Bismuth Cathode", 2017 ANS Winter Meeting, Washington D.C., October 31, 2017.

(25) H. Kim, "Electrochemical Separation of Barium Ions from LiCl-KCl-$BaCl_2$ Electrolyte Using Liquid Bi and Sb", TMS annual meeting, Phoenix, AZ, March, 2018.

(26) J. Gesualdi, T. Lichtenstein, N. Smith, and H. Kim, "The thermodynamics of Barium-Lead Alloys", Reactive Metal Processing Workshop, Cambridge, MA, March, 2018.

(27) T. Lichtenstein, H. Kim, "Electrochemical Separation of Alkaline Earth Metals from LiCl-KCl Molten Salts", Reactive Metal Processing Workshop, Cambridge, MA, March, 2018.

(28) N. Smith and H. Kim. "Measurements of Thermodynamic Properties of Sr/Cs-Liquid Metal Alloys via the Electromotive Force Method", Reactive Metal Processing Workshop, Cambridge, MA, March, 2018.

(29) M. Woods, S. Phongikaroon, "Electrochemical Impedance Spectroscopy of Cs and Ba in LiCl-KCl/Liquid Bi", 2018 ANS Student Conference, Gainesville, FL, April 7th, 2018.

(30) H. Kim, T. Lichtenstein, N. Smith, "Electrochemical Deposition of alkaline-earth elements (Sr and Ba) into liquid metals in molten LiCl-KCl-$SrCl_2$-$BaCl_2$ salt", ECS annual meeting, Cancun, Mexico, Oct. 1, 2018.

(31) H. Kim, "Determining thermodynamic properties of alkaline-earths (Ba and Sr) in liquid metals by electromotive force measurements", MS&T, Columbus, OH, Oct. 16, 2018.

(32) M. Woods, S. Phongikaroon, "Electrochemical behavior of alkali/alkaline-earths on liquid Bi in LiCl-KCl eutectic salt", IPRC 2018, Tokai-Mura, Ibarki, Japan, Oct. 25, 2018.

(33) N. Smith, T. Nigl, H. Kim, “Electrochemical Separation of Cs from Molten Salts Using Liquid Metal Electrodes”, AIChE, Pittsburgh, PA, Oct. 30, 2018.

(34) T. Nigl, T. Lichtenstein, N. Smith, J. Gesualdi, Y. Kong, H. Kim, “Thermodynamic Properties of Strontium-Lead Alloys Determined by Electromotive Force Measurements”, AIChE, Pittsburgh, PA, Oct. 30, 2018.

(35) T. Lichtenstein, T. Nigl, N. Smith1, H. Kim, “Electrochemical deposition of Sr and Ba into liquid Bi in Molten Salt Electrolytes”, AIChE, Pittsburgh, PA, Oct. 30, 2018.

APPENDIX. Published Journal Articles

Electrochimica Acta 220 (2016) 237–244

Contents lists available at ScienceDirect

Electrochimica Acta

journal homepage: www.elsevier.com/locate/electacta

Electrochemical Separation of Barium into Liquid Bismuth by Controlling Deposition Potentials

Hojong Kim*, Nathan Smith, Kuldeep Kumar, Timothy Lichtenstein

Materials Science and Engineering, The Pennsylvania State University, 406 Steidle Building, University Park, PA 16802, United States

ARTICLE INFO

Article history:
Received 20 June 2016
Received in revised form 12 October 2016
Accepted 12 October 2016
Available online 13 October 2016

Keywords:
Electrochemical Separation
Liquid Electrode
Liquid Alloys
Molten Salt Electrolyte
Alkaline-earth separation
Liquid Bismuth
Barium

ABSTRACT

Electrochemical separation of barium from multi-component molten salt electrolyte ($BaCl_2$-LiCl-$CaCl_2$-NaCl) at 500–700 °C is demonstrated using a liquid bismuth electrode which possesses strong chemical interactions with barium. While the standard emf analysis suggests Na to be the first species to deposit in this electrolyte followed by Ca, Li, and finally Ba, barium was found to be the first species to be reduced into the bismuth electrode followed by Ca. The exceptional deposition behavior of barium was ascribed to the activity of the constituent alkali/alkaline-earth metals in the bismuth metal. The activity of barium in bismuth was extremely low (as low as 10^{-15}), shifting the redox potential of barium to the most positive potentials and enabling the separation of barium into liquid bismuth. By exploiting the differential interactions of constituent ions with the liquid bismuth, it was possible to separate conventionally non-separable barium species from the electrolyte solution. In addition, high coulombic efficiencies of the liquid bismuth electrode (>99%) suggest that electrode processes are chemically reversible for co-deposition of barium and calcium. The analyses of electrode potentials at various current densities and electrochemical impedance spectra indicate charge transfer as the most significant overpotential mechanism during electrolysis.

1. INTRODUCTION

Alkali/alkaline-earth metals are highly reactive, characterized by low standard electrode potentials, and their halides are often employed as constituents of a supporting electrolyte (as non-electroactive ions). According to the standard electrode potentials of alkali/alkaline-earth elements in the chloride system at 600 °C (Fig. 1)[1], one would expect barium metal to deposit last from a solution of alkali/alkaline-earth metal chlorides as it has the highest stability in the electrolyte, indicated by its redox potential ($E^0_{Ba^{2+}/Ba} = -3.74$ V vs. $Cl^-/Cl_2(g)$). In other words, barium is one of the most challenging species to separate from the electrolyte solution electrochemically.

While the reduction of the most stable species in the electrolyte (e.g., Ba^{2+} in the chloride system) is not feasible based upon the analysis of standard electrode potentials, we will demonstrate the feasibility of separating these stable species using liquid metal electrodes that possess preferential, strong chemical interactions with these elements. More specifically, we will present unusual deposition behavior of barium into liquid bismuth electrodes ($T_{m,Bi}$ = 271 °C) from the multi-component $BaCl_2$-LiCl-$CaCl_2$-NaCl (16-29-35-20 mol%) electrolyte, based upon the thermodynamic analysis of electrode reactions at 500–700 °C. This finding is believed to occur due to the strong interaction between liquid bismuth and barium metals, switching the sequence of deposition potentials of the constituent ions.

This study also suggests that the use of strongly interacting liquid metals enables us to separate out the most stable ionic species from electrolyte solutions, providing a direct methodology to purify electrolyte solutions contaminated with stable alkali/alkaline-earth elements in electrochemical refining or separation processes. For example, in electrochemical separation of uranium from used nuclear fuels in molten salt electrolytes (e.g., LiCl-KCl), a periodic replacement of electrolyte solution is required due to the accumulation of the alkali/alkaline-earth elements (e.g., Ba^{2+}, Cs^+, or Sr^{2+}) that changes the physical and chemical properties of the electrolyte thereby generating an excessive volume of nuclear waste [2,3]. The liquid metal electrodes can separate these conventionally non-separable alkali/alkaline-earth elements from the electrolyte solution, enabling direct purification and recycling of electrolytes, as well as reduction in the volume of nuclear waste.

* Corresponding author.
E-mail addresses: huk29@psu.edu, metaldep@gmail.com (H. Kim), nds174@psu.edu (N. Smith), kxk1023@psu.edu (K. Kumar), tvl5297@psu.edu (T. Lichtenstein).

http://dx.doi.org/10.1016/j.electacta.2016.10.083
0013-4686/

Video Article

Determination of Thermodynamic Properties of Alkaline Earth-liquid Metal Alloys Using the Electromotive Force Technique

Thomas P. Nigl[1], Nathan D. Smith[1], Timothy Lichtenstein[1], Jarrod Gesualdi[1], Kuldeep Kumar[1], Hojong Kim[1]

[1]Department of Materials Science and Engineering, The Pennsylvania State University

Correspondence to: Hojong Kim at huk29@psu.edu

URL: https://www.jove.com/video/56718
DOI: doi:10.3791/56718

Keywords: Chemistry, Issue 129, Electromotive force, thermodynamic properties, alkaline-earth alloys, electrochemical separation, binary alloys, electromotive force method

Date Published: 11/3/2017

Citation: Nigl, T.P., Smith, N.D., Lichtenstein, T., Gesualdi, J., Kumar, K., Kim, H. Determination of Thermodynamic Properties of Alkaline Earth-liquid Metal Alloys Using the Electromotive Force Technique. *J. Vis. Exp.* (129), e56718, doi:10.3791/56718 (2017).

Abstract

A novel electrochemical cell based on a CaF_2 solid-state electrolyte has been developed to measure the electromotive force (emf) of binary alkaline earth-liquid metal alloys as functions of both composition and temperature in order to acquire thermodynamic data. The cell consists of a chemically stable solid-state CaF_2-AF_2 electrolyte (where A is the alkaline-earth element such as Ca, Sr, or Ba), with binary A-B alloy (where B is the liquid metal such as Bi or Sb) working electrodes, and a pure A metal reference electrode. Emf data are collected over a temperature range of 723 K to 1,123 K in 25 K increments for multiple alloy compositions per experiment and the results are analyzed to yield activity values, phase transition temperatures, and partial molar entropies/enthalpies for each composition.

Video Link

The video component of this article can be found at https://www.jove.com/video/56718/

Introduction

Electromotive force (emf) measurements can directly determine the partial molar Gibbs free energy change of a chemical reaction and provide accurate thermodynamic properties such as activity, partial molar enthalpy, and partial molar entropy[1]. The acquisition of thermochemical data is crucial to a variety of research topics in the materials community, from the refinement of multi-component phase diagrams, to the experimental validation of first-principle materials modeling, to the synthesis of new intermetallic species with advantageous properties. Recently, Kim *et al.* utilized emf measurements to assess the viability of using liquid metal electrodes to separate alkaline-earth species from molten salt electrolytes[2].

Electrochemical separation using molten salts (*e.g.*, LiCl-KCl) is a promising technology for separating uranium and transuranic metals from used nuclear fuel for recycling[3]. As used fuel is processed as an anode in the molten salt, fission products with lower standard reduction potentials than uranium are oxidized and accumulate in the molten salt as dissolved ions (e.g., Ba^{2+}, Sr^{2+}, Cs^{+}, and rare-earth metal cations)[4]. Consequently, the molten salt electrolyte must be periodically replaced and/or processed further to separate the accumulated fission products[4]. Of particular concern are alkali/alkaline-earth fission products (Ba^{2+}, Sr^{2+}, and Cs^{+}) because these ions exhibit the lowest standard reduction potentials among the constituent cations, making them difficult to separate from the molten salt solution.

However, Lichtenstein *et al.* recently demonstrated that barium exhibits low thermodynamic activity in liquid bismuth (8.7×10^{-12} at barium mole fraction $x_{Ba(in\ Bi)}$ = 0.05, 1,123 K), implying strong atomic interactions between barium and bismuth[5]. Kim *et al.* observed that these interactions caused a shift in the deposition potentials of barium ions into a liquid bismuth electrode (-3.74 V to -2.49 V vs. $Cl^{-}/Cl_2(g)$), resulting in a preferential deposition of barium from the electrolyte solution ($BaCl_2$-LiCl-$CaCl_2$-NaCl, 16-29-35-20 mol%) at 773 - 973 K[6]. This shift in deposition potential could be leveraged by using liquid metal electrodes to selectively separate alkali/alkaline-earth fission products from the electrolyte used for electrochemical processing of used nuclear fuel. To determine the viability of separating alkali/alkaline-earth fission products from molten salt electrolyte, the thermodynamic properties of these elements in the prospective liquid metals (*e.g.*, Bi, Sb) must be determined.

In previous studies, Delcet *et al.* utilized coulometric titration to determine the thermodynamic properties of binary alloys (*e.g.*, Ba-Bi, Ba-Sb, Ba-Pb)[7]. For Ba-Bi alloys up to x_{Ba} = 0.50, they employed coulometric titration using a single-crystal BaF_2 electrolyte at 1,123 K and observed comparable activity values of barium in bismuth (2.4×10^{-12} at $x_{Ba(in\ Bi)}$ = 0.05, 1,123 K). However, it was reported that the results were inaccurate due to the uncertainty regarding barium content in the binary alloys. Barium metal is highly reactive and soluble in its halide salts (~15 mol % in $BaCl_2$ at 1,163 K), which can cause increased electronic conduction in the halide salt at higher temperatures and lead to inaccurate compositional accounting during coulometric titration. To determine the thermodynamic properties (*e.g.*, excess partial molar Gibbs free energy, partial molar enthalpy, partial molar entropy) of binary alloys containing highly reactive elements, the emf method described in this protocol was used.

Electrochimica Acta 228 (2017) 628–635

Contents lists available at ScienceDirect

Electrochimica Acta

journal homepage: www.elsevier.com/locate/electacta

Thermodynamic properties of Barium-Bismuth alloys determined by emf measurements

Timothy Lichtenstein, Nathan D. Smith, Jarrod Gesualdi, Kuldeep Kumar, Hojong Kim*

Materials Science and Engineering, The Pennsylvania State University, 406 Steidle Building, University Park, PA 16802, United States

ARTICLE INFO

Article history:
Received 9 December 2016
Received in revised form 23 December 2016
Accepted 23 December 2016
Available online 26 December 2016

Keywords:
Barium-Bismuth alloys
Emf method
Thermodynamic properties
Barium-Bismuth phase diagram

ABSTRACT

Thermodynamic properties of Ba-Bi alloys, including the activity, partial molar entropy and enthalpy, were determined using the electromotive force (emf) technique for fourteen compositions, x_{Ba} = 0.05–0.80. Emf measurements were performed at ambient pressure using a Ba(s)|CaF_2-BaF_2|Ba(in Bi) or Ba-Bi (x_{Ba} = 0.05)|CaF_2-BaF_2|Ba(in Bi) electrochemical cells at 723–1073 K. At 773 K, activity values of Ba were as low as 6.6×10^{-16} at mole fraction x_{Ba} = 0.05 and approached unity for mole fractions $x_{Ba} \geq 0.80$. Stable emf values were observed at mole fractions x_{Ba} = 0.05–0.25, exhibiting less than a 5 mV difference between the heating and cooling cycles. Mole fractions $x_{Ba} \geq 0.30$ exhibited increased hysteresis or had an unexpected emf profile due to the formation of metastable phases such as Bi and Ba_5Bi_3, confirmed by X-ray diffraction. The Ba-Bi alloys were further characterized using differential scanning calorimetry over the entire composition range. Based on these data, a revised Ba-Bi binary phase diagram is proposed.

1. Introduction

Thermochemical properties of binary Ba-Bi alloys were investigated using the electromotive force (emf) technique to assess the viability of Bi electrodes in separating Ba species from molten salt electrolytes. Recently, Kim et al. investigated the electrochemical properties of bismuth electrodes in a $BaCl_2$-LiCl-$CaCl_2$-NaCl (16-29-35-20 mol%) electrolyte at 773–973 K. They identified Ba to be preferentially deposited over Na, Ca or Li due to Ba having the strongest atomic interactions with Bi, i.e. the lowest thermodynamic activity values of Ba in the Bi metal among alkali/alkaline-earth constituents [1,2].

Delcet et al. determined the thermodynamic properties of Ba-Bi alloys up to x_{Ba} = 0.50 by coulometric titration using a single-crystal BaF_2 electrolyte at 1123 K. The activity values of Ba in Bi were as low as 2×10^{-12} at x_{Ba} = 0.05; however, they reported that the results were not accurate due to uncertainty in Ba compositions (up to 3 mol%) during the coulometric titration [3]. Pure Ba metal is highly reactive and well known to have a high solubility in its own halide salts (e.g., ~15 mol% in $BaCl_2$ at 1163 K) [4]; barium metal dissolved in the halide electrolyte can promote electronic conduction through the electrolyte and prevent accurate compositional accounting by coulometric titration using halide electrolytes.

In this work, a solid-state binary CaF_2-BaF_2 (97-3 mol%) electrolyte was employed to determine the emf values of Ba-Bi alloys at fixed compositions over 723–1073 K. In the binary CaF_2-BaF_2 system, CaF_2 is more stable than BaF_2 due to having a more negative potential versus the F^-/F_2 redox couple, implying barium ions are the more electroactive species in the CaF_2-BaF_2 electrolyte. For example, at 800 K the standard electrode potential is −5.65 V for Ca^{2+}/Ca and −5.58 V for Ba^{2+}/Ba, calculated using the Nernst equation and the standard free energies of formation for CaF_2 and BaF_2 [5]. Utilizing the relatively high ionic conductivity of CaF_2 (~1.5×10^{-3} S cm^{-1} at 1073 K) [6] and higher stability than pure BaF_2, the binary CaF_2-BaF_2 electrolyte will allow for accurate emf measurements of Ba-Bi alloys using the electrochemical cell:

Ba(s)|CaF_2–BaF_2|Ba(in Bi) (1)

where pure Ba is the reference electrode (RE), solid CaF_2-BaF_2 is the electrolyte, and Ba-Bi alloys are the working electrodes (WE). Considering that CaF_2-BaF_2 is a fluoride-ion conducting electrolyte [6], the half-cell reactions are

WE: $BaF_2(s) + 2e^- = Ba(\text{in Bi}) + 2F^-$ (2)

RE: $BaF_2(s) + 2e^- = Ba(s) + 2F^-$ (3)

and the overall cell reaction is

Overall: $Ba(s) = Ba(\text{in Bi})$. (4)

* Corresponding author. Tel.: 814-865-3117, Fax: 814-865-2917.
E-mail addresses: tvl5297@psu.edu (T. Lichtenstein), nds174@psu.edu (N.D. Smith), jqg5465@psu.edu (J. Gesualdi), kxk1023@psu.edu (K. Kumar), huk29@psu.edu, metaldep@gmail.com (H. Kim).

http://dx.doi.org/10.1016/j.electacta.2016.12.141
0013-4686/

Electrochimica Acta 251 (2017) 203–211

Contents lists available at ScienceDirect

Electrochimica Acta

journal homepage: www.elsevier.com/locate/electacta

Thermodynamic Properties of Barium-Antimony Alloys Determined by Emf Measurements

Timothy Lichtenstein, Jarrod Gesualdi, Thomas P. Nigl, Chen Ta Yu, Hojong Kim*

Materials Science and Engineering, The Pennsylvania State University, 406 Steidle Building, University Park, PA 16802, United States

ARTICLE INFO

Article history:
Received 5 July 2017
Received in revised form 18 July 2017
Accepted 19 July 2017
Available online 22 July 2017

Keywords:
Barium-antimony alloys
Emf method
Ba-Sb phase diagram
Thermodynamic properties

ABSTRACT

The thermodynamic properties of Ba-Sb alloys, including the activity, partial molar entropy, and partial molar enthalpy, were determined using the electromotive force (emf) technique for thirteen compositions spanning the composition range of x_{Ba} = 0.03–0.77. Emf measurements were performed at ambient pressure under an inert argon atmosphere using a Ba-Bi(x_{Ba} = 0.05)|CaF_2-BaF_2|Ba(in Sb) electrochemical cell at 723–1073 K. At 923 K, activity values of Ba in Sb were as low as 2.0×10^{-15} at mole fraction x_{Ba} = 0.05 and approached unity for mole fractions $x_{Ba} \geq 0.77$. Phase characterization using X-ray diffraction (XRD) was performed on compositions of x_{Ba} = 0.03–0.77 and thermal characterization was performed on compositions up to x_{Ba} = 0.40 using differential scanning calorimetry (DSC). Integrating the results from emf, XRD, and DSC measurements, an experimentally determined Ba-Sb phase diagram was constructed.

1. Introduction

Electrochemical processing using molten salt electrolytes (e.g. LiCl-KCl) is a promising technology for closing the nuclear fuel cycle by separating uranium and transuranic metals from used nuclear fuels for recycling. The electrochemical separation process operates by oxidizing a metallic used fuel anode and preferentially reducing the uranium metal onto an inert cathode. In this process, alkali/alkaline-earth fission products (e.g. Ba, Cs, and Sr) in the metallic anode tend to preferentially oxidize and accumulate in the electrolyte as dissolved ions, as these elements are electrochemically more active than uranium [1–3]. For this reason, it is necessary to separate the dissolved alkali/alkaline-earth fission products from the molten salt electrolyte to minimize the volume of nuclear waste generated.

Recent work by Kim et al. demonstrated the feasibility of separating barium ions from $BaCl_2$-LiCl-$CaCl_2$-NaCl (16-29-35-20 mol%) electrolyte by electrochemical co-deposition of barium and calcium into liquid bismuth metal at 773–973 K [4]. The deposition of the conventionally more stable barium ions into liquid bismuth was attributed to the extremely low thermodynamic activity of barium in liquid Bi relative to the other alkali/alkaline-earth constituents. In a separate study, they determined the thermodynamic activity of barium in liquid bismuth to be as low as 6.6×10^{-16} at barium mole fraction $x_{Ba(inBi)}$ = 0.05 and 773 K, implying strong atomic interactions between barium and liquid bismuth [5]. Such a low activity alters the reduction potential of barium, making deposition occur at more positive potentials relative to the Ba^{2+}/Ba redox couple and enabling preferential deposition of barium into liquid bismuth. This prior work suggests that the separation of barium ions from molten salt electrolytes is possible by exploiting electrode materials that strongly interact with barium.

Compared to bismuth, antimony exhibits stronger chemical interactions with typical alkali/alkaline-earth elements (e.g. Li and Ca) [5–7]. For example, the activity of calcium is 1.2×10^{-11} in liquid antimony and 2.8×10^{-10} in liquid bismuth, both at calcium mole fraction x_{Ca} = 0.05 and 973 K [7,8]. Assuming a similar trend is found for barium, antimony will shift the deposition potentials of barium more positive than bismuth and may serve as an additional electrode system that can effectively separate the alkaline-earth ions from molten salt electrolytes. In order to assess the utility of antimony as a separation medium for Ba, this work investigates the thermodynamic properties of the Ba-Sb system.

* Corresponding author.
E-mail addresses: tvl5297@psu.edu (T. Lichtenstein), jqg5465@psu.edu (J. Gesualdi), tpn6@psu.edu (T.P. Nigl), cxy18@psu.edu (C.T. Yu), huk29@psu.edu, metaldep@gmail.com (H. Kim).

http://dx.doi.org/10.1016/j.electacta.2017.07.113
0013-4686/

Electrochimica Acta 225 (2017) 584–591

Contents lists available at ScienceDirect

Electrochimica Acta

journal homepage: www.elsevier.com/locate/electacta

Thermodynamic Properties of Strontium-Bismuth Alloys Determined by Electromotive Force Measurements

Nathan D. Smith, Timothy Lichtenstein, Jarrod Gesualdi, Kuldeep Kumar, Hojong Kim*

Materials Science and Engineering, The Pennsylvania State University, 406 Steidle Building, University Park, PA 16802, United States

ARTICLE INFO

Article history:
Received 20 November 2016
Accepted 8 December 2016
Available online 9 December 2016

Keywords:
Strontium-bismuth alloys
Emf method
Sr-Bi phase diagram
Thermodynamic properties

ABSTRACT

The thermodynamic properties of Sr-Bi alloys were determined by electromotive force (emf) measurements to evaluate the viability of liquid bismuth metal as a medium for separating alkali/alkaline-earth fission products from molten salt electrolyte. A Sr(s)|CaF_2-SrF_2|Sr(in Bi) cell was used to measure emf values at 748–1023 K for thirteen Sr-Bi alloys at mole fractions $0.05 \leq x_{Sr} \leq 0.75$. Activity values of strontium in bismuth were determined at 788 K, 888 K, and 988 K as well as the partial molar entropy and enthalpy at each composition. Reproducible emf values within ± 5 mV were obtained up to $x_{Sr} = 0.35$ during cooling-heating cycle. At higher mole fractions ($x_{Sr} \geq 0.40$), the emf values exhibited increased hysteresis during the thermal cycles due to the strong tendency of the alloys to form metastable phases. The non-equilibrium phase behavior of Sr-Bi alloys was verified by X-ray diffraction (XRD), differential scanning calorimetry (DSC), and microstructural analyses. Compared to the existing equilibrium phase diagram, two additional phases of Sr_2Bi_3 and Sr_4Bi_3 were identified and discussed. Liquid-state solubility of Sr was 15–40 mol% at 788–988 K and the activity values were as low as 10^{-13} at 788 K, implying strong chemical interactions between Sr and Bi.

1. Introduction

Electrochemical separation using molten salt electrolytes (e.g., LiCl-KCl) is currently one of the most promising techniques for separating uranium and transuranics from metallic used nuclear fuels [1]. However, the process has the inevitable consequence of accumulating alkali/alkaline-earth fission products in the molten salt electrolyte because alkali/alkaline-earth metals (Ba, Sr, and Cs) have the strongest tendency to oxidize during electrolysis. Periodic replacement of the electrolyte containing these fission products results in chloride wastes that can limit the development of a ceramic wasteform for long-term disposal and increase the volume of nuclear waste [2]. In addition, the alkali/alkaline fission products Sr and Cs pose serious environmental challenges as they have short half-lives (around 30 years) and high heat densities [3]. In our previous work, the separation of barium from quaternary $BaCl_2$-LiCl-$CaCl_2$-NaCl (16-29-35-20 mol%) electrolyte was achieved due to the extremely low thermodynamic activity of Ba in the liquid Bi electrode compared to Li, Ca, and Na, implying strong atomic interactions between Ba and Bi [4]. In efforts to separate radiotoxic Sr species from molten salt electrolyte, the thermodynamic properties of Sr-Bi alloys at 748–1023 K were examined using electromotive force (emf) techniques to evaluate the viability of using liquid bismuth electrodes for the separation of Sr.

Constructing an electrochemical cell to effectively measure emf values for Sr-Bi alloys can be technically challenging due to (i) the high reactivity of pure Sr as well as Sr-Bi alloys which can degrade the electrolyte or cell components during emf measurements, and (ii) the high melting temperatures of pure Sr ($T_{m,Sr}$ = 1042 K) and Sr-Bi alloys ($T_{liquidus}$ up to 1218 K) [5]. In recent studies, solid-state CaF_2 electrolyte has been utilized in determining the thermodynamic properties of Ca-Bi, Ca-Sb, and Ca-Mg alloys at 723–1100 K [6–8], employing the high stability of CaF_2 electrolyte in emf measurements of calcium alloys. Delcet and Egan also determined the emf values of Ca-Ag and Ca-In alloys using single-crystal CaF_2 at 1073 K via coulometric titration techniques and derived thermodynamic activity values of calcium [9]. The solid-state CaF_2 is well known to have substantial ionic conductivity (1.5×10^{-3} S cm^{-1} at 1073 K), suitable for emf measurements [10,11].

In the present study, the investigation of Sr-Bi alloys required using CaF_2-SrF_2 (97-3 mol%) instead of the pure CaF_2 electrolyte to account for the change in electroactive species. According to the

* Corresponding author.
E-mail addresses: nds174@psu.edu (N.D. Smith), tvl5297@psu.edu (T. Lichtenstein), jqg5465@psu.edu (J. Gesualdi), kxk1023@psu.edu (K. Kumar), metaldep@gmail.com, huk29@psu.edu (H. Kim).

http://dx.doi.org/10.1016/j.electacta.2016.12.051
0013-4686/

Electrochimica Acta 281 (2018) 810–815

Contents lists available at ScienceDirect

Electrochimica Acta

journal homepage: www.elsevier.com/locate/electacta

Electrochemical deposition of alkaline-earth elements (Sr and Ba) from LiCl-KCl-$SrCl_2$-$BaCl_2$ solution using a liquid bismuth electrode

Timothy Lichtenstein, Thomas P. Nigl, Nathan D. Smith, Hojong Kim*

Materials Science and Engineering, The Pennsylvania State University, 406 Steidle Building, University Park, PA 16802, United States

ARTICLE INFO

Article history:
Received 27 March 2018
Received in revised form
13 May 2018
Accepted 14 May 2018
Available online 17 May 2018

Keywords:
Liquid metal electrode
Molten salt electrolyte
Alkaline-earth separation
Used nuclear fuel recycling
Bismuth

ABSTRACT

Electrochemical deposition of Sr and Ba into liquid Bi metal was investigated in LiCl-KCl-$SrCl_2$-$BaCl_2$ electrolytes at 500 °C as a means to separate stable alkaline-earth ions from the molten salts (eutectic LiCl-KCl) utilized for recycling used nuclear fuel, by leveraging the strong chemical interactions between alkaline-earth metals and liquid Bi. The liquid Bi electrodes were subjected to cathodic discharge up to 270 C g^{-1} at a constant current density of 50 mA cm^{-2} in eutectic LiCl-KCl with the addition of 5 mol% total of $SrCl_2$ and/or $BaCl_2$. The use of Bi resulted in complex electrode reactions, leading to co-deposition of Sr (2.0–6.5 mol%), Ba (4.1–12.8 mol%), and Li (5.9–16.2 mol%), and coulombic efficiencies of 63–67% were achieved. The observed co-deposition was also supported via thermodynamic analyses of electrode potentials by incorporating the experimentally determined activity values of each alkali/alkaline-earth metal in Bi. The results of this work suggest that alkaline-earth fission products accumulated in molten salts (Sr^{2+} and Ba^{2+}) can be recovered into liquid Bi by electrochemical separation, which could be employed as a critical step for recycling the process salt (LiCl-KCl) in order to minimize the generation of additional nuclear wastes.

1. Introduction

Electrochemical deposition of alkaline-earth metals (Sr and Ba) into liquid Bi was investigated in order to separate alkaline-earth ions (Sr^{2+} and Ba^{2+}) from molten LiCl-KCl-$SrCl_2$-$BaCl_2$ solutions at 500 °C (Fig. 1). In molten LiCl-KCl-$SrCl_2$-$BaCl_2$ electrolytes, lithium ions are the least thermodynamically stable based upon the free energies of formation for pure chloride compounds [1], suggesting that the deposition of Li metal is the dominant cathodic reaction at an inert electrode and that the deposition of Sr or Ba is thermodynamically less favorable. Considering the higher stability of Sr and Ba ions relative to the Li ions in the chloride system, it would seem impractical to separate Sr and Ba from the molten chloride solutions by electrochemical means; however, our work indicates that the deposition of Sr and Ba into liquid Bi becomes thermodynamically feasible by leveraging the strong chemical interactions between alkali/alkaline-earth metals and liquid Bi.

Molten salts are widely employed in electrochemical processes for production of reactive metals and alloys (e.g., Na metal from $CaCl_2$-NaCl and Al metal from NaF-AlF_3) at elevated temperatures [2,3]. In the nuclear industry, an electrorefining process using molten salts (e.g., LiCl-KCl eutectic) was developed to separate uranium from used nuclear fuel for recycling and reduction of nuclear waste [4–6]. During electrorefining, more active fission products than uranium (e.g., Sr, Ba, Cs, and rare-earth metals) in the used nuclear fuel anode are oxidized and accumulate in the molten salt as dissolved ions [7]. In order for the process salt (LiCl-KCl) to be reused, the accumulated fission products in the salt must be removed, including ^{90}Sr which results in costly thermal management in long-term storage due to a relatively short half-life (~30 years) and a high heat density [4,8]. The deposition of Sr and Ba into liquid Bi in this work could be utilized to separate stable alkaline-earth fission products to enhance recycling of the process salts and minimize the generation of additional nuclear wastes.

Matsumiya et al. investigated the feasibility of using liquid Bi metal for electrochemically separating Sr ions from molten KCl-$SrCl_2$ at 723 °C and Ba ions from NaCl-KCl-$BaCl_2$ at 800 °C by constant-current electrolysis (−226 mA cm^{-2}) and cyclic voltammetry. They concluded that the recovery of Sr and Ba into liquid Bi was not feasible based on minimal contents of Sr and Ba recovered in the liquid Bi cathodes (<0.1 ppm) after coulombic discharge at 72 C g^{-1} and relatively high activity coefficients of alkaline-earths

* Corresponding author.
E-mail addresses: tvl5297@psu.edu (T. Lichtenstein), tpn6@psu.edu (T.P. Nigl), nds174@psu.edu (N.D. Smith), huk29@psu.edu (H. Kim).

https://doi.org/10.1016/j.electacta.2018.05.097
0013-4686/

Thermodynamic Properties of Strontium-Lead Alloys Determined by Electromotive Force Measurements

Thomas P. Nigl, Timothy Lichtenstein, Nathan D. Smith, Jarrod Gesualdi, Yuran Kong, and Hojong Kim[z]

Materials Science and Engineering, The Pennsylvania State University, University Park, Pennsylvania 16802, USA

The thermodynamic properties of Sr-Pb alloys were determined by electromotive force (emf) measurements. A Sr(s)|CaF_2-SrF_2|Sr(in Pb) electrochemical cell was used to measure emf values at 773–1073 K for Sr-Pb alloys at mole fractions $x_{Sr} = 0.07$–0.59. These emf measurements were used to determine thermodynamic properties of Sr-Pb alloys, including activity, partial molar entropy, and partial molar enthalpy. At 873 K, activity values of Sr in Pb were as low as $a_{Sr} = 1.72 \times 10^{-9}$ at mole fraction $x_{Sr} = 0.07$, implying strong atomic interactions between Sr and Pb. Phase transition temperatures of Sr-Pb alloys, observed during emf measurements, were corroborated by thermal analysis ($0.07 \leq x_{Sr} \leq 0.34$) by differential scanning calorimetry (DSC), and the phase constituents of Sr-Pb alloys ($0.07 \leq x_{Sr} \leq 0.75$) were characterized using X-ray diffraction (XRD). Experimentally-determined thermodynamic properties were compared to the assessed thermodynamic properties of the Sr-Pb system, confirming the phase transition temperatures and highlighting discrepancies in solution properties (activity and excess Gibbs energy).

 [DOI: 10.1149/2.1091814jes]

Manuscript submitted August 9, 2018; revised manuscript received October 23, 2018. Published November 10, 2018.

Electrochemical separation of uranium from used nuclear fuel in molten salt electrolytes (e.g. LiCl-KCl eutectic) is a promising recycling technique to close the nuclear fuel cycle via electrorefining processes where the uranium metal is deposited at the cathode for recycling and the metallic used fuel is oxidized as the anode.[1,2] During the electrorefining process, fission products more active than uranium (e.g., Sr and Ba) are subjected to oxidation reactions at the anode and accumulate in the electrolyte as dissolved ions which should be removed from the electrolyte for proper process control and long-term storage.[3–5]

Recently, Lichtenstein et al. demonstrated a novel approach to separate Sr and Ba ions from LiCl-KCl eutectic via electrochemical deposition into a liquid Bi cathode at 773 K, and rationalized their results based upon strong chemical interactions between Bi and alkaline-earth metals, namely a low thermodynamic activity of alkaline earths in liquid Bi (e.g., $a_{Ba(in\ Bi)} = 6.6 \times 10^{-16}$ at mole fraction $x_{Ba(in\ Bi)} = 0.05$, 773 K).[6–8] Matsumiya et al. reported the utility of low-cost, low-melting liquid Pb ($T_{m,\,Pb} = 601$ K) for separating Sr ions from molten salt electrolytes based on the increased Sr content in Pb after galvanostatic discharge in NaCl-KCl or KCl electrolytes at 1073 K, and postulated that the deposition of Sr could occur possibly due to a low thermodynamic activity of Sr in liquid Pb.[9] Reliable thermochemical properties of liquid Sr-Pb alloys are essential in identifying the electrode reactions, and thus in evaluating the viability of liquid Pb electrodes for separating Sr from molten salt electrolytes. However, experimentally-verified thermochemical properties of Sr-Pb alloys are not widely available in the literature and were systematically investigated in this study.

Early studies of the thermodynamic properties of the Sr-Pb system were primarily focused on the detection of phase transition temperatures and intermetallic compounds to establish the Sr-Pb phase diagram,[10–17] with few details reported on the solution properties of Sr-Pb alloys. The most comprehensive study was conducted by Bruzzone et al., who investigated the phase behavior of the Sr-Pb system over the entire composition range and constructed an experimentally-determined phase diagram based upon phase transition temperatures determined via differential thermal analysis (DTA) and crystal structures of seven intermetallic Sr-Pb compounds ($SrPb_3$, Sr_3Pb_5, Sr_2Pb_3, SrPb, Sr_5Pb_4, Sr_5Pb_3, Sr_2Pb) identified using X-ray diffraction (XRD).[18] Recently, Zhang et al. modeled the thermodynamic description of the Sr-Pb system via the CALPHAD (CALculation of PHAse Diagrams) approach using reported experimental results (e.g., transition temperatures from DTA), the enthalpies of formation of intermetallic compounds from first-principles calculations, and a substitution solution model for liquid, fcc, and bcc phases.[19]

In this work, the thermochemical properties of Sr-Pb alloys were investigated via electromotive force (emf) measurements. Emf measurements of Sr-Pb alloys were conducted across a range of Sr mole fractions ($x_{Sr} = 0.07$–0.59) at 773–1073 K and used to determine the chemical potential, activity, partial molar entropy, and partial molar enthalpy of Sr in Pb. A solid-state CaF_2-SrF_2 (97-3 mol%) electrolyte was employed utilizing the chemical stability and the relatively high ionic conductivity of CaF_2 at elevated temperatures while SrF_2 was added to account for the change in electroactive species.[7,20] Phase transition behaviors observed during emf measurements were complemented by thermal and structural analyses of each alloy composition using differential scanning calorimetry (DSC) and XRD. These results were also compared to computationally assessed Sr-Pb thermochemical properties, including activity and excess Gibbs energy.

Electromotive force (emf) measurements of the Sr-Pb system.— The emf values of Sr-Pb alloys were measured using the following electrochemical cell:

$$\underline{\text{Sr (s)}}\,|\text{CaF}_2\text{-SrF}_2|\,\text{Sr (in Pb)} \qquad [1]$$

where pure Sr is the reference electrode (RE), solid CaF_2-SrF_2 (97-3 mol%) is the electrolyte, and Sr-Pb alloys are the working electrodes (WEs). The half-cell reactions for the electrochemical cell are below:

$$\text{WE: } \text{SrF}_2\,(\text{s}) + 2\text{e}^- = \text{Sr (in Pb)} + 2\text{F}^- \qquad [2]$$

$$\text{RE: } \text{SrF}_2\,(\text{s}) + 2\text{e}^- = \text{Sr (s)} + 2\text{F}^- \qquad [3]$$

with the following overall reaction:

$$\text{Sr (s)} = \text{Sr (in Pb)}\,. \qquad [4]$$

For this cell reaction, the change in partial molar Gibbs energy of Sr, $\Delta\bar{G}_{Sr}$, is:

$$\Delta\bar{G}_{Sr} = \bar{G}_{Sr(in\ Pb)} - G^0_{Sr(s)} = RT\ln\left(a_{Sr(in\ Pb)}\right) \qquad [5]$$

where $\bar{G}_{Sr(in\ Pb)}$ is the partial molar Gibbs energy of Sr in Pb, $G^0_{Sr(s)}$ is the standard free energy of pure Sr ($a_{Sr} = 1$), R is the universal gas constant, T is the cell temperature in Kelvin, and $a_{Sr(in\ Pb)}$ is the activity of Sr in Pb, moving forward referred to as a_{Sr}. Using the Nernst relation ($\Delta\bar{G}_{Sr} = -zFE_{cell}$), the measured cell ($E_{cell}$) potential

[z]E-mail: huk29@psu.edu

Journal of Alloys and Compounds 771 (2019) 281–289

Contents lists available at ScienceDirect

Journal of Alloys and Compounds

journal homepage: http://www.elsevier.com/locate/jalcom

Thermodynamic properties and phase stability of the Ba-Bi system: A combined computational and experimental study

Jinming Liu [a, b], Pin-Wen Guan [a, *], Cassie N. Marker [a], Nathan D. Smith [a], Nicole Orabona [a], Shun-Li Shang [a], Hojong Kim [a], Zi-Kui Liu [a]

[a] Department of Materials Science and Engineering, The Pennsylvania State University, University Park, PA, 16802, USA
[b] School of Material Science and Engineering, Jiangxi University of Science and Technology, Ganzhou, 341000, China

ARTICLE INFO

Article history:
Received 15 June 2018
Received in revised form
29 August 2018
Accepted 31 August 2018
Available online 1 September 2018

Keywords:
Electrochemistry
Ba-Bi system
CALPHAD
First-principles
Thermodynamics
X-ray diffraction

ABSTRACT

The thermodynamic properties and phase stability of the Ba-Bi system are investigated computationally and experimentally in the present work. The enthalpies of formation and the finite temperature thermodynamic properties of seven compounds are predicted by first-principles calculations based on density functional theory (DFT), indicating five compounds ($BaBi_3$, $Ba_{11}Bi_{10}$, Ba_4Bi_3, Ba_5Bi_3, and Ba_2Bi) to be stable. Phase relations at 773 K and 858 K with composition $x_{Ba} = 0.90$ are established by isothermal annealing and powder X-ray diffraction (XRD) to clarify the previously observed phase transition at 796 K. The extremely low chemical activity of Ba in liquid for a wide range of temperatures and compositions indicates very strong short-range ordering in the liquid phase which is modeled in the present work by introducing the Ba_4Bi_3 and $BaBi_3$ associates in the liquid phase. Both thermodynamic and phase equilibrium data are then used to evaluate the model parameters in Gibbs energy functions of the five stable compounds and three solution phases of liquid, bcc, and rhombohedral phases by the CALPHAD (CALculation of PHAse Diagram) technique. The present work shows that the Ba-Bi system consists of three eutectic reactions, two peritectic reactions, one peritectoid reaction, and two congruent reactions, as well as that the concentrations of associates are very high in the liquid phase with very low concentration of atomic Ba, which provides the fundamental understanding as to why Bi can be used to remove Ba ions from molten salt solutions.

1. Introduction

Recent experimental work by Kim et al. [1] outlined the ability of a liquid metal Bi electrode to separate Ba ions from a molten $BaCl_2$-LiCl-$CaCl_2$-NaCl (16-29-35-10 mol%) salt, despite the conventional expectation that Li, Na, and Ca would deposit into a Bi electrode first due to their more positive standard reduction potentials: −3.49 V, −3.42 V, and −3.44 V, respectively, vs. −3.74 V for Ba [2] in the Cl^-/Cl_2 (g) system. The unexpected phenomenon was believed to be a result of the strong atomic interactions (i.e., lower activity) between Ba and Bi, causing a shift in the standard reduction potential [1], given by the Nernst Equation:

$$E_{eq} = E^0_{Ba^{2+}/Ba} - \frac{RT}{2F}\ln\left(\frac{a_{Ba(in\ Bi)}}{a_{Ba^{2+}}}\right) \quad (1)$$

where E_{eq} is the equilibrium potential, $E^0_{Ba^{2+}/Ba}$ the standard electrode potential of the Ba^{2+}/Ba couple, R the ideal gas constant, T the absolute temperature, F Faraday's constant, and $a_{Ba(in\ Bi)}$ and a^{2+}_{Ba} are the activity values of Ba in the liquid Bi and Ba ions in the molten salt, respectively. This notion was further elucidated by Lichtenstein et al. [3] who performed electromotive force (EMF) measurements on the Ba-Bi system, determining the activity of Ba in Bi to be as low as 10^{-15} at $x_{Ba} = 0.05$ and 773 K, whereas the activity of Li in Bi is only about 10^{-6} at $x_{Li} = 0.05$ [4].

Leveraging these strong atomic interactions to preferentially remove alkaline-earth elements such as Ba from molten salts could provide a new paradigm in nuclear waste management [5], as the accumulation of elements such as Ba, Sr, and Cs in electrorefiner LiCl-KCl-UCl_3 electrolyte necessitates replacement, appropriate encapsulation, and disposal of the electrolyte as used nuclear waste due to the high heat densities and short half-lives of the alkaline-earth isotopes [6]. Improved understanding of the Ba-Bi system could provide a cost-effective and efficient method for removing the Ba, Sr, and Cs build-up in LiCl-KCl-UCl_3 without removing any of

* Corresponding author.
E-mail address: pxg928@psu.edu (P.-W. Guan).

https://doi.org/10.1016/j.jallcom.2018.08.324
0925-8388/